Luciano Selva Ginani

Optical Scanning Sensor System with Submicron Resolution

Berichte aus dem
INSTITUT FÜR MASCHINEN- UND
GERÄTEKONSTRUKTION (IMGK)

Herausgegeben von
Univ.-Prof. Dr.-Ing. Ulf Kletzin (Maschinenelemente),
Univ.-Prof. Dr.-Ing. René Theska (Feinwerktechnik) und
Univ.-Prof. Dr.-Ing. Christian Weber (Konstruktionstechnik)
aus dem Institut für Maschinen- und Gerätekonstruktion (IMGK) an
der TU Ilmenau.

Band 24

Diese Reihe setzt die „Berichte aus dem Institut für
Maschinenelemente und Konstruktion“ fort.

Optical Scanning Sensor System with Submicron Resolution

Luciano Selva Ginani

Universitätsverlag Ilmenau
2013

Impressum

Bibliografische Information der Deutschen Nationalbibliothek
Die Deutsche Nationalbibliothek verzeichnet diese Publikation in der Deutschen Nationalbibliografie; detaillierte bibliografische Angaben sind im Internet über http://dnb.d-nb.de abrufbar.

Diese Arbeit hat der Fakultät für Maschinenbau der Technischen Universität Ilmenau als Dissertation vorgelegen.

Tag der Einreichung:	28. Februar 2013
1. Gutachter:	Univ.-Prof. Dr.-Ing. René Theska (Technische Universität Ilmenau)
2. Gutachter:	Univ. -Prof. Dr.-Ing. habil. Eberhard Manske (Technische Universität Ilmenau)
3. Gutachter:	Prof. Dr. Herman Lepikson (Universidade Federal da Bahia)
Tag der Verteidigung:	21. Mai 2013

Technische Universität Ilmenau/Universitätsbibliothek
Universitätsverlag Ilmenau
Postfach 10 05 65
98684 Ilmenau
www.tu-ilmenau.de/universitaetsverlag

Herstellung und Auslieferung
Verlagshaus Monsenstein und Vannerdat OHG
Am Hawerkamp 31
48155 Münster
www.mv-verlag.de

ISSN 2191-8082 (Druckausgabe)
ISBN 978-3-86360-068-6 (Druckausgabe)
URN urn:nbn:de:gbv:ilm1-2013000337

Geleitwort der Herausgeber

Schriftenreihe des Instituts für Maschinen- und Gerätekonstruktion, Band 24:

Luciano Selva Ginani
Optical Scanning Sensor System with Submicron Resolution

Die Konstruktion von Maschinen und Geräten sowie die zugehörigen Methoden und Werkzeuge sind seit den frühen 1950er Jahren ein profilbildender Schwerpunkt an der Technischen Universität Ilmenau und ihren Vorgängerinstitutionen. Es war daher ein nahe liegender Schritt, dass die drei konstruktiv orientierten Fachgebiete der Fakultät für Maschinenbau - Maschinenelemente, Feinwerktechnik/Precision Engineering, Konstruktionstechnik - im Mai 2008 das Institut für Maschinen- und Gerätekonstruktion (IMGK) neu gegründet haben. Das IMGK steht in der Tradition einer Kette ähnlicher Vorgängerinstitute, deren wechselnde Zusammensetzung hauptsächlich durch sich über der Zeit ändernde Universitätsstrukturen bedingt war.

Zweck des Institutes ist es, die Kompetenzen und Ressourcen der beteiligten Fachgebiete zu bündeln, um Forschung und Lehre zu verbessern und erzielte wissenschaftliche Ergebnisse gemeinsam in die Fachöffentlichkeit zu tragen.

Ein wesentliches Instrument hierzu ist die Schriftenreihe des Instituts für Maschinen- und Gerätekonstruktion. Sie führt eine erfolgreiche Schriftenreihe des im Jahr 1991 gegründeten unmittelbaren Vorgängerinstitutes IMK (Institut für Maschinenelemente und Konstruktion) fort.

In der Schriftenreihe erscheinen in erster Linie die am Institut entstandenen Dissertationen, daneben werden aber auch andere Forschungsberichte, die in den thematischen Rahmen passen und von allgemeinem Interesse sind, in die Schriftenreihe aufgenommen.

Der vorliegende Band 24 ist als Dissertation am Fachgebiet Feinwerktechnik entstanden.

Die Herausgeber wünschen sich reges Interesse an der Schriftenreihe und würden sich freuen, wenn sie zum fruchtbaren Dialog in Wissenschaft und Praxis beitragen würde.

Ilmenau, im März 2013

Univ.-Prof. Dr.-Ing. Ulf Kletzin (Maschinenelemente)
Univ.-Prof. Dr.-Ing. René Theska (Feinwerktechnik)
Univ.-Prof. Dr.-Ing. Christian Weber (Konstruktionstechnik)

Abstract

Laser Scanning Microscopy (LSM) has been used for a long time in the field of surface measurement and is today one of the most promising technologies for fast, accurate and repeatable measurements in application areas such as material science, microelectronics, medical technology, and, especially, nanotechnology. Its basic concept was originally developed in 1957 by Marvin Minsky, and it is basically a technique for increasing contrast and resolution in optical imaging systems through the rejection of out-of-focus light. Images are acquired point-by-point and reconstructed with a computer, allowing the three-dimensional reconstruction of complex objects.

All modern laser scanning microscope designs are centred on conventional upright or inverted optical microscope arrangements and the use of standard high-end objectives lenses with high numerical aperture, for which there is a large design experience basis. In this work, autofocus and optical scanning technologies are brought together in the design and construction of an alternative simplified scanning microscope for surface measurements in millimetre range with sub-micrometer resolution. The developed system uses an autofocus sensor based on the Foucault knife-edge principle to generate a defocus signal and a high precision piezo positioning stage for translating the objective and scanning the samples in the axial direction. For the lateral scanning, a piezo driven tip-tilt mirror is used.

The developed scanning microscope is built with a reduced number of optical components and designed to offer a simple and versatile experimental set-up for the measurement and analysis of errors induced by optical aberrations due to the use of suboptimal optics in scanning microscopy. The reduction of the number of optical components and the use of simple uncompensated lenses has always been avoided in scanning microscopy as it inserts optical aberrations into the system, generating asymmetries in the defocus signal and deteriorating its overall

performance. The traditional way of solving this problem is to improve the optical system such that it works as a paraxial lens, but that comes with the price of heavy and costly optics. Thanks to advances made in modern computing power, it is now possible to consider unconventional alternatives to optics optimization.

By breaking the paradigm of improving the optics to a paraxial lens and observing the optics as part of a complex system, it is possible to use simpler optics and correct the resultant errors computationally. These errors are systematic and, as long as they can be measured and modelled, can be predicted and corrected. This way, the design of the optical system becomes much more flexible and the task of error handling can be divided between optics optimization and computational correction, reducing overall size and weight, raising system dynamics and reducing costs, without losing accuracy. The goal is not to study each optical aberration individually, but to measure and model their combined influence in the measurements. Different strategies for addressing these measurement errors caused by the use of uncompensated optics are proposed, discussed and experimentally validated.

Zusammenfassung

Laser-Scanning Mikroskopie (LSM) ist eine seit langer Zeit im Bereich der Oberflächenmessung sehr wichtige und sehr vielversprechende Technologie für schnelle, genaue und wiederholbare Messungen in Anwendungsbereichen wie Mikroelektronik, Medizintechnik, Materialwissenschaft und insbesondere Nanotechnologie. Das Grundprinzip wurde ursprünglich im Jahre 1957 von Marvin Minsky entwickelt. Es ist im Grunde eine Technik zur Erhöhung von Kontrast und Auflösung in optischen Abbildungssystemen. Ein Prüfling wird punktweise abgetastet und ein Bild seiner Oberfläche mit Hilfe eines Rechners erfasst und rekonstruiert, sodass die Aufnahme von komplexen dreidimensionalen Objekten möglicht ist.

Alle modernen Scanning Mikroskope basieren auf der herkömmlichen aufrechten oder umgekehrten Bauweise von Lichtmikroskopen unter Verwendung von High-End Mikroskopobjektiven mit hoher numerischer Apertur. In dieser Arbeit werden Autofokus- und optische Abtastverfahren in der Entwicklung und Konstruktion eines alternativen, vereinfachten Scanning Mikroskops für Oberflächenmesstechnik im Millimeterbereich mit Sub-Mikrometer Auflösung zusammengebracht. Das System verwendet einen auf dem Foucault'sches Schneidenverfahren basierenden Autofokussensor um die Fokuslage zu bestimmen und einen hochpräzisen Piezo-Linearantrieb für die Verschiebung des Objektivs entlang der optischen Achse sowie das Abtasten des Prüflings in der axialen Richtung. Die laterale Abtastung des Prüflings wird durch den Einsatz eines Piezo-Spiegels realisiert, der um zwei Achsen schwenkbar ist.

Das entwickelte Scanning Mikroskop hat eine reduzierte Anzahl von optischen Komponenten und bietet einen einfachen und vielseitigen Versuchsaufbau zur Messung und Analyse von Fehlern, die durch die bewusste Verwendung von unkompensierten Optiken und deren entsprechende Abbildungsfehler auftreten. Die Verringerung der An-

zahl der optischen Komponenten und der Einsatz einfacher, unkompensierter Linsen wird prinzipiell in der Scanning-Mikroskopie vermieden. Die damit verbundenen Abbildungsfehler erzeugen Asymmetrien in den Autofokussensoren und beeinträchtigen die Gesamtleistung. Die herkömmliche Lösung dieser Problematik ist das System durch Addition zusätzlicher optischer Komponenten zu verbessern, sodass es wie ein paraxiales System für den gesamten Funktionsbereich wirkt. Diese Verbesserung bringt aber die Nachteile von Baugröße, Gewicht und Kosten mit sich. Unter Berücksichtigung der heutigen verfügbaren Rechenleistung, ist es jetzt möglich, unkonventionelle Alternativen zur Optimierung der Optik in Betracht zu ziehen.

Durch das Brechen des Paradigmas der Verbesserung der Optik bis zu einem paraxialen System und die Betrachtung der Optik als Teil eines komplexen Systems ist es möglich, simplere Optik zu verwenden, und die resultierenden Fehler rechnerisch zu korrigieren. Diese Fehler sind systematisch und können - solange sie modelliert und gemessen werden können - vorhergesagt und korrigiert werden. Damit wird das Design des optischen Systems wesentlich flexibler und die Aufgabe der Fehlerbehandlung zwischen Optimierung der Optik und rechnerischer Korrektur aufgeteilt. Baugröße, Gewicht und Kosten können dann reduziert werden und die Systemdynamik erhöht sich, ohne Einschränkung der Präzision. Das Ziel ist nicht jeden Abbildungsfehler individuell zu untersuchen, sondern deren Zusammenwirken auf die Messungen zu beobachten und zu modellieren. Verschiedene Strategien für die Behandlung dieser Messfehler werden in dieser Arbeit vorgeschlagen, diskutiert und experimentell validiert.

Vorwort

Die vorliegende Dissertation entstand während meiner Tätigkeit als wissenschaftlicher Mitarbeiter am Fachgebiet Feinwerktechnik in der Technischen Universität Ilmenau. Diese Arbeit wurde mit Mitteln der Deutsche Forschungsgemeinschaft (DFG) im Rahmen des Sonderforschungsbereich SFB622 “Nanopositionier- und Nanomessmaschinen” und der Johannes Hübner Stiftung Gießen (JHS) unter dem Projekt Nr. 01/10 “Entwicklung optisch scannender Sensorsysteme” gefördert.

An erster Stelle möchte ich meinem Doktorvater Herrn Prof. Dr.-Ing. René Theska, Direktor des Instituts für Maschinen- und Gerätekonstruktion und Inhaber des Lehrstuhls für Feinwerktechnik an der Technischen Universität Ilmenau, herzlich danken. Er hat immer an mein Potenzial geglaubt und durch seine persönliche Unterstützung und sein Vertrauen diese Arbeit ermöglicht. Seine wissenschaftliche Betreuung und wertvollen Anregungen haben mich immer vorangetrieben.

Herrn Prof. Dr.-Ing Eberhard Manske, Leiter des Fachgebietes Präzisionsmesstechnik an der Technischen Universität Ilmenau, und Herrn Prof. Dr. Herman Augusto Lepikson, an der Bundesuniversität von Bahia (Brasilien), danke ich für die Übernahme der Gutachten der Arbeit und die wertvollen Hinweise zu meiner Dissertationsschrift.

Meinen Kollegen Kerstin John, Tobias Hackel und Christoph Hahm sowie allen Mitarbeitern der Fachgebiet Feinwerktechnik und des Graduiertenkollegs des SFB622 danke ich für die Zusammenarbeit und die zahlreichen wissenschaftlichen Gesprächen und Diskussionen, die mir stets neue Ideen und Anregungen boten.

Ich bedanke mich ebenso bei der Johannes Hübner Stiftung für die finanzielle Förderung der Arbeit. Ohne ihre Unterstützung wäre diese Arbeit nicht möglich gewesen. Sie hat durch eine unkomplizierte und unbürokratische Vorgehensweise meine Arbeit und wissenschaftliche

Freiheit immer gefördert und unterstützt. Ihr Vertrauen und ihre Unterstützung waren essenziell für den Abschluss meiner Promotion.

Ein besonders herzlicher Dank gilt meinen Eltern. Mit ihrer Unterstützung, unendlichen Geduld und freundlichem Nachdruck haben sie beständig meine Bestrebungen zur Erweiterung meines Horizonts gefördert.

Ilmenau, März 2013
Luciano Selva Ginani

Contents

Abstract **vii**

Zusammenfassung **ix**

Vorwort **xi**

Abbreviations and Symbols **xv**

1 Introduction **1**
1.1 Optical Measuring Technologies and Systems 4
1.2 Objectives and Structure 6

2 Fundamentals and State of the Art **9**
2.1 Principles of Optics 9
2.1.1 The Nature of Light 9
2.1.2 Geometric Optics 10
2.1.3 Ray-Tracing 12
2.1.4 Optical Aberrations 17
2.2 Confocal Microscopy 20
2.3 Resolution Limits of Optical Instruments 23
2.4 Auto-focus in Optical Systems 26
2.4.1 Astigmatic Method 26
2.4.2 Foucault Knife-Edge Method 32
2.5 Optical Scanning 36
2.6 Modern Confocal Laser Scanning Microscopy 38

3 Design and Development of a Simplified Scanning Microscope **41**
3.1 Basic Design 41
3.2 Telecentricity 46
3.3 Scanning Procedure 47
3.4 Control and Data Acquisition 50

4 Modelling, Simulation and Calibration 53
4.1 Correction vs Compensation 54
4.2 Error Correction in Scanning Systems 55
4.3 Model Based Error Correction 57
4.3.1 Paraxial Model 59
4.3.2 Ray-Tracing Model 69
4.3.3 Model Calibration 75
4.4 Measurement Based Error Correction 81
4.4.1 Look-up Table 83
4.4.2 Polynomials 85

5 Experimental Results 89
5.1 Characteristic Curve of the Sensor 89
5.2 Error and Sensitivity Analysis 92
5.3 Model Calibration and Function Measurement 96
5.4 Error Correction Methods 97
5.5 Influence of the Model Calibration 103
5.6 Influence of Sample Inclination in the Measurements . 104
5.7 Vertical and Lateral Resolution and Noise 107
5.7.1 Vertical Resolution and Noise 108
5.7.2 Lateral Resolution and Noise 110
5.8 Repeatability 115
5.9 Comparison with other Measurement Systems 116
5.10 Ray-Tracing Implementations 117

6 Measurement Tasks and Applications 121

7 Conclusions and Further Work 125
7.1 Conclusions 125
7.2 Further Work 126

List of Figures 132

List of Tables 133

Bibliography 142

Abbreviations and Symbols

Abbreviations

ADC	Analog Digital Converter
AFM	Atomic Force Microscope
ASP	Asphere
CCD	Charged Coupled Device
CMM	Coordinate Measuring Machine
CMOS	Complementary Metal-Oxide Semiconductor
CPU	Central Processing Unit
DAC	Digital Analog Converter
DSP	Digital Signal Processing
DVD	Digital Versatile Disk
FES	Focus Error Signal
FWHM	Full Width at Half Maximum
GPU	Graphic Processing Unit
HOE	Holographic Optical Element
IEEE	Institute of Electrical and Electronics Engineers
LMA	Levenberg-Marquardt Algorithm
LSM	Laser Scanning Microscopy
LUT	Lookup Table
MEMS	Micro-Electro-Mechanical System
MOEMS	Micro-Opto-Electro-Mechanical System
NA	Numerical Aperture
NPMM	Nanopositioning and Measuring Machine
PCX	Plan Convex
PI	Proportional Integral
PSD	Position Sensitive Device

RMS	Root Mean Square
SPM	Scanning Probe Microscopy
SEM	Scanning Electron Microscopy

Symbols

Symbol	*Unit*	*Description*
α	rad	Field Angle
f	mm	Focal Length
λ	nm	Wavelength
n	-	Refractive Index
δ	μm	Defocus
β	$\circ$	Sample Inclination
β_{max}	$\circ$	Maximum Measurable Sample Inclination
θ_x	mrad	Mirror Tilting Angle
θ_y	mrad	Mirror Tilting Angle
Δ_z	μm	Objective Displacement
V_x	V	Voltage Control Signal for the Mirror Tilting Angle
V_y	V	Voltage Control Signal for the Mirror Tilting Angle
V_z	V	Voltage Control Signal for the Objective Displacement
DIF	V	Difference Voltage Signal
SUM	V	Sum Voltage Signal
$[P_x, P_y, P_z]$	mm	Measured Point Coordinates
F_{LSM}	-	Function of the Laser Scanning Microscope
J_{LSM}	-	Jacobian Matrix of the Function F_{LSM}
Q	-	Parameters of the Function F_{LSM}
$T_{i,j}$	-	Homogeneous Transformation
T_x	-	Translation along the X-axis
T_y	-	Translation along the Y-axis
T_z	-	Translation along the Z-axis
R_x	-	Rotation on the X-axis
R_y	-	Rotation on the Y-axis
R_z	-	Rotation on the Z-axis
$\vec{S}_i$	-	Mathematical Description of an Optical Surface

$\vec{R}_i$	-	Mathematical Description of an Optical Ray
$\vec{N}$	-	Normal Vector of an Optical Surface
C	mm^{-1}	Surface Curvature
K	-	Conic Constant
TH	mm	Lens Thickness
K_i	-	Aspheric Coefficients

Chapter 1

Introduction

In many ways the nanotechnology era has already began. Nanotechnology is a very broad and fast developing field. It can be defined as a collection of different techniques and approaches, which take advantage of the physical properties of dimensions on the nanometre scale to the production of structures and devices with novel or optimized characteristics and features. [Hul07, SS02]. Numerous forecasts predicting massive growth in the nanotechnology markets have appeared in recent years and almost daily new nanofabrication technologies and nanodevices based on electrical, optical, magnetic, mechanical, chemical and biological effects are reported [Bog07, Hul07, SS02, DDX+10]. But so that such technology may indeed start a new revolution, it must be underpinned by a reliable metrology infrastructure that is yet not fully available [HCHD06, Hul07, SS02, LBB+10, Gra07].

Metrology is a vital part of industrial manufacturing as it enables networks of services, suppliers and communications to work with efficiency and reliability, but when the dimensions are reduced from the micro to the nanoscale there are major differences in the associated metrological requirements [Bog07]. Dimensional metrology for nanotechnology requires measuring instruments to provide shape and size information with atomic levels of resolution and precision, and that has to be done within seconds. This precise and fast measurement of structures from macro to nano in constantly increasing volumes of up to several hundred millimetres with nanometer precision is a constantly increasing demand of today's industry. Such requirements are mostly evident in fields such as microelectronics, data storage and advanced photonics, where the technological progress is characterized

by reductions in size, although precision in the nanoscale is already a requirement for many industrial and research fields. Precision engineering, lithography, nanomaterials, thin films, optics, micromechanics and many other industries work today on the limits of actual instrumentation.

This tendency to miniaturisation is growing and spreading to other fields and, in order to support this expansion and to promote the further development of these high-end industries, accessible and reliable instruments that allow the measurement and manipulation of structures with nanometer precision are necessary. This can already be seen in most of the state-of-the-art measuring equipments in use or under development today. Electron Microscopy (EM), Scanning Probe Microscopy (SPM) and near field microscopy are just a few examples [Bog07, SMGH95, DDX+10, WPH06]. Scanning electron microscopes (SEM) and atomic force microscopes (AFM) are the most commonly used instruments.

Most of the systems used for the measurement of structures in the nanoscale have a very limited working range and are therefore often used as probing systems in coordinate measuring machines (CMMs). In such applications, the obtained precision is determined by the CMM used for positioning the samples and measuring instruments [Bog07]. This important role played by CMMs led to the recent development of the μ-CMMs and more recently the Nano-CMMs, which are able to achieve resolutions in the sub-nanometric range in working volumes up to a few millimetres [Bog07, SS02, HTB+06, TFHL04, Hac10]. Figure 1.1 shows such a Nano-CMM developed in the Ilmenau University of Technology and its basic working principle.

The nanopositioning and nanomeasuring machine (NPMM) uses three interferometers arranged in a way to build a cartesian coordinate system so that their light beams virtually intersect at a single point located on the tip of the probing system. This way the distance between the point of measurement and the reference line of the measurement system, and therefore the Abbe-Error, are minimized. The machine has a working volume of $25mm \times 25mm \times 5mm$, a resolution of $0.01nm$ and a positioning uncertainty of less than $10nm$ in all three axes. It also allows the use of different probe systems for accomplishing various measuring or machining tasks.

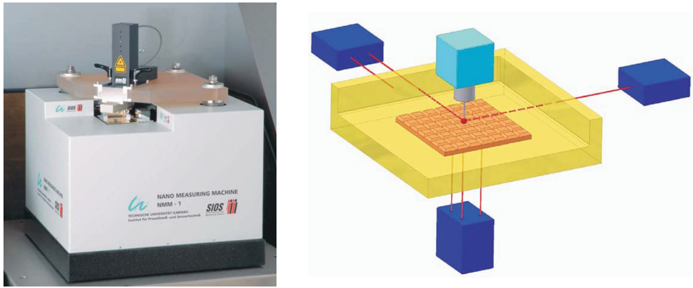

Figure 1.1: The nanopositioning and measuring machine (NPMM) developed in Ilmenau.

Nano-CMMs equipped with AFMs are today the state of the art in the measurement of technical surfaces [JHM+06, Jö6, MHM+07]. They allow the measurement of different samples with sub-nanometer resolutions independent of material properties, but also have some disadvantages. The cantilever sensors used in AFMs have an extremely limited working range ($2-20\mu m$), which, when exceeded, causes premature breakage of the cantilever. These sensors work mostly in contact with the sample surface or in a very small gap and in order to keep the deflection of the cantilever minimum the distance between sample and cantilever must be continuously adjusted. The speed with which this adjustment can be made is limited by the dynamic of the positioning system, so that the surface topography can not be followed without a time delay. As the surface topography in sub-micrometer range is normally unknown and the sensor tip is "blindly" guided through the sample surface, there is a constant danger of a collision between the sensor and the sample. In order to avoid collisions, Nano-CMMs are often operated with reduced scanning speed, resulting in long measuring times, which can easily amount to several hours.

A second limitation of Nano-CMMs equipped with AFMs, typical in high-resolution systems, is the amount of data generated. As the scanning speed and the size of the measured areas increase, the necessary data rate and the resulting data size also increases. A small area of $(1 \times 1)mm^2$ scanned with steps of $10nm$, a resolution of 32 bits per measuring point and an acquisition rate of $10Khz$ would take about 12 days and comprise at least 120 gigabytes of data.

One way to overcome these problems is the use of feature-oriented measurements, where the step size, and therefore the data density, can be altered during the measurement. This way, simple regions without important features can be measured with low data density and important areas with high density, obtaining an increase in the measuring throughput and a reduction in the overall data size and measurement time.

However, that is not possible with the use of a single sensor. For the efficient measurement of extended areas, the integration of multiple sensors is necessary. In this work, an alternative to overcome these difficulties, based on the development of a novel fast miniaturized optical pre-scanning system, is proposed. The pre-scanning system allows a rapid parallel measurement of the sample topography, so that *a priori* information about the sample in the sub-micrometer range can be acquired and used to optimize measurement planning and scanning speeds of the more precise sensor without data or precision losses and without risking a collision between sensor and sample.

In this context, non-contact measuring systems and optical scanning play an important role. Merbach [Mer84] discussed the importance of these systems and presented in his work a systematic analysis of different non-contact technologies and their use in dimensional measuring, while Barthel [Bar85] discussed in more detail the use of optical technologies for non-contact dimensional measuring.

Figure 1.2 illustrates an example of a measuring task using a cantilever sensor and the typical dimensions involved. With the use of an optical pre-scanning system, the collision risk between the cantilever and the step can be detected and the data density of the measurement adjusted, optimizing the measuring task.

1.1 Optical Measuring Technologies and Systems

Optical technologies are a key technology in many technical fields and optical based sensors and systems are today an essential tool in metrology. They not only offer a flexible, fast and robust measurement, but also distinguish themselves through a multitude of advantages. They

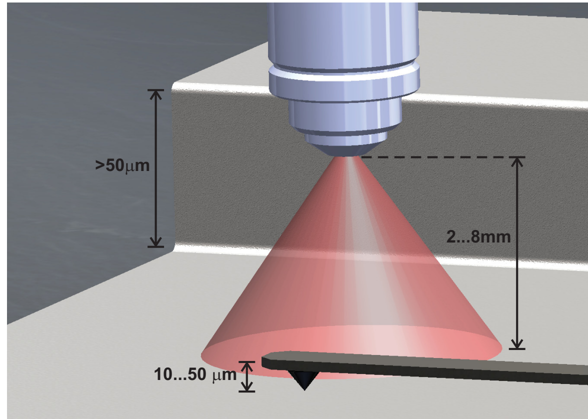

Figure 1.2: Conceptual diagram of the proposed optical pre-scanning system.

are a non-contact, non-destructive and non-invasive measuring technology, demonstrate no wear and present a large potential for miniaturization and integration with other measuring systems. Optical sensors cover scales ranging from nanometers to kilometres and, thanks to their relative low cost, are adopted in a wide variety of applications. However, they also have some drawbacks and limitations. Specifically in the field of surface measurements, topics such as dependence to optical characteristics of the probe surface, limited lateral resolution and measuring artifacts due to optical diffraction need to be considered. Even though, in many high-end industries, where the nanoscale is already a reality, optical sensors determine the state of the art, as it is in the case of the semiconductor industry [Kni03].

There is a wide variety of technologies in the field of optical measurements and new ones are constantly developed. A few examples are triangulation methods, moiré and structured light methods, interferometry (homodyne, polarization, white light, heterodyne), wavefront sensors, speckle methods, holographic methods, microscopy, confocal microscopy, conoscopy, near field scanning microscopy and many others [Lea11,Gas02,CK96]. Two of these are of greater importance to the presented work and are addressed in more detail in following chapters: confocal laser scanning microscopy and focus detection methods.

Nevertheless, all these technologies share as a common point the use of optical systems and sensors, combining many different technical fields and using light as information carrier for measuring different parameters and properties. While the optical sensor is responsible for converting light rays into electronic signals, the optical system is responsible for capturing, shaping and directing those rays and is the core of most optical measurements.

An optical system is a group of lens, mirrors, prisms, and other optical elements, placed in a specific configuration to reflect, refract, disperse, absorb, polarize, or otherwise interact with light. These specific configurations or schemas are normally chosen so that optical aberrations are minimized and the optical system may be described with the paraxial approximation. This is nowadays mostly done with the use of computer aided optimization techniques in order to improve the performance of the optical system until the desired tolerances are achieved and, for achieving tight tolerances, the number of necessary elements is often large, leading to large and heavy optics.

A second point of interest in this work is to consider software based alternatives to optical optimization. Considering the optics as part of a complex system, it is possible to use simple non-optimized optics and correct a part of their optical errors computationally. By observing the effects of optical aberrations in the measurement system as a whole, the task of minimizing these errors can be divided between the optical design and the post-processing of the measurement data, so that, with the use of simpler optics, overall weight and size can be reduced as well as costs, facilitating miniaturization and integration of optical measurement systems in different applications.

1.2 Objectives and Structure

The objective of this work is to develop and design a fast optical scanning system for technical surfaces based on the use of simple uncompensated optics and its validation. The proposed system is designed to reduce overall costs and weight, improving measurement speed and system dynamic and expanding the possibilities for miniaturization. In order to overcome the effects of optical aberrations caused by the use of simple optics, a novel approach is proposed, where the effects of

these aberrations in the measurements are computationally corrected. This way, through computation and intelligent measuring, more information can be extracted from the system and the control of optical aberrations can be divided between optical compensation (*hardware*) and data correction (*software*), offering more flexibility for the system's design.

This work was developed within the framework of the *Collaborative Research Centre 622: Nanopositioning and Measuring Machines* from the *Deutsche Forschungsgemeinschaft* (DFG) and was also supported by the *Johannes Hübner Stiftung*. It is structured in seven chapters emphasizing the following points:

Chapter 2 presents the basic concepts necessary for the comprehension of the developed work with emphasis in the fields of focus detection and optical microscopy and measuring technologies.

Chapter 3 describes the developed scanning system, its optical design and its operation principle with the combination of auto-focus detection for axial scanning and a tilting mirror for lateral scanning.

Chapter 4 shows the complete modelling of the system using both the paraxial and geometric light models in order to observe the influence of optical aberrations on the system's behaviour. It also introduces the proposed correction strategies for accounting for these influences.

Chapter 5 shows a series of experimental tests and simulations to evaluate the developed system and its performance as well as to validate the proposed error correction strategies and observe experimentally the influence of optical aberration and different sample's characteristics in the measuring results.

Chapter 6 shows the obtained results with the developed system for different measuring tasks and illustrates different possible applications.

Chapter 7 concludes the work with a summary of the achieved knowledge and the obtained results, and gives an outlook of further potential developments and studies.

Chapter 2

Fundamentals and State of the Art

To facilitate the comprehension of the presented work and the developed measurement system, the basic knowledge required for its understanding is presented in this chapter. A short summary on the fundamentals of optical systems and instruments is devised as well as a short introduction to the fields of confocal laser scanning microscopy and auto-focus detection.

2.1 Principles of Optics

Optics is the branch of the physics responsible for the study of light, its properties and its interaction with matter. In this chapter only a short overview of the necessary knowledge for the description and comprehension of optical systems is presented. For a deeper comprehension of the points discussed in this chapter, Haferkorn [Haf94], Hecht [Hec02] and Bass [Bas95] offer a solid literature basis.

2.1.1 The Nature of Light

Light is the name given to a small range of the electromagnetic spectrum that can be detected by the human eye. The modern light theory is highly complex and tries to describe the wave-particle duality of electromagnetic radiation using the wave and the quantum models.

Such a description is nevertheless often not necessary for describing most optical systems and instruments, so that the classical electromagnetic wave description based on Maxwell's equations and the geometric optics are the most widely used models for the description of light and are also the models adopted in this work.

In the wave theory, light is described as an electromagnetic wave, that is, as an oscillating electric and magnetic field which propagates through space. This way, the wave can be represented by describing its electric field, as shown in Equation 2.1, where r is the position vector of a point inside the field and both the amplitude A and phase Φ of the wave are functions of the spatial coordinates and of the time.

$$\boldsymbol{E}(\boldsymbol{r}, t) = \boldsymbol{A}(\boldsymbol{r}, t) \cos\left(\Phi(\boldsymbol{r}, t)\right) \tag{2.1}$$

In optics, light is often simplified as a linearly polarized monochromatic plane wave so that Equation 2.1 can be rewritten as shown in Equation 2.2, where s is the direction of propagation of the field, λ is the wavelength of the light, c its speed in the medium and δ the phase of the field at the instant $t = 0$ in the position $\boldsymbol{r.s} = 0$.

$$\boldsymbol{E} = \boldsymbol{A} \sin\left(\frac{2\pi c}{\lambda}(\boldsymbol{r.s}) - \frac{2\pi}{\lambda} t + \delta\right) \tag{2.2}$$

The amplitude A of the wave defines the brightness of the light and the wavelength λ its colour. The wave theory can explain effects such as interference and diffraction as well as reflection and refraction and is extremely important to the determination of the resolution limits of optical instruments (Chapter 2.3).

2.1.2 Geometric Optics

Although the wave model of light can describe most of the observed optical phenomena, it is often too complex, so that, in practice, a simplified model, the ray model, is normally used. The ray model is used by the geometric optics and describes light as a collection of rays that travel in straight lines and change their direction when they pass through different media or reflect on a surface.

Geometric optics describes the reflection and refraction of light, but not its diffraction. Although, when the wavelength of light is small compared to the size of the structures involved, the diffraction effects are strongly reduced and the geometric optics and the ray model of light offer a high accurate description of the system [Haf94, Hec02].

In order to simplify even further the analysis of optical systems in geometric optics and make the propagation of rays through the optical system linear, the thin lens model together with the paraxial approximation is often used. Figure 2.1 illustrates a single lens and how the image S' of an object S is formed by a thin lens.

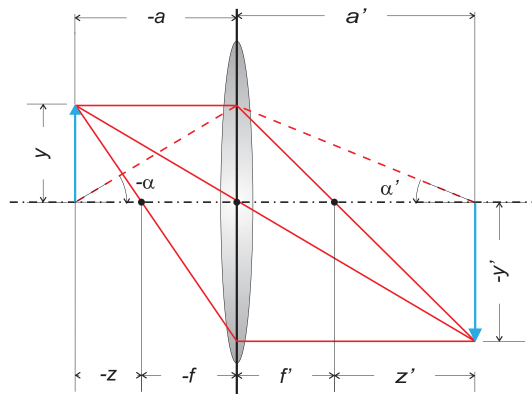

Figure 2.1: Image formation on a thin lens.

The paraxial approximation is only valid for rays that have a small angle to the optical axis of the system and are near it, so that $\tan(x) = \sin(x) = x$. This way the relation between the object and image positions a and a' is given by the Newtonian form of the lens equation (Equation 2.3) and the image magnification β' is given by Equation 2.4.

$$ff' = aa' \tag{2.3}$$

$$\beta' = \frac{y'}{y} = \frac{a'}{a} = \frac{f}{f-a} \tag{2.4}$$

2.1.3 Ray-Tracing

Ray-tracing is a widespread technique for the design and simulation of optical elements and systems through the generation of an optical path in a system based on the laws of geometric optics. By successively applying the laws of reflection and refraction on the optical surfaces (lens, mirrors, prisms, etc), a light ray can be propagated from its source to its target and the analysis of various optical properties can be carried out.

Ray-tracing involves the geometrical modelling of the optical surfaces of a system, defining their optical properties, approximating the light sources with directional rays and then propagating these rays through system models [SM62, Lin94]. Although some ray-tracing techniques do take into account properties such as energy, polarization and the wave nature of light [MPM05], in this work, and in general, rays are treated as a mathematical abstraction with a point of origin and a direction. This assumption simplifies computation and usage while still offering reliable results for most applications [MPM05, SM62]. Figure 2.2 exemplifies the basic elements and steps of ray-tracing in optical systems.

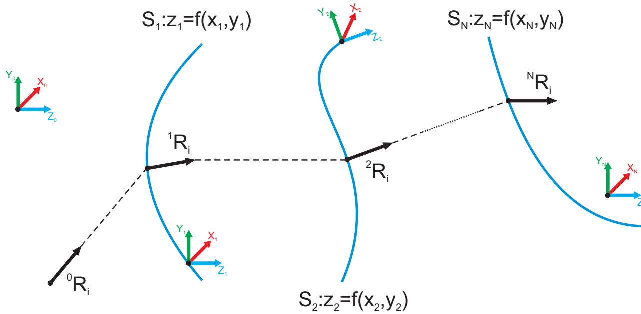

Figure 2.2: Ray-tracing general procedure.

Each ray ($\vec{R_i}$) is propagated through the optical surfaces ($\vec{S_j}$) by applying the laws of reflection and refraction. The optical surfaces are all mathematically described and their position and orientation in reference to a global coordinate system are defined. The ray-tracing procedure is well known and largely described in the literature [MPM05,

SM62, GT09, Lin94]. Both sequential and non-sequential ray-tracing techniques are similar and can be summarized through the flowchart illustrated in Figure 2.3. While non-sequential ray-tracing demands the mathematical determination of the next surface that the ray intersects, in sequential ray-tracing the surface sequence is predetermined.

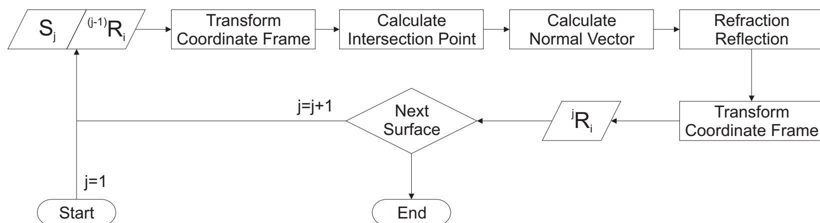

Figure 2.3: Ray-tracing flowchart.

The first step is the mathematical definition of the involved structures: rays and surfaces. A ray $\vec{R}$ can be defined through the parametric equation shown in Equation 2.5, where (x_R, y_R, z_R) are the coordinates of a point through which it passes and (k_R, l_R, m_R) its direction cosines in a global coordinate system (X_0, Y_0, Z_0).

$$\vec{R}(t) = \begin{bmatrix} x_R \\ y_R \\ z_R \end{bmatrix} + \begin{bmatrix} k_R \\ l_R \\ m_R \end{bmatrix} t \tag{2.5}$$

A surface $\vec{S}$, on the other side, is defined through Equation 2.6 using a support coordinate system (X_j, Y_j, Z_j).

$$\vec{S}(x,y) = \begin{bmatrix} x \\ y \\ f(x,y) \\ 1 \end{bmatrix} \tag{2.6}$$

There is a wide range of surfaces that are used as optical components. When dealing with rotation symmetrical surfaces the most common are spheres, aspheres and planes. All these surfaces can be seen as solids of revolution and the form of its cross sections can be mathematically described using the even aspheric equation [Haf94, NS92]

(Equation 2.7), where z is the height of the aspheric surface, r the radial distance to the centre, C the surface curvature, K the conic constant and K_i the aspheric coefficients of the surface. The even aspheric equation is widely used by optical manufacturers and optical design programs to describe lenses [Haf94, Mar91, NS92].

$$z = \frac{Cr^2}{1+\sqrt{1-(1+K)\,C^2r^2}} + K_2r^2 + K_4r^4 + ... \tag{2.7}$$

This way, the surface shape is fully defined using the parameters (C, K, K_2, K_4, ...) and the next step in describing the optical surface is to define its position in the global coordinate system. Homogeneous coordinates and transformation matrices offer an optimal tool for this task, as they can represent rotation and translation in the form of matrix operations. This way, any point from a surface $\vec{S}$ can be represented in the global coordinate system using Equation 2.8.

$$\vec{S}'(x,y) = T(\alpha,\beta,\gamma,d_x,d_y,d_z)\begin{bmatrix} x \\ y \\ f(x,y) \\ 1 \end{bmatrix} \tag{2.8}$$

,where $T(\alpha,\beta,\gamma,d_x,d_y,d_z)$ is an homogeneous transformation defined by Equation 2.9 with the use of Euler angles [TV98].

$$\begin{cases} T = \begin{bmatrix} C_\alpha C_\gamma + S_\alpha S_\beta S_\gamma & -C_\beta S_\gamma & -S_\alpha C_\gamma + C_\alpha C_\beta C_\gamma & d_x \\ C_\alpha S_\gamma - S_\alpha S_\beta S_\gamma & C_\beta C_\gamma & -S_\alpha S_\gamma - C_\alpha C_\beta C_\gamma & d_y \\ S_\alpha C_\beta & S_\beta & C_\alpha C_\beta & d_z \\ 0 & 0 & 0 & 1 \end{bmatrix} \\ S_x = \sin(x) \\ C_x = \cos(x) \end{cases} \tag{2.9}$$

The transformation T also enables the surface $\vec{S}$ to move freely through the space, so that the mechanical movement of system components can then be described and simulated. Once the basic mathematical

structures are described, the next step is the definition of the ray-tracing operations shown in the flowchart in Figure 2.3. In sequential ray-tracing, the surface sequence is predetermined, so that the calculation of the next surface in the optical path is not necessary. For the evaluation of the surface geometry, the calculation of the intersection point between a surface and a ray is given by the solution of the vector equation:

$$T\vec{S}(x,y) - \vec{R}(t) = \vec{0} \tag{2.10}$$

Nevertheless, computationally, Equation 2.10 can be rewritten in a more efficient way as shown in Equation 2.11. This way the evaluated ray is represented in the support coordinate frame and the number of necessary mathematical operation reduced.

$$\vec{S}(x,y) - T^{-1}\vec{R}(t) = \vec{S}(x,y) - \vec{R}'(t) = \vec{0} \tag{2.11}$$

As the function $f(x,y)$ can be any arbitrary function, a direct solution is not always possible, so that the use of numerical methods offer a more flexible solution. The intersection point between the surface $\vec{S}$ and the ray ($\vec{R}'$) can then be determined by finding the parameter t that minimizes Equation 2.12:

$$\varepsilon(t) = \left[z_{\vec{R}'}(t) - f\left(x_{\vec{R}'}(t), y_{\vec{R}'}(t)\right)\right]^2 \tag{2.12}$$

Once the intersection point $\overline{P}_{\vec{R}'}$ is determined, the surface normal in this point can be calculated as:

$$\vec{N} = \left. \left| \begin{matrix} -\frac{\partial f(x,y)}{\partial x} \\ -\frac{\partial f(x,y)}{\partial y} \\ 1 \end{matrix} \right|^{-1} \begin{bmatrix} -\frac{\partial f(x,y)}{\partial x} \\ -\frac{\partial f(x,y)}{\partial y} \\ 1 \end{bmatrix} \right|_{\overline{P}_{\vec{R}'}} \tag{2.13}$$

The incident ray and the normal vector are now known, so that it is now possible to calculate the angle between both vectors as:

$$\begin{cases} \theta_{\vec{R}',\vec{S}} = \vec{N} \cdot \begin{bmatrix} k_{\vec{R}'} \\ l_{\vec{R}'} \\ m_{\vec{R}'} \end{bmatrix} \\ \vec{N}_{\vec{R}',\vec{S}} = \vec{N} \times \begin{bmatrix} k_{\vec{R}'} \\ l_{\vec{R}'} \\ m_{\vec{R}'} \end{bmatrix} \end{cases} \tag{2.14}$$

, where $\theta_{\vec{R}',\vec{S}}$ is the angle between both vectors, and $\vec{N}_{\vec{R}',\vec{S}}$ defines the plane in which the incident and outgoing rays lie. The final step in determining the outgoing ray is the calculation of the exit angle using the laws of reflection and refraction for geometric optics (Equation 2.15).

$$\begin{cases} \text{Reflection} \rightarrow & \theta'_{\vec{R}',\vec{S}} = -\theta_{\vec{R}',\vec{S}} \\ \text{Refraction} \rightarrow & \theta'_{\vec{R}',\vec{S}} = \arcsin(\frac{n}{n'} \sin(\theta_{\vec{R}',\vec{S}})) \end{cases} \tag{2.15}$$

Based on Equation 2.15, the resulting ray, after the refraction or the reflection on the surface $\vec{S}$, can be calculated according to Equation 2.16, where $\mathbf{ROT}_{\vec{N}_{\vec{R}',\vec{S}}}(\theta'_{\vec{R}',\vec{S}})$ is a rotation of $\theta'_{\vec{R}',\vec{S}}$ around the vector $\vec{N}_{\vec{R}',\vec{S}}$.

$$\vec{R}'_{final} = \overline{P}_{\vec{R}'} + \mathbf{ROT}_{\vec{N}_{\vec{R}',\vec{S}}}(\theta'_{\vec{R}',\vec{S}}) \begin{bmatrix} k_{\vec{R}'} \\ l_{\vec{R}'} \\ m_{\vec{R}'} \end{bmatrix} t \tag{2.16}$$

Once the resulting ray is determined, now it needs to be transformed back into the global coordinate system as shown in Equation 2.17.

$$\vec{R}_{final}(t) = T\vec{R}'(t) \tag{2.17}$$

The whole process is then recursively repeated until all surfaces and all rays are processed.

2.1.4 Optical Aberrations

The paraxial approximation considers only rays that are near the optical axis, forming infinitesimally small angles with it. However, depending on the position of an object, these assumptions are often not fulfilled and deviations occur. These deviations from the ideal geometric optic model are defined as optical aberrations [Haf94, Hec02, Bas95]. Figure 2.4 shows a diagram of the models used to describe how light interact with optical systems and their validity.

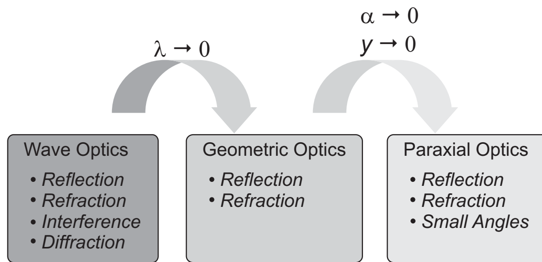

Figure 2.4: Models for optical imaging.

Optical aberrations can be interpreted as the difference between the paraxial and the geometric models. They can be divided in two main groups, monochromatic and chromatic aberrations. Chromatic aberrations occur due to the dependence of the index of refraction to the wavelength of light. Since the focal length of a lens depends on this index, it also changes with the wavelength of light. On the other side, monochromatic aberrations arise from the inaccuracies of the paraxial approximation. They are caused by the errors that arise from the first-order approximation $\sin(x) = \tan(x) = x$ used in the paraxial approximation.

The analytical evaluation of these errors was firstly done by Seidel and Petzval. Using the first two terms of the Taylor series shown in Equation 2.18, they developed the third-order aberration theory where the primary aberrations are spherical, coma, astigmatism, field curvature and distortion (Figure 2.5).

$$\sin(x) = x - \frac{x^3}{3!} + \frac{x^5}{5!} - \frac{x^7}{7!} + \cdots \tag{2.18}$$

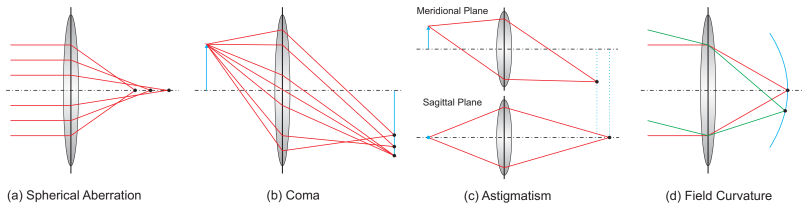

Figure 2.5: Third-order optical aberrations.

The first aberration term, the spherical aberration, results from the fact that the focal length of a spherical lens depends on the distance between a ray and the optical axis. This way, for a converging lens, an off-axis ray will be focused closer to the lens than a paraxial ray, as shown in Figure 2.5a, so that a point will not be imaged in a point.

The second aberration is the coma. It can be observed when off-axis points are imaged, resulting in a cone-shaped image as shown in Figure 2.5b. This happens due to the variation in the magnification of off-axis rays caused by the curvature of the lens and makes clear the dependence between magnification and system's aperture in a spherical lens.

The third Seidel aberration is the astigmatism. As the cone of rays from a point off-axis strikes the lens asymmetrically, two different focal planes are produced in the meridional and sagittal planes (Figure 2.5c). Due to astigmatism a point imaged by a converging lens will produce a vertical line at one image plane and a horizontal line at the other.

Field curvature or Petzval field curvature arises from the fact that a spherical lens does not image a plane to a plane, but rather to a curved surface as shown in Figure 2.5d.

The final third-order aberration is the distortion. It occurs due to the variation of the lens magnification depending on the distance to its centre so that straight lines are not imaged accurately as straight lines. Distortion deforms an image, but do not modify its focal position. If the magnification decreases as the distance from the centre increases, then barrel distortion is observed. When magnification increases with distance, pincushion distortion is observed. Figure 2.6 illustrates both types of distortion.

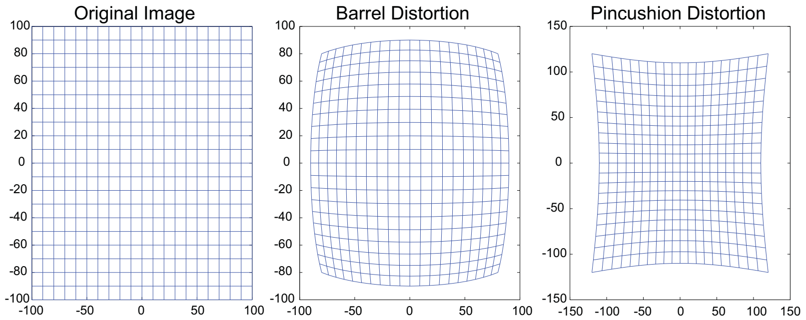

Figure 2.6: Barrel and pincushion distortion in a grid.

Every optical system exhibit some combination of the aberrations discussed above and, in addition to these aberrations, there are still other higher order aberrations that often also need to be considered. The standard way to avoid these aberrations is to combine different lenses and other optical components, building complex optical systems, so that the optical aberrations can be minimized below certain tolerance levels for a given operation range. This is often done with the use of ray-tracing simulations together with mathematical optimization tools.

2.2 Confocal Microscopy

Optical microscopy started in the 17th century in the Netherlands and is today one of the most widely used scientific tools worldwide [Rie88]. The goal of optical microscopy is the use of optical systems to generate a magnified image of a sample and make different features from these objects visible. The generated image can then be observed directly by the eye or with a camera.

There are a large number of different techniques in optical microscopy, and an uncountable number of applications and instruments. Most of these instruments have the compound microscope as base. Figure 2.7 illustrates the typical design of a compound microscope and its associated optical path.

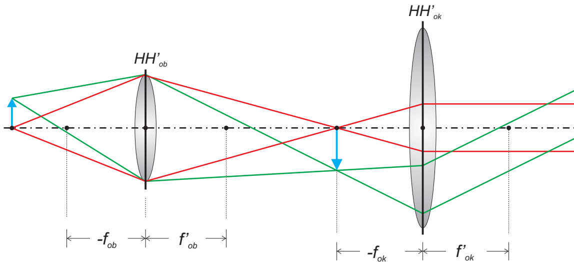

Figure 2.7: Basic compound microscope and its optical path.

The compound microscope is basically composed of two lenses. The objective lens (HH'_{ob}) creates a magnified real image of the object and this image is observed with the ocular (HH'_{ok}). Microscopes are indispensable in many research fields and are widely described in the literature. Haferkorn [Haf94], Naumann [NS92] and Hecht [Hec02] present an insightful discussion of the basic properties and characteristics of these systems as well as many design considerations and Riesenberg [Rie88] describes many different applications and techniques.

Confocal scanning microscopy is one of the many types of optical microscopy. It is today a standard investigation tool in material, medical and biological sciences. It also plays an important role in the field of surface measurements and is a promising technology in high-end

application areas, such as micro- and nanotechnology [Bit03, Fab09, Web96]. Its first concepts (Figure 2.8) were originally developed by Minsky in 1957 [Min61], but, due to the lack of suitable light sources for imaging and of the necessary computer power to process all the required amount of data, the first practical confocal scanning microscopes were developed only in the 1970's by, among others, Egger and Petran and Brakenhoff [CK96].

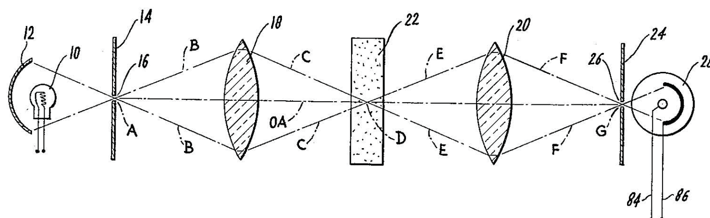

Figure 2.8: Misky's confocal microscope [Min61].

The main idea behind Minsky's microscope was to develop an optical system capable of rejecting all scattered light, except that emanating from a single focused point. Therefore, blurring could be strongly reduced and contrast and resolution enhanced. Basically, confocal scanning microscopy is a technique for increasing contrast and resolution in optical imaging systems through the rejection of out-of-focus light. Images are acquired point-by-point and reconstructed with a computer, allowing optical sectioning, expanding the optical limits of conventional microscopes and offering fast, accurate and repeatable measurements.

Figure 2.9 illustrates diagrammatically the basic principle of modern confocal microscopes. A light beam, normally a laser beam, is firstly collimated and then focused on the sample's surface. The scattered and the reflected light are then collected by the same objective used to focus the light and, with the help of a beam splitter and a second lens, focused on a pinhole. Behind the pinhole, a detector (normally a photomultiplier detector or a CCD chip) is responsible for measuring the light intensity that comes through. When the sample is out of focus, the light intensity measured in the detector is strongly reduced. This way most of the light that comes from points above or below the objective focal plane is blocked by the pinhole and does not contribute to the image formation.

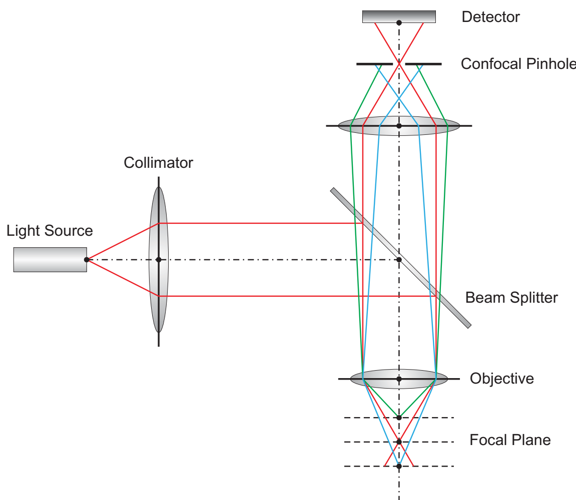

Figure 2.9: Basic principle of confocal microscopes.

Nevertheless Figure 2.9 illustrates the measurement of a single point in a sample. For having an areal measurement it is necessary to scan the samples. There is a wide variety of methods for achieving this scanning, going through the use of linear stages for moving the sample in X, Y and Z directions until the use of Nipkow disks or acusto-optical modulators (AOMs) for moving the laser spot. Webb [Web96], Claxton *et.al.* [CFD05] and Sheppard [SS97] describe and discuss these methods and offer a detailed overview. In general, the scanning methods can be divided in two major groups: stage scanners and beam scanners.

Stage scanners move the sample while keeping the laser spot fixed in one position. The main advantages of this configuration are that all lenses work on axis and the field of view is not limited by the optics. However, it presents some major drawbacks. It is often difficult to move large samples, especially if it must be done fast. Because of this major drawback, almost all modern confocal microscopes are based on beam scanners [Web96, Mar91, Mar85, CFD05] and the mostly used approach is based on the use of a pair of galvanometer mirrors [Web96, SS97].

2.3 Resolution Limits of Optical Instruments

The lateral resolution of an optical instrument can be seen as a measure of its ability to distinguish two separated point objects [Hec02, Gro03] and defines the size of the smallest feature of an object that can still be resolved by the optical system. It is ultimately limited by diffraction. Due to the finite aperture of the optical system, a radiating point source will not be imaged as a point, but will have a finite size. The form, or intensity distribution, of this imaged point source is defined as the point spread function (PSF) of an optical system and is a measure of its resolving power. The narrower the point spread function is, the better the resolution of the system will be.

In a paraxial optical system with a circular aperture, the PSF can be obtained through the Fraunhofer diffraction [Hec02, Haf94]. The light is first diffracted by the finite aperture and generates a diffraction image. This image is then imaged by the optical system and the resulting PSF in the focal plane is described by the rotationally symmetric Airy pattern shown in Figure 2.10.

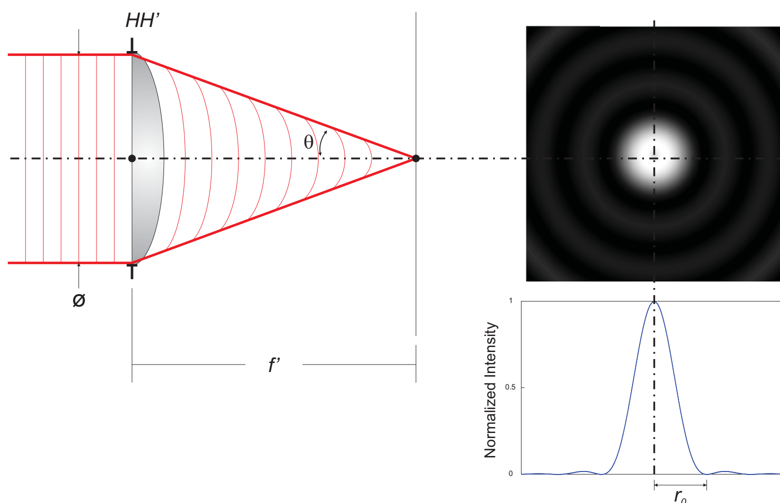

Figure 2.10: Fraunhofer-diffraction on a circular aperture.

The size of the resulting Airy pattern will depend on the numerical aperture (NA) of the lens. The NA describes the ability of a lens to gather light and is important to determine its resolution limits. It depends of the half aperture angle (θ) and the refraction index of the medium (n) and is defined as shown in Equation 2.19.

$$NA = n \sin(\theta) \tag{2.19}$$

The most well known resolution criterion is the Rayleigh criterion. It says that for two incoherent point sources to be still resolved by an optical instrument, the maxima of one of the imaged Airy disks must be at least coincident with the first minimum of the second Airy disk. This way the minimum separation between two features is given by Equation 2.20, where λ is the wavelength of the light and NA is the numerical aperture of the optical system.

$$d_{min} = \frac{0.61\lambda}{NA} \tag{2.20}$$

The Rayleigh criterion is considered a conservative measure of the spatial resolution of an optical instrument [Hec02, Gro03]. Another widely used criterion is the Sparrow criterion [Hec02, GVY05]. It considers the fact that two Airy disks can still be detected as long as a minimum exists between their maxima. This way the smallest separation between two points, so that both are still distinguishable is:

$$d_{min} = \frac{0.47\lambda}{NA} \tag{2.21}$$

Figure 2.11a and Figure 2.11b illustrate the Rayleigh and the Sparrow criteria respectively.

The Rayleigh and Sparrow criteria are widely used for astronomic telescopes, as stars can be well approximated as incoherent point sources. Nevertheless, for microscopy applications where often partially coherent light is used and the objects are mostly not self-luminous, the Abbe resolution limit offers a better estimate.

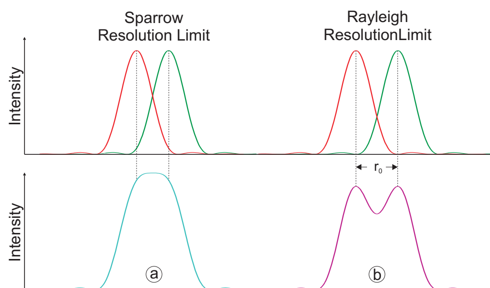

Figure 2.11: Rayleigh and sparrow resolution criteria.

In order to estimate the resolution limit of optical instruments, Ernst Abbe used a periodic grating. The grating diffracts the light and, depending on the aperture angle of the optical system, different diffraction orders are filtered. Abbe defined that for an image to be resolved, at least the 0th and the 1st diffraction orders should still be imaged by the optical system. This way the resolution limit of an optical system is given by Equation 2.22.

$$d_{min} = \frac{0.5\lambda}{NA} \tag{2.22}$$

In the special case of confocal microscopy, the resolution can still be slightly improved. If the pinhole is chosen to have a radius smaller than the radius of the Airy disk (r_0), the diffraction of the light on the pinhole starts to have a significant influence on the system so that the resolution limit is improved as shown in Equation 2.23.

$$d_{min} = \frac{0.37\lambda}{NA} \tag{2.23}$$

Nevertheless it is important to consider the fact that all the discussed theoretical resolution limits consider the use of a perfect optical system without any optical aberrations, what in practice is not possible. Therefore, the resolution achieved by an optical instrument is always inferior to its theoretical limit. For standard compound light microscopes with numerical apertures of approximately 1.0 and white light illumination ($\lambda \approx 500nm$), the best achievable resolution is around $2\mu m$.

2.4 Auto-focus in Optical Systems

Due to the overwhelming demand of the industry, especially in the field of optical data storage (CD, DVD, MD, Blue-Ray), a large variety of methods and sensors have been developed for focus point detection [Mas05,Mar91,Coh87,MS97,CNY$^+$00,The88]. The detection of the focus error signal (FES) is a key task in those systems and many methods such as the astigmatic method, the Foucault knife-edge method, the beam offset method, the critical angle prism method, the spot size method have been adopted and are extensively described in the literature. Most of those techniques rely on the use of a detection lens to create a secondary focused spot, so that deviations from the focusing on the sample cause a change in the shape, size or position of the secondary spot.

From all these methods the two most widely used are the astigmatic and the Foucault knife-edge methods [Mas12, MS97, The88, Mer84]. Barthel [Bar85], Theska [The88], Cohen [Coh87] and many other authors [Mar91, CNY$^+$00, MMJ04, She93, HBVS03] have thoroughly described and studied these various focus point detection methods in the literature, therefore in this chapter only the astigmatic and the knife-edge methods, as the most widely used ones, will be presented in detail.

2.4.1 Astigmatic Method

The astigmatic method, developed by Bricot [BL76] in 1976, is the most used focus point detection method and offers a good compromise between sensitivity and acquisition range [CNY$^+$00]. The basic diagram of the astigmatic method is illustrated in Figure 2.12. The main elements of the system are the light source, the collimation optics, the focusing optics, the detection optics and the quadrant photodiode for detecting the light intensity distribution.

A collimated light beam is focused on the sample's surface and the reflected light is collected by the same focusing optics. With the help of a beam splitter the light is directed towards the detection optics where a combination of a converging lens and a cylindrical lens focus the light in a quadrant photodiode. The cylindrical lens is responsible for the

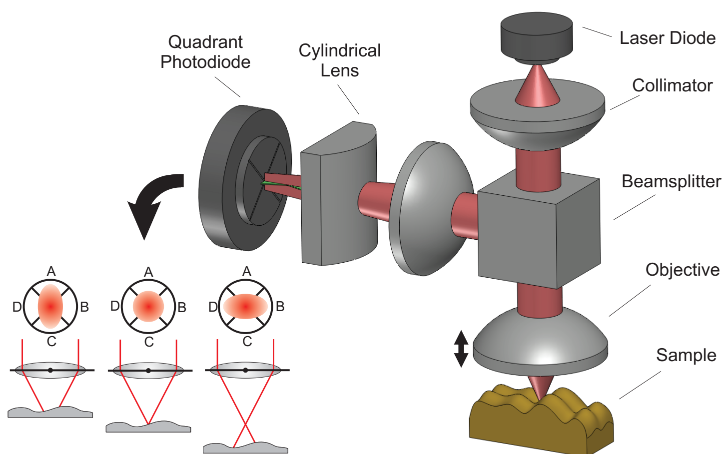

Figure 2.12: Diagram of the astigmatic method for detection of the focus error signal (FES).

astigmatism in the system. This way, the focal distance in the XZ and YZ planes is different and only a small region between these two focal lines has a balanced circular intensity distribution on the four photodiodes of the detector, as illustrated in Figure 2.12. The same results can also be achieved through the use of astigmatic lenses [The88].

If the sample's surface does not lie on the focal plane of the objective lens, the astigmatism in the system inserts a distortion in the circular form of the light spot on the quadrant photodiode. This deformation can then be measured using Equation 2.24, where V_A, V_B, V_C and V_D are the voltages in the photo detectors in Figure 2.12.

$$FES = \frac{(V_A + V_C) - (V_B + V_D)}{(V_A + V_B + V_C + V_D)} \tag{2.24}$$

These voltage values are proportional to the light intensity on the photodiodes and the resulting signal FES is a non-linear bipolar function whose typical form is illustrated in Figure 2.13. This function characterizes the position of the sample in reference to the focal plane of the objective lens.

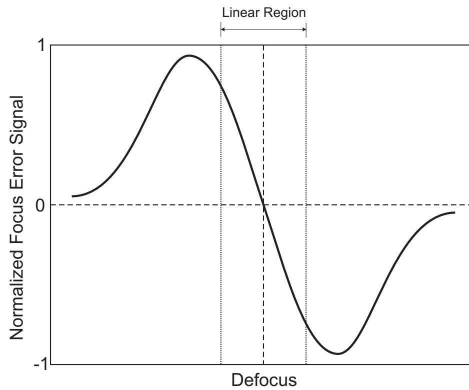

Figure 2.13: Typical focus error signal (FES) curve.

All focus detection methods generate a curve with a basic shape similar to the curve illustrated in Figure 2.13 [Coh87]. This curve is also known as S-Curve and is used to control the position of the objective lens, so that the sample (e.g. an optical disk) is always in focus.

One of the main disadvantages of the astigmatic method is the large number of required optical components and the associated adjustments and design considerations. However, many technical developments have been made in the last years and the number of components in the system drastically reduced through integration techniques [YMO+00, BR91].

Using the thin lens approximation [Hec02, Haf94], the light path in an astigmatic system can be described as shown in Figure 2.14. At first, the light source, with an aperture angle θ_L, is collimated using a lens with a focal length f_c. The collimated beam is then focused using an objective with focal length f_{ob} and is reflected back into the objective by the sample. The sample is located at a distance d_s from the objective lens, corresponding to a defocus of δ. The light beam, collected by the objective, is then focused on the quadrant diode using an astigmatic optic.

The astigmatic optic is modelled using a thin lens with two different focal lengths f_y and f_x in the meridional (YZ) and tangential (XZ) planes respectively. The distances between the objective lens, astig-

matic lens and quadrant diode are given by d_1 and d_2 and are illustrated in Figure 2.14.

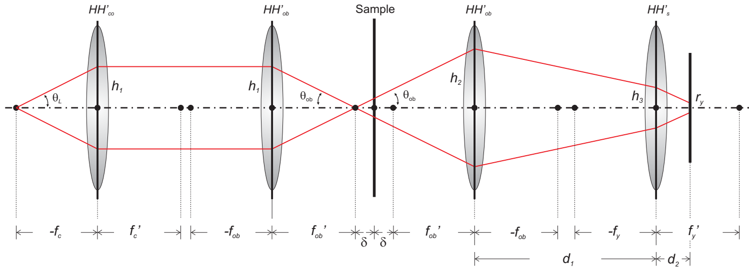

Figure 2.14: Beam path of the collinear astigmatic method.

Given the aperture angle θ_L and the focal length of the collimation and focusing lenses, the angle θ_{ob} and the radial distances h_1 and h_2 can be calculated as:

$$\tan(\theta_{ob}) = \frac{f_c}{f_o} \tan(\theta_L) \tag{2.25}$$

$$h_1 = f_c \tan(\theta_L) \tag{2.26}$$

$$h_2 = \frac{h_1}{f_{ob}}(f_{ob} + 2\delta) \tag{2.27}$$

Using the Newtonian form of the thin lens equation (Equation 2.3), the value h_3 can be calculated according to Equation 2.28:

$$h_3 = h_1 + \frac{2h_1(f_{ob} - d_1)}{f_o^2}\delta \tag{2.28}$$

Now, considering the astigmatic lens in two separated planes (Figure 2.15) the radii r_x and r_y of the light spot on the quadrant diode can be determined as shown in Equation 2.29.

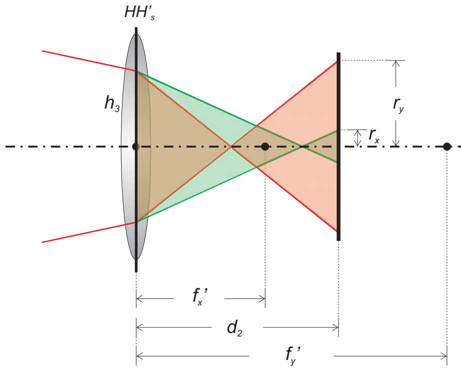

Figure 2.15: The two planes of the astigmatic lens.

$$\begin{cases} r_x = h_1\left(1 - \frac{d_2}{f_x^2}\right) + \frac{2h_1}{f_{ob}^2 f_x}\left[f_x(f_{ob} - d_1 - d_2) - d_2(f_{ob} - d_1)\right]\delta \\ r_y = h_1\left(1 - \frac{d_2}{f_y^2}\right) + \frac{2h_1}{f_{ob}^2 f_y}\left[f_y(f_{ob} - d_1 - d_2) - d_2(f_{ob} - d_1)\right]\delta \end{cases} \tag{2.29}$$

The radii r_x and r_y represent the major and minor radii of the ellipse projected on the quadrant diode by the astigmatic lens and are directly dependent on the defocus δ. The distance d_2 between the quadrant diode and the astigmatic lens should be chosen to avoid an offset of the S-Curve, so that the zero-crossing of the curve represents the point where the defocus δ is zero. This is accomplished by setting d_2 according to Equation 2.30, so that when the light is exactly focused on the sample, a circle will be project on the quadrant diode and the FES will be zero.

$$|r_x|_{\delta=0} = |r_y|_{\delta=0} \rightarrow d_2 = 2\frac{f_x f_y}{f_x + f_y} \tag{2.30}$$

Once both radius of the projected ellipse in the quadrant diode have been determined (Equation 2.29), the next step to derive the FES is to define the energy distribution on the diodes.

Photodiodes are semiconductor devices capable of converting light into an electric signal. The generated voltage or current is proportional

to the energy received and therefore to the energy distribution of the incident light on the detector active surface. Many different functions have been used in the literature [CGLL84, Mas12, HBVS03] to approximate this distribution, but, as the mostly used light source for *FES* generation are laser diodes, a Gaussian distribution presents itself as the most appropriate.

The energy distribution of the light spot on the detection surface can be described with a two-dimensional Gaussian distribution [Hec02] as shown in Equation 2.31, where r_x and r_y are the radii of the beam where the energy is reduced by a factor of $(1/e^2)$ and (x, y) describe a point in the detection surface of the quadrant diode.

$$I(x,y,\delta) \sim \frac{1}{r_x(\delta) r_y(\delta)} \exp\left(-2\left(\frac{(x-x_0)^2}{r_x(\delta)^2} + \frac{(y-y_0)^2}{r_y(\delta)^2}\right)\right) \tag{2.31}$$

x_0 and y_0 define the centre of the quadrant diode, so that, in the ideal case, when the laser diode is positioned exactly on the optical axis, their values are zero.

In order to determine the voltage generate by each quadrant of the diode, it is necessary to integrate the energy distribution function over their active surfaces. Using as reference a coordinate system aligned with the quadrant diode (Figure 2.16) the projected ellipse is rotated 45 degrees. To take this rotation in consideration, Equation 2.31 can be expanded according to Equation 2.32, where φ is the rotation angle of the projected ellipse.

$$\begin{cases} I(x,y,\delta) \sim \frac{1}{r_x r_y} \exp\left(-2\left(a(x-x_o)^2 + 2b(x-x_o)(y-y_o) + c(y-y_o)^2\right)\right) \\ a = \frac{\cos^2\varphi}{r_x(\delta)^2} + \frac{\sin^2\varphi}{r_y(\delta)^2} \\ b = -\frac{\sin 2\varphi}{r_x(\delta)^2} + \frac{\sin 2\varphi}{r_y(\delta)^2} \\ c = \frac{\sin^2\varphi}{r_x(\delta)^2} + \frac{\cos^2\varphi}{r_y(\delta)^2} \end{cases} \tag{2.32}$$

Now, the integration intervals for each quadrant can be easily defined and the voltage signals generated are given by Equation 2.33, where h_{min} and h_{max} are geometrical characteristics of the quadrant diode as illustrated in Figure 2.16 and the *FES* function (Equation 2.24), is fully defined.

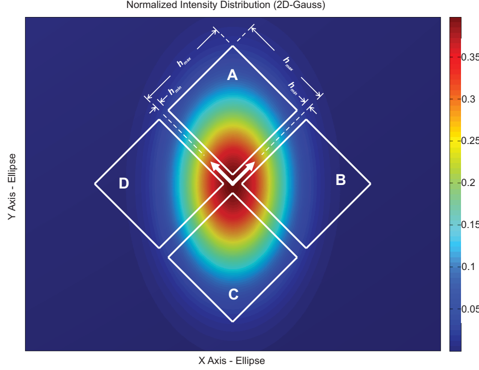

Figure 2.16: Two-dimensional gaussian distribution on the quadrant diode.

$$\begin{cases} V_A \sim \int_{h_{max}}^{h_{min}} \int_{h_{min}}^{h_{max}} I(x,y,\delta)\partial y \partial x \\ V_B \sim \int_{-h_{min}}^{-h_{max}} \int_{h_{min}}^{h_{max}} I(x,y,\delta)\partial y \partial x \\ V_C \sim \int_{-h_{min}}^{-h_{max}} \int_{-h_{max}}^{-h_{min}} I(x,y,\delta)\partial y \partial x \\ V_D \sim \int_{h_{max}}^{h_{min}} \int_{-h_{max}}^{-h_{min}} I(x,y,\delta)\partial y \partial x \end{cases} \tag{2.33}$$

It is important to take in consideration that the model derived in this section does not take in consideration neither the wave nature of the light or the effects of optical aberrations. The wave nature of the light can be partially introduced in the model through the propagation of Gaussian beams through thin lenses [Mas12], but for the evaluation of diffraction effects and optical aberrations, numeric simulations are necessary [CGLL84, Coh87, BM94, BM92].

2.4.2 Foucault Knife-Edge Method

The knife-edge principle was developed by Leon Foucault in 1859 to test astronomical mirrors and is until today a cost effective and easy way to test for deformations on optical surfaces such as large mirrors and aspheres. Figure 2.17 shows the basic schema of the knife-edge principle for focus detection.

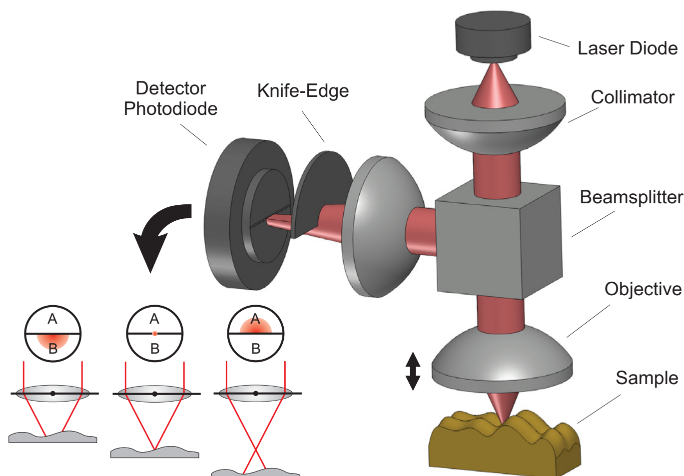

Figure 2.17: Diagram of the knife-edge method for detection of the focus error signal (FES).

A knife edge is placed on the focal plane of the detection lens and behind it a detector consisting of two photodiodes. When the object is exactly focused no obstruction occurs on the light path and both photodiodes are equally illuminated as shown in Figure 2.17. If the sample is defocused, the light path will be obstructed by the knife edge and the energy distribution on the detector will be asymmetric. This asymmetry is used to measure the defocus using Equation 2.34, where V_A and V_B are the voltages generated by each one of the photodiodes illustrated in Figure 2.17.

$$FES = \frac{(V_A - V_B)}{(V_A + V_B)} \tag{2.34}$$

Different implementations of the knife-edge method are described by many authors [YMO$^+$00,Mas12,Coh87,BM94], but they all rely on the basic principle developed by Foucault.

In an analogous way to that used for the astigmatic method, the knife-edge method shown in Figure 2.17 can also be modelled using geometric optics and the thin lens approximation. The light source is

collimated and then focused on the sample. The probe, at a distance $d_s = f_{ob} + \delta$ from the objective lens, reflects the light back into the objective and the light beam is then focused on the detector. Figure 2.18 shows the light path in the knife-edge detection method.

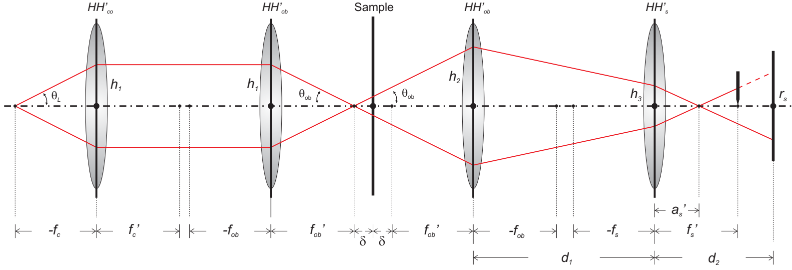

Figure 2.18: Beam path of the knife-edge method.

The first part of the system is similar to the astigmatic method, so that h_1, h_2 and h_3 are given by Equations 2.26, 2.27 and 2.28 respectively. Considering the detector lens with a focal length f_s and the photodiodes positioned at a distance d_2 from the lens, the radius r_s of the laser spot on the sensor can be calculated as shown in Equation 2.35 and the distance a_s', where the light is focused after the sensor's lens, as shown in Equation 2.36

$$r_s = h_1 \left(1 - \frac{d_2}{f_s^2}\right) + \frac{2h_1}{f_{ob}^2 f_s} \left[f_s(f_{ob} - d_1 - d_2) - d_2(f_{ob} - d_1)\right] \delta \quad (2.35)$$

$$a_s' = f_s - \frac{2 f_s^2 \delta}{f_o^2 + 2\delta(f_{ob} + f_s - d_1)} \quad (2.36)$$

The radius r_s represent the radius of the laser spot projected on the diode without the knife edge. Using a two-dimensional Gaussian distribution and taking the values of a_s' as a decision criterion, the energy distribution of the light spot on the detection surface of the photodiode can be described by Equation 2.37 and the voltage generated by each

one of the two photodiodes determined as shown in Equation 2.38. The FES is then given by Equation 2.34.

$$I(x,y,\delta) \sim \begin{cases} \frac{1}{r_s(\delta)^2} \exp\left(-\frac{2}{r_s(\delta)^2}\left((x-x_0)^2+(y-y_0)^2\right)\right) & \text{if } y \leq 0, a'_s \leq f_s \\ 0 & \text{if } y > 0, a'_s < f_s \\ \frac{1}{r_s(\delta)^2} \exp\left(-\frac{2}{r_s(\delta)^2}\left((x-x_0)^2+(y-y_0)^2\right)\right) & \text{if } y \geq 0, a'_s \geq f_s \\ 0 & \text{if } y < 0, a'_s > f_s \end{cases} \quad (2.37)$$

$$\begin{cases} V_A \sim \int_{-h_{max}}^{h_{max}} \int_{h_{min}}^{h_{max}} I(x,y,\delta)\partial y \partial x \\ V_B \sim \int_{-h_{max}}^{h_{max}} \int_{-h_{max}}^{h_{min}} I(x,y,\delta)\partial y \partial x \end{cases} \quad (2.38)$$

One of the most widespread variation of the Foucault knife-edge principle is the obscuration method [YMO+00, BM94]. In this focus detection method the detector element is placed in the focal plane of the detection lens instead of the knife edge, and the knife-edge itself is placed near the lens to obstruct half of the light path. Figure 2.19 shows a schematic of this detection method.

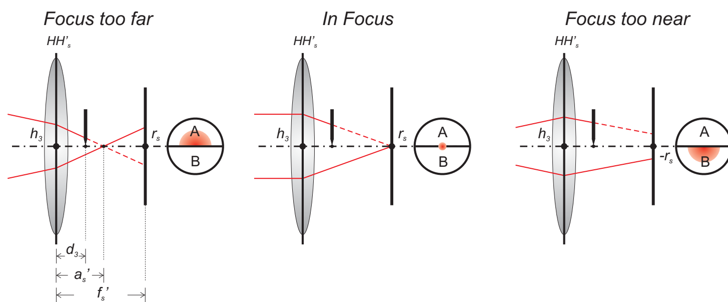

Figure 2.19: Focus error detection with the obscuration method.

The evaluation of the focus error is similar to that of the knife-edge method. The energy distribution of the light spot on the detection surface of the photodiode and the FES are also given by Equations 2.37, 2.38 and 2.34 with $d_2 = f_s$.

2.5 Optical Scanning

Focus point detection allows the measurement of the defocus in the system and therefore the measurement of the height of a single point in a sample along the optical axis. Besides this axial measurement, in order to implement an areal measurement, a lateral scanning must also be implemented. As discussed in Chapter 2.2, optical scanning methods can be divided in two major groups: stage scanners and beam scanners. In this chapter a short overview on beam scanners is presented.

Optical beam scanners are used in a wide range of applications from data storage and barcode readers to confocal microscopy and industrial measurements [Mar85,Mar91]. They can be divided in three basic types [Cho06, Mar91, Bei95]: Post-Objective Scanning, Pre-Objective Scanning and Objective Scanning. Figure 1 shows a diagram of each one of these basic types.

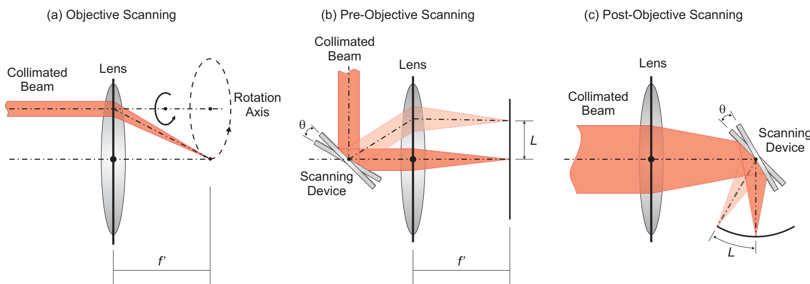

Figure 2.20: Types of optical beam scanning.

Objective scanning (Figure 2.20a) is achieved through the movement of the focusing lens while the incident beam stays still and pre- and post-objective scanning utilize an additional deflecting unity to direct the beam. In pre-objective (Figure 2.20b) this deflections is done before the focusing optic and in the post-objective (Figure 2.20c), after. Each configuration has its advantages and disadvantages regarding linearity of the scanning, scan field, resolution and optical characteristics [Cho06, Mar91, Bei95, GT10]. The most commonly used configuration is the pre-objective scanning, especially in the field of microscopy, where high numeric aperture (NA) objectives are normally

used. Specifically in confocal microscopy, the Nipkow disk, scanning mirrors and microlenses are the most common methods. There is a large variety of other methods for lateral scanning, such as fiber optic scanning [CK96], digital mirror matrixes [Bit03] and holographic scanners [Mar91], but as lateral scanning is not the main topic of this work, only the most common methods are briefly discussed. Figure 2.21 illustrates the basic principle of these methods.

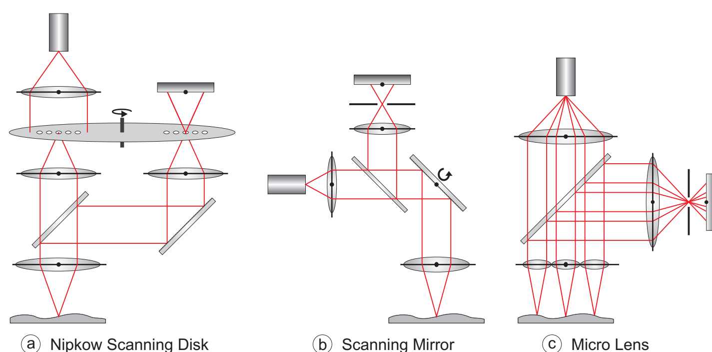

Figure 2.21: Lateral scanning in confocal microscopy.

The Nipkow disk scanning (Figure 2.21a) was firstly proposed by Petran and Hadravsky [CK96,Web96]. It uses a two-sided disk to achieve the lateral scanning through the displacement of the confocal aperture. While the disk is illuminated on one of its sides, the image is observed through a conjugate set of pinholes on the opposite side of the disk. In order to avoid alignment problems, a one sided variant, where the same aperture is used for illumination and imaging, is also widely used [CK96, SS97]. One of the biggest advantages of the use of the Nipkow disk is the possibility of using parallel processing. Using a disk with several thousand of pinholes arranged in multiple interleaved spirals and illuminating many of these pinholes at the same time, image rates of up to several hundred per second can be achieved. Corle and Kino [CK96] present a detailed discussion on this scanning technique.

The use of scanning mirrors is another widely used method for lateral scanning in confocal microscopy. As shown in Figure 2.21b, a collimated beam is deflected using a mirror. Considering the objective as

a perfect lens (paraxial approximation), the lateral displacement d of the focus spot is then given by Equation 2.39, where θ is the mirror rotation angle and f the focal length of the objective.

$$d = f \tan(2\theta) \tag{2.39}$$

The light reflected by the probe is then descanned by the same mirror and focused on the imaging pinhole. Confocal microscopes employing scanning mirrors often use laser sources for illumination and are called Confocal Laser Scanning Microscopes (CLSM). Typically, CLSM systems include high-end objectives and additional sophisticated optical systems to compensate for optical aberrations that arise as the system does not work on-axis. Other possibility to address this problem, based on the use of correction algorithms, is presented in Chapter 4.2 and is one of the subjects addressed in this work.

Another possibility to achieve a lateral scanning is the use of microlens arrays. A microlens array is an arrangement of small lenses ranging from $1mm$ down to a few μm. With the use of such an array, thousands of small confocal systems can be build in parallel as shown in Figure 2.21c.

2.6 Modern Confocal Laser Scanning Microscopy

Modern laser scanning microscope designs are centred on conventional upright or inverted optical microscope arrangements and the use of standard high-end objective lenses with a high numerical aperture, for which there is a large design experience basis [Bit03, Fab09, Web96, XRJR07]. The basic diagram shown in Figure 2.9 does not represent the reality of these systems. Confocal laser scanning microscopes are designed as complete stand-alone units with multiple detection and excitation channels, complex optics for beam conditioning, high-end objective lenses, variable pinholes, beam scanners, as well as a manifold of electronic components for operating and controlling these components.

Although a brief overview of these components was presented in previous chapters, a detailed description is not in the scope of this work. Pawley [Paw06], Sheppard [SS97] and Corle [CK96] made a broader study of traditional confocal laser scanning microscopy and describe thoroughly each one of these components and their characteristics.

Modern confocal laser scanning microscopes are relatively large and are not intended for integration with other measuring systems. Table 2.1 shows a short summary of the typical size and scanning frequency of commercial available confocal laser scanning systems.

Table 2.1: Typical characteristics of commercial confocal scanning systems.

Property	Value
Frame Rate	5 fps (500x500 Pixels)
Size	$(350 \times 450 \times 500)mm$

In order to measure the 3D topography of a sample, traditional confocal microscopes need to acquire a stack of optical slices from the sample and merge them together [CFD05, Web96, SS97]. This way the acquisition times shown in Table 2.1 are normaly reduced by an average factor of 40 or higher depending on the complexity of the sample and the desired axial resolution.

As explained in Chapter 1.2, one of the objectives of this work is the simplification and miniaturization of confocal laser scanning microscopes, making their integration with other systems viable. The combination of optical scanning techniques (Chapter 2.5) and auto-focus methods (Chapter 2.4) offers new possibilities to the design of scanning microscopes and has a large potential for improving miniaturization, costs and measuring frequencies.

Chapter 3

Design and Development of a Simplified Scanning Microscope

The developed measuring system is based on the basic concepts of confocal microscopy and auto-focus detection presented on Chapter 2 and offers an alternative way to overcome the use of complex compensated optical systems, that will be discussed in details in Chapter 4.2.

In this chapter a detailed description of the designed scanning microscope is presented. Its complete optical design is shown and discussed and the lateral and axial scanning procedures are explained.

3.1 Basic Design

In order to keep the number of optical elements minimal, the system was designed using a suboptimal optical schema and has its functionality defined through three main modules and two optical groups. A 2D tilting mirror, a linear stage and a focus detection sensor compose the three main functional groups and a collimation/sensor lens and an objective lens the optical groups. Figure 3.1 shows a schematic drawing of the system's configuration with its main components and optical path.

The system uses a hologram laser unit from conventional DVD tech-

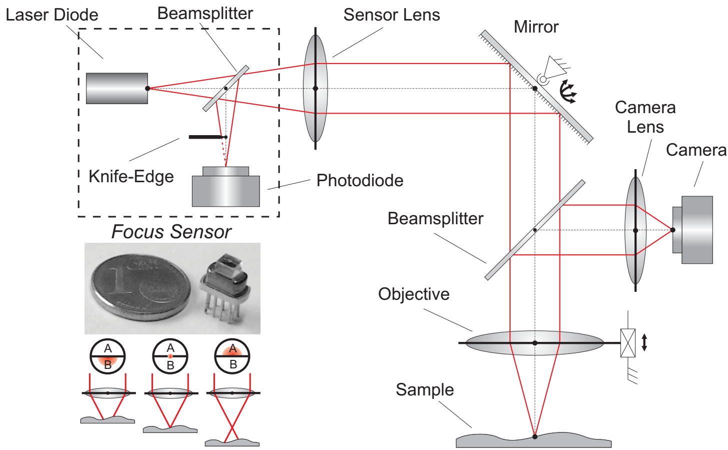

Figure 3.1: Optical schema of the scanning system and its main components.

nology [Mas05, Mas12, YMO+00] that generates a single beam with a wavelength of 654nm. The generated beam is collimated and then deflected with a 2D tilting mirror. The deflected laser is then focused on the sample through the objective. The laser reflects on the sample and returns through the objective to the mirror where it is descanned and reflected back into the hologram laser unit, where the focus detection system is integrated.

The hologram laser unit is based on the obscuration method explained in Chapter 2.4.2 and is composed by three main components: a laser diode, a holographic optical element (HOE) and a six-segment photodiode (Figure 3.2a).

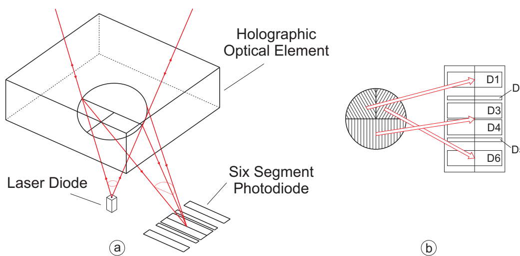

Figure 3.2: Miniaturized hologram laser unit [YMO+00].

The HOE consists of a hologram diffraction pattern. It directs the returning beam towards the photodiode and acts as a knife-edge for the focus detection. The patterns of the HOE and the photodiode, illustrated in Figure 3.2b, are responsible for generating the focus error signal (FES). The hologram pattern has three regions in which the directions of the grating are different and the photodiode has six segments ($D1$ to $D6$). Part of the light, diffracted by the semicircular shape of the hologram pattern, is focused on the gap between the segments $D3$ and $D4$ and is used for generating the FES. The semicircular shape acts as the knife-edge and the segments $D2$ and $D5$ are auxiliary segments for enhancing the FES signal [YMO+00]. The light focused on the segments $D1$ and $D6$ is used by DVD systems for measuring the sideways deviation of the laser spot from the centre of an information track and was not used.

The hologram laser unit delivers two output signals. The first one (SUM) is a measure of the total energy collected by the photodiodes and the second one (DIF) the non-normalized measure of the defocus. This way, the normalized focus error signal (FES) will be given by Equation 3.1, where $V2$, $V3$, $V4$ and $V5$ are the voltages generated by the diode segments $D2$, $D3$, $D4$ and $D5$.

$$\begin{cases} SUM = (V2 + V4) + (V3 + V5) \\ DIF = (V2 + V4) - (V3 + V5) \end{cases} \rightarrow FES = \frac{DIF}{SUM} \qquad (3.1)$$

The tilting mirror is used in a pre-scanning configuration for scanning the sample in the lateral direction (XY). For the axial direction (Z), a linear stage is used for moving the objective along the optical axis, while the focus sensor measures the distance along the optical axis between the actual position and the system focal point. Therefore, the position of the system's focal point along the optical axis can be determined through an analysis of the reflected light and the generated FES, as explained in Chapter 2.4. The linear stage and the tilting mirror have both integrated sensors, so that the mirror angles and the objective position can be directed measured.

The system also features a camera for observing the scanning procedure. Although it is not used for the surface scanning, it assists in the positioning of samples in the working area of the microscope.

Regarding the objective lens, the system allows a fast and simple exchange of objectives so that various optical systems and their performance could be evaluated. Even though the goal of the system is the use of uncompensated optics, experiments using a high-end microscope objective were also carried out. This way, a comparison between high-end and simple optics could be carried out. The used objectives and the observed results are discussed in Chapter 5.

The implemented system is shown in Figure 3.3. It was designed for surface measurements in millimeter range with sub-micrometer resolution. It uses a tilting mirror platform for deflecting the laser beam and a linear stage for the axial shift of the objective. Both stages are commercial products based on piezo actuators and use strain gauge and capacitor sensors for position control, respectively.

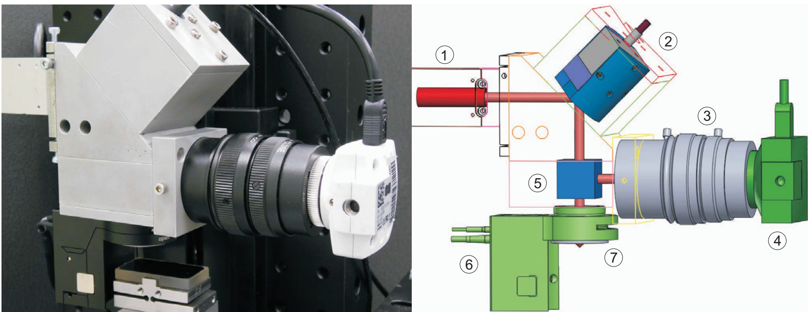

Figure 3.3: Developed laser scanning microscope (1-Hologram Laser Unit; 2-Tilting Mirror; 3-Camera Lens; 4-Camera; 5-Polarized Beam Splitter; 6-Linear Stage; 7-Objective).

The tilting mirror and the linear stage are the main mechanical components. The tilting mirror is based on parallel-kinematics with two coplanar, orthogonal axes and a fixed pivot point. It allows a movement of $\pm 25mrad$ around both axes with a resolution of $5\mu rad$, which e.g. together with a $8.225mm$ focal length objective offers, according to Equation 2.39, a lateral scanning area of approximately $0.8mm \times 0.8mm$ and a step width of approximately $80nm$. The rotation angles are controlled using two voltage signals V_X and V_Y. The linear stage used to move the objective allows a linear movement of $100\mu m$ of the objective with a resolution of $0.7nm$. The position of the stage is controlled using a voltage signal V_Z. Chapter 3.3 and 3.4 explain how

these signals are generated and used to control the scanning procedure and Table 3.1 shows a brief summary of the system's components and their main specifications.

Table 3.1: Specification of the system's components.

Tilting Mirror	
Range	$\pm 25mrad$
Resolution	$5\mu rad$
Repeatability	$5\mu rad$
Resonant Frequency	$1KHz$

Linear Stage	
Range	$100\mu m$
Resolution	$0.7nm$
Repeatability	$\pm 5nm$
Resonant Frequency (unloaded)	$580Hz$

Hologram Laser Unit	
Optical Power	$5mW$
Wavelength	$654nm$
Response Frequency	$40MHz$

Camera	
Sensor Type	CMOS $1/2''$
Pixels	2560×1920
Pixel Size	$2.2 \times 2.2\mu m$

Collimation/Sensor Lens	
Focal Length	$22mm$
Clear Aperture	$\varnothing 4.8mm$
Numerical Aperture	0.11
Details on Table 5.1	

Camera Lenses	
Focal Length	$50mm$
Aperture Value	$12.5mm - 2.7mm$

3.2 Telecentricity

Telecentricity is an important property of optical systems that needs to be considered in the design of scanning microscopes based on auto-focus detection. Telecentricity describes a special condition on optical systems when the light chief rays across the whole object and/or image space are parallel [Haf94, NS92]. In order to achieve telecentricity, the position of the entrance and exit pupils of the system must be properly located. Depending on the position of the pupils, and consequently on the position of the system aperture stop, the system can be telecentric on the object space, on the image space or on both.

Considering the developed microscope shown in Figure 3.1, the system stop and its telecentricity are given by the tilting mirror. If the mirror is located in the back focal plane of the objective lens, the exit pupil will be situated at infinity. The system will then be telecentric on the image space (Figure 3.4a), that is, the chief ray of the incident light on the probe for different mirror angles will always be parallel to one another.

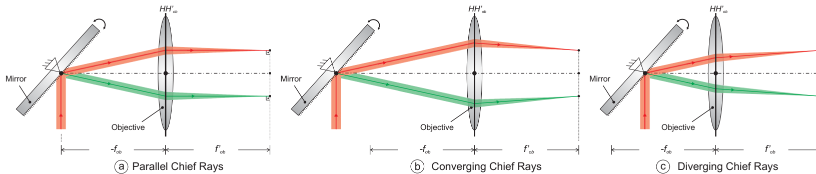

Figure 3.4: Telecentricity in the scanning system.

If the system aperture stop is not in the back focal plane of the objective lens, two important points arise. First, the angle between the light chief ray and the optical axis will change depending on the tilting angle of the mirror, what, as will be shown in Chapter 4.3.1, has a direct influence on the S-Curve of the focus error signal. The second point that arises from the non-telecentricity of the system is illustrated in Figure 3.4b and c. Due to the angle between the optical axis and the chief ray, if the projected laser spot does not lie on the focal plane of the objective, its lateral position will also depend on the defocus of the system and on the position of the objective.

Figure 3.5 illustrates the effect of a defocus in the system with and

without telecentricity on the image space. If telecentricity is present (Figure 3.5a), a defocus of the sample will occur in a larger spot size (circle of confusion), but the position of the center of the spot will not change. The imaging of the light spot will correspond to a parallel projection. If the mirror is not properly positioned (Figure 3.5b), no telecentricity will be present. In this case, a defocus of the sample will change the size and position of the projected laser spot.

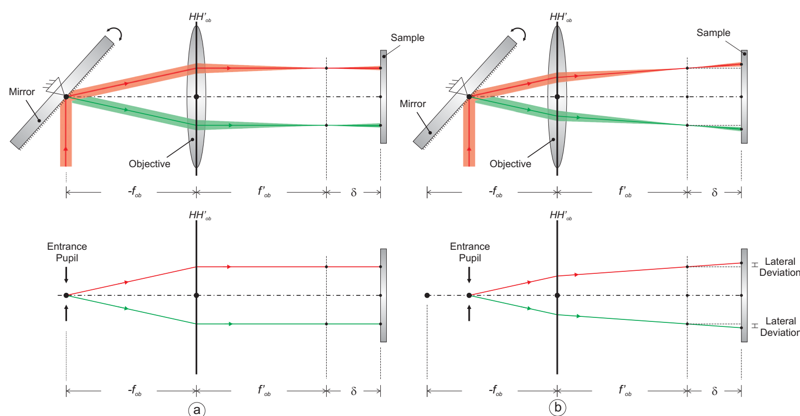

Figure 3.5: Telecentricity on the image space and system defocus.

Therefore, a defocus of the probe causes a lateral deviation of the light spot and can lead to measurement errors. In order to avoid such errors and keep axial and lateral scanning independent from one another, telecentricity on the image space is a necessary feature. It is important especially for the continuous scanning procedure shown in Chapter 3.3, where the sample is not always in focus during measurement.

3.3 Scanning Procedure

The scanning procedure can be divided in two main parts: Axial and lateral scanning. The axial scanning is done using the focus sensor as a zero-sensor. That is, the distance between the sample and the focal plane of the objective is changed until the focus error signal (FES) is

zero and, therefore, the laser spot is exactly focused on the surface. The movement of the objective is measured using the sensors of the linear stage. The tilting mirror is responsible for the lateral scanning, moving the laser spot through the working area.

Two different types of scanning procedures were implemented: a stepwise and a continuous scanning mode. Figure 3.6a shows the typical behaviour of the system during the stepwise scanning procedure for a measurement of 5 × 5 points during the scanning of a sample. The signals V_X and V_Y are used to control the mirror position, moving the laser spot in the lateral direction. The signal V_Z is responsible for controlling the linear stage, moving the objective along the optical axis and changing the distance between the focal plane and the sample. Finally, the FES is used as an error signal for generating the control signal V_Z.

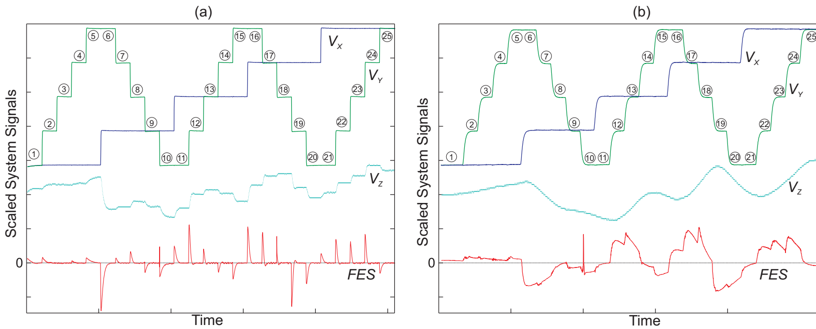

Figure 3.6: Typical signals during the stepwise and continuous scanning procedure.

In each step (1-25), one single point of the sample is measured. First the rotating mirror is positioned and held at a standstill. Then, using the FES as an error signal, the linear stage is used to move the objective along the optical axis until a zero-crossing is detected. Once the zero-crossing is detected the actual position of the system (θ_x, θ_y, Δ_z) is recorded and the measurement of the next point started. The entire process is repeated until all points are measured.

The second implemented scanning procedure is the continuous scanning. The mirror is constantly moved while the FES is used to constantly move the objective and keep it as near from the zero as the res-

onant frequency of the linear stage allows. The data acquisition is performed without waiting for a zero-crossing as shown in Figure 3.6b. In the continuous scanning, due to the intrinsic inertia of the system and the response frequency of the linear stage ($100Hz$), it is not possible to constantly keep the FES exactly at zero, so that the real position of the scanned sample point will be given by the values of Δ_z and FES. Using the characteristic curve of the system (Figure 2.13), as long as the FES is kept small and within its linear region, it is possible to obtain the defocus distance directly and add it to the value of Δ_z, therefore obtaining the Z position of the sample.

Each scanning method has advantages and disadvantages when compared with one another. The stepwise method offers a more precise measurement, independent from the characteristic curve of the system. On the other side, the continuous scanning offers a much faster measurement as illustrated in Table 3.2.

Table 3.2: Average measurement frequency of the scanning methods.

Scanning Modus	Average Frequency
Stepwise	$30Hz$
Continuous	$400Hz$

The hologram laser unit is capable of measurement frequencies up to $40MHz$, but the measurement speed of the system is limited by the resonant frequency of its mechanical components and of the data acquisition. The linear stage ($100Hz$) is the main limiting factor for the stepwise scanning and, for the continuous scanning, the tilting mirror ($1KHz$).

The continuous scanning is highly dependent on the chararacteristic curve of the FES and, as will be shown in Chapters 4.3.1 and 5.1, this curve varies depending on the inclination of the sample. Eventhough these changes do not affect the zero-crossing of the curve, they alter the slope of its linear region, directly affecting the continuous scanning method. Regardless of this disavantage, the continuous scanning offers a substantial gain in the measurement frequency (Table 3.2) and, as long as the defocus is kept small, the error caused by eventual variations of the sample inclination can also be kept within defined boundaries.

3.4 Control and Data Acquisition

For controlling the developed scanning system it is necessary to generate all the signals described in Chapter 3.3 and, at the same time, to acquire all the sensors outputs. The complete system (Figure 3.7) is composed by 3 control signals and 5 sensor signals. The three controls signals (V_X, V_Y, V_Z) are used for tilting the scanning mirror and for positioning the objective while the 5 sensor signals (θ_x, θ_y, Δ_z, DIF, SUM) are used for measuring the actual angle of the mirror, the position of the objective and the focus error.

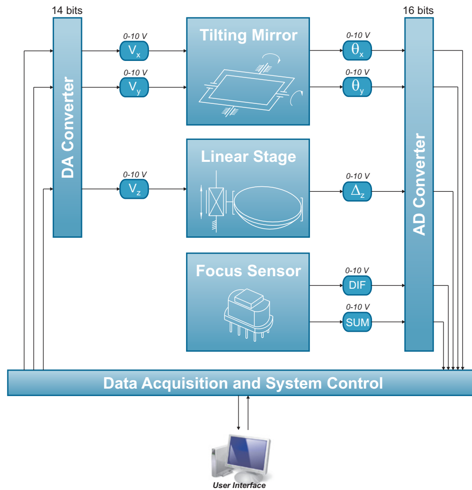

Figure 3.7: System control signals and data acquisition.

The used tilting mirror and linear stage are based on piezo actuators and their resolution is not limited by friction or stick-slip effects. The resolution values shown in Table 3.1 are defined by the electronic noise generated by the driving circuits of the piezos. Nevertheless, due to the use of external analog-digital and digital-analog converters with a resolution inferior to this noise, the limiting parameter becomes the resolution of the AD/DA converters. Even though the tilting mirror and the linear stage offer a much higher resolution, due to the used DA converter with a resolution of 14 bits and a voltage span of $\pm 10V$, the achieved positioning resolution is approximately $6\mu rad$ and $12nm$.

The used AD converter has a slightly better resolution of 16 bits and both of them have a maximal acquisition frequency of $10KHz$. Table 3.3 shows the resolution limits imposed by the AD/DA converters.

Table 3.3: Resolution limits of the used AD/DA converters.

Variable	Positioning Resolution (14 bits)	Measuring Resolution (16 bits)	Voltage Span
θ_x	$6\mu rad$	$1.5\mu rad$	$\pm 10V$
θ_y	$6\mu rad$	$1.5\mu rad$	$\pm 10V$
Δ_z	$12nm$	$3nm$	$\pm 10V$
DIF	–	$0.3mV$	$\pm 10V$
SUM	–	$0.3mV$	$\pm 10V$

Chapter 4

Modelling, Simulation and Calibration

The use of simple uncompensated lenses has always been avoided in scanning microscopy, as it inserts optical aberrations in the system, generates asymmetries in the focus error signal and deteriorates overall performance. The traditional way of solving this problem, as mentioned in previous chapters, is to improve the optical system such that it works as a near-perfect lens, but that comes with the price of large, heavy and costly optics with shorter working distances.

Thanks to advances made in modern computing power, it is now possible to consider unconventional alternatives to optics optimization. The developed scanning microscope presented in Chapter 3 aims at the development of a simple and versatile system with the use of sub-optimal optics. Laser scanning microscopy is a technique that acquires data from the surface point to point, so that the measurement errors caused by optical aberration at each measuring point can be predicted or measured. With previous knowledge of the occurring errors, it is then possible to correct these errors computationally. This allows the use of simpler optics in scanning systems, reducing overall size and weight, raising system dynamics and reducing costs, without significant losses in accuracy. The use of simpler optics also facilitates the integration of scanning devices in different applications. With smaller sizes and longer working distances, scanning devices can be further miniaturized and easily integrated in different systems, allowing their use in applications such as parallel scanning, collision detection of cantilevers and sensor fusion.

Nevertheless, it is important to note that the use of computer correction strategies without any optical compensation also bring drawbacks to the system. The achievable lateral resolution of the optical system as well as the system's sensitivity will be inferior in comparison with a fully compensated system. Nevertheless, these issues do not render the use of simple optics and computer based corrections unviable. The combination of traditional optics optimization with computer based correction offer more flexibility for the optical design and the task of error handling can be divided between optical compensation and computational correction.

In this chapter the complete modelling of the system is presented together with a detailed description of the error correction strategies implemented.

4.1 Correction vs Compensation

Before describing the error correction strategies used, it is important to properly define the use of the technical terms "compensation" and "correction". These terms are often incorrectly used in the literature as interchangeable and are therefore more precisely defined in this section.

According to the Oxford dictionary, compensation can be defined as something that counterbalances or makes up for an undesirable or unwelcome state of affairs, while correction is a quantity adjusting a numerical result to allow for a departure from standard conditions. Although both definitions may sound similar, they present a conceptual difference. Compensation acts on an existing error, or undesired effect, continuously working against the error itself, while correction acts on the obtained results, trying to adjust them to remove the influence of the errors through calculation.

In the scope of optical systems, compensation can be defined as hardware modifications such as changes of lens curvature, the addition of an optical filter or aperture or the adjustment of system alignment. That means compensation alters the signals captured by the used sensors (photodiodes, CCD Matrices, etc.). On the other side, correction uses the measured data signals and manipulates them in order to re-

move undesired effects. Low-pass filters to remove fast oscillations from a photodiode signal or the use of digital filters on an image are common correction examples.

Since the advent of digital signal processing, correction is often associated with software solutions for measurement improvement and error removal, while compensation is mostly associated with hardware improvements or adjustments.

Although system compensation is always possible, it is always associated with high technical and economical costs [Sch82]. System correction, on the other hand, offers more flexibility and makes it possible to extract the maximum performance of a given system. The best way to act against errors in a system is to find a trade-off between correction and compensation.

4.2 Error Correction in Scanning Systems

The idea behind error correction in scanning systems is to determine and predict the influence of the errors caused by the use of uncompensated optics. Optical aberrations in uncompensated optics are systematic and as long as they can be described, they can be corrected. There are two main methods to achieve this: the use of mathematical models to describe the system behaviour, or the experimental measurement of the system's behaviour. A combination of both methods is also a possibility.

In both methods, it is essential to understand the basic functionality of the system as described in Chapter 3. The developed scanning microscope uses sensors to directly measure the inclination angles (θ_x, θ_y) of the moving mirror and the displacement (Δ_z) of the objective. Another important information acquired by the scanning system is that these measured values represent a point $[P_x P_y P_z]$ on the measured sample in which the focus sensor has a null difference signal. The task of the scanning system is now to determine the point $[P_x P_y P_z]$ based on this information.

The scanning system encloses mechanical and optical parameters. The optical parameters define the optical surfaces and components, while

the mechanical parameters define the relative position of those components through kinematic transformations (rotations and translations). Knowing where each component is located and their optical characteristics, each triplet $[\theta_x \theta_y \Delta_z]$ fully describes a state of the system and defines a unique point $[P_x P_y P_z]$ in the measuring volume where the difference signal of the focus sensor is zero. Figure 4.1 shows the basic flow of information for the reconstruction of a sample's surface.

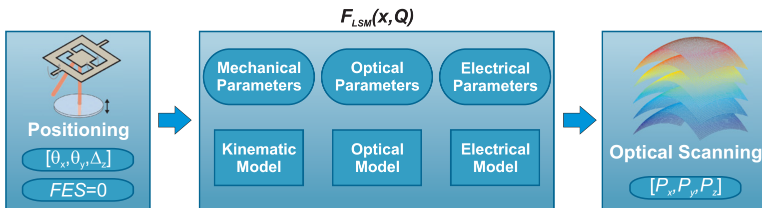

Figure 4.1: Surface reconstruction using error correction.

This way, the LSM can be seen as a mathematical function $F_{LSM}(x, Q)$ that relates kinematic and optical parameters (Q) to 3D coordinates of the system's measuring point. The definition of the function F_{LSM} and the calibration of its parameters are the basis of the model based error correction and are discussed in detail in Chapter 4.3.

Sometimes, due to the complexity of a system, it may be preferable to determine the function F_{LSM} experimentally, so that the mathematical modelling of the system and the definition and calibration of its parameters is no longer necessary. This approach is discussed in detail in Chapter 4.4.

The third possibility to characterize a system is to combine modelling and experimental measurements. This can be implemented, for example, through the calibration of a mathematical model using the measurement results of a known artifact, or the direct measurement of the model's parameters or through the use of a simplified model and the measurement of the deviations between the model and the real system, so that the measured deviations can be used to correct the results obtained with the simplified model.

4.3 Model Based Error Correction

According to IEEE [IEE90], a model can be defined as an approximation, representation, or idealization of selected aspects of the structure, behaviour, operation, or other characteristics of a real-world process, concept, or system. More specifically in the field of measurement systems, a model can be defined, as a mathematical relation between all the parameters and variables involved in the evaluation of a measurement [DIN99]. In other words, a model is a mathematical abstraction that represents the relevant aspects of a real system and, in order to model the developed laser scanning microscope, all the involved elements must be described. In this way the function $F_{LSM}(x, Q)$ encloses the modelling of mechanical, optical and electronic components. The mechanical components are represented by the rotating mirror, the linear stage and all the mounting elements, the optics by all the involved mirrors, lenses and apertures, and the electronics by the photodiodes used to detect the light and generate the focus error signal (FES).

While the mechanical components define the position of every component, the electronics are responsible for the conversion of the light intensity in the sensor into an electrical signal. The optics are the key elements of the scanning system and their modelling the core of the model based definition of the function $F_{LSM}(x, Q)$ presented in this chapter. In Chapter 2.1, different models to describe the behaviour of light were discussed, and two of them are of particularly interest. Due to the complexity of the wave model, the paraxial and the geometric models are in praxis the most convenient ones.

Using the paraxial model, the complete scanning system can be easily described, but, as discussed in earlier chapters, many of the paraxial assumptions are not fulfilled in a scanning system and the model does not represent the true behaviour of the optical system. Nevertheless the paraxial model can still be used as a reference model, and, with the use of highly compensated optical elements, it can still describe a scanning system with high precision.

The geometric model offers a much more precise description of the scanning system, but brings with it a higher complexity than the paraxial model. It is, as explained in Chapter 2.1.3, often used together with ray-tracing. Ray-tracing is a widely used and established technique

for the simulation of optical systems using the geometric model of light, but is often associated with high computer processing demands. However, with the constant advances in graphic computation and the constantly increasing processing power from graphic (GPU) and central (CPU) processing units, the interactive use of ray-tracing is today a reality [Pac08, PBMH02].

Chapter 4.3.1 and Chapter 4.3.2 present the complete derivation of the paraxial model of the developed LSM and also its geometric model using ray-tracing. As optical aberrations are defined as the difference between the paraxial and the geometric models, the comparison of both LSM models makes it possible to evaluate the influence of those aberrations in the measurements. Figure 4.2 illustrates the basic concepts of real system, paraxial and ray model and optical aberrations in the scope of LSM modelling.

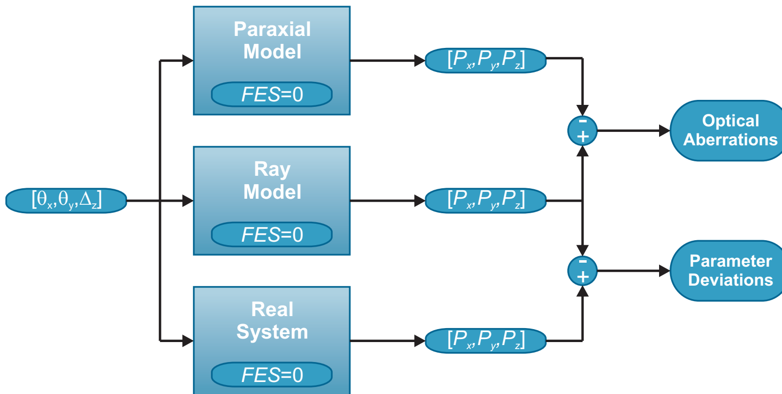

Figure 4.2: Basic concepts of model based error correction.

4.3.1 Paraxial Model

Paraxial optics, also known as Gaussian optics, are the simplest way of describing optical systems [Haf94]. As explained in Chapter 2.1.2, it is a valuable method for determining the first-order properties of a system, assuming that all ray angles are small and in the vicinity of the optical axis. It offers an easy and fast framework in which optical characteristics of a system can be observed and analyzed. Figure 4.3 shows a simplified 2D schematic of the scanning system and its modelling as a paraxial system.

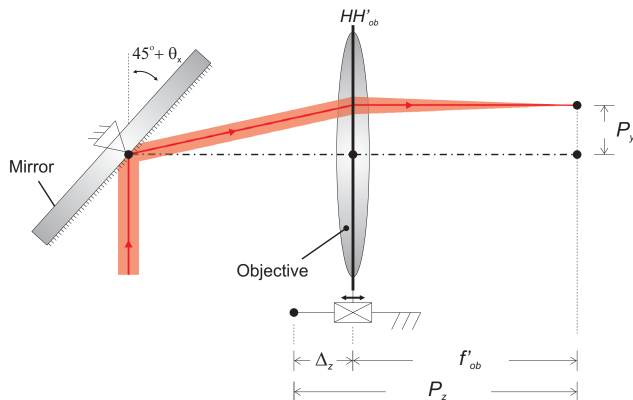

Figure 4.3: Simplified 2D schematic of the scanning system.

Using the framework shown in Figure 4.3, Equation 4.1 defines the position of the focal point of the scanning system. The linear behaviour observed in the Z direction is one of the main reasons why this optical scanning configuration is largely used in laser engraving and confocal laser microscopy [Web96, Mar91, Mar85, GT10].

$$\begin{cases} P_y\left(\theta_x\right) = -f'_{ob}\tan\left(2\theta_x\right) \\ P_z\left(\Delta_z\right) = f'_{ob} + \Delta_z \end{cases} \tag{4.1}$$

The necessary extension of this framework to the 3D space is nevertheless not so direct. In order to shift the focal point freely in the scanning

area, two angles (θ_x,θ_y) and therefore two distinct rotation axes are required. This can be accomplished with the use of two mirrors or with a single mirror capable of tilt in 2 axes. Although the use of two mirrors is still the most usual design, the use of single 2D tilting mirrors started to gain importance, especially due to the recent developments in MEMS. In this work a single mirror was used due to its advantages regarding reduction of elements and compactness for future miniaturization of the system. The mirror has two fixed rotation axes that meet in a single point with a small off-set d_m to the mirror surface. Figure 4.4 shows a schematic of these characteristics which must be considered in the system's modelling.

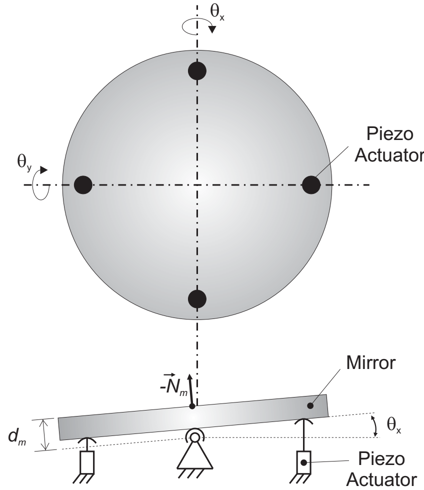

Figure 4.4: Schematic diagram of the used 2D tilting mirror.

The angles θ_x and θ_y are controlled using two piezo actuators per axis (four in total) that work in a push-pull configuration in order to improve the dynamic response of the mirror [Phy03]. Using the schematic diagram in Figure 4.4, the vector $\vec{N}_m$, normal to the mirror's surface, can be defined as:

$$\vec{N}_m = \frac{1}{\sqrt{1+\tan(\theta_x)^2+\tan(\theta_y)^2}} \begin{bmatrix} \tan(\theta_y) \\ -\tan(\theta_x) \\ 1 \end{bmatrix} \tag{4.2}$$

Now, expanding the simplified 2D schematic of the system in Figure 4.3, the 3D paraxial model of the system, illustrated in Figure 4.5, can be derived as shown in Equation 4.3.

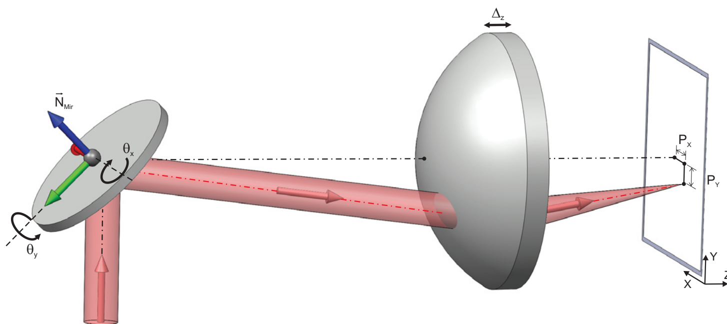

Figure 4.5: Simplified 3D paraxial schematic of the scanning system.

$$\begin{cases} P_x\left(\theta_x,\theta_y\right) = -\frac{\cos(\theta_x)\sin(\theta_y)\sqrt{2}f'_{ob}}{(\cos(\theta_x)-\sin(\theta_x))\cos(\theta_y)} \\ P_y\left(\theta_x,\theta_y\right) = -\frac{\left[\cos(\theta_x)\cos(\theta_y)^2+2sin(\theta_x)cos(\theta_y)^2-cos(\theta_x)\right]\cos(\theta_x)f'_{ob}}{(2\cos(\theta_x)^2-1)cos(\theta_y)^2} \\ P_z\left(\Delta_z\right) = f'_{ob}+\Delta_z \end{cases} \tag{4.3}$$

Equation 4.3 takes into consideration the particular characteristics of the tilting mirror and its orientation at an angle of 45°, so that one of the rotation axes is also tilted in reference to the system's global reference frame. As the objective lens is modelled as a paraxial lens, the linearity of P_z remains unchanged, but Equation 4.3 shows clearly that the positions P_x and P_y of the focal point depend on both angles θ_x and θ_y. Figure 4.6 shows graphically how the position $[P_x, P_y]$ is mapped by the angles $[\theta_x, \theta_y]$ on the focal plane of the objective. The tilting angles were chosen so that the non-linearity of the mapping is visible.

Equation 4.3 and Figure 4.6 show that when using an equally spaced grid of tilting angles (θ_x, θ_y) the resulting positions of the focal point are not equally spaced, and the spatial resolution with which the surface will be sampled will be slightly different for different regions in the working area. In order to avoid this and have a constant spatial resolution over the entire sampled surface, Equation 4.3 can be eas-

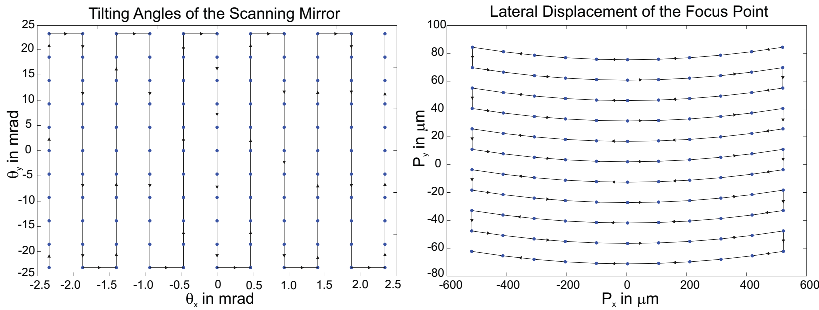

Figure 4.6: Lateral displacement of the focus point in the 3D paraxial model with $f'_{ob} = 15mm$.

ily inverted and the tilting angles necessary for generating an equally spaced grid for the positions $[P_x, P_y]$ calculated.

Once the projection of the laser spot on the sample is known, the next step to complete the modelling of the system is to evaluate the return signal and the generated FES. The developed scanning system, as shown in Chapter 3, uses a variation of the obscuration method and therefore, the following modelling will be done regarding this method.

The obscuration method described in Chapter 2.4.2 uses a knife-edge aperture to block part of the returning light and generate the S-Curve for the FES detection. Chapter 2.4.2 shows the modelling of this method for the collinear case. Nevertheless, due to the use of the tilting mirror and the possibility of measuring inclined probes, the collinearity is not guaranteed in a scanning system. Figure 4.7 illustrates different cases that may arise during the focus detection and show some important details about the generation of the FES in a non-collinear system.

Two main points arise from the introduction of the tilting mirror in the system. The first one is the position of the mirror in reference to the objective lens. In order to achieve telecentricity in the image space, the mirror must be placed in the back focal plane of the objective lens. This way the chief rays of the system will always be parallel to the optical axis as shown in Figure 4.7a and the system will behave exactly as the collinear system described in Chapter 2.4.2. However, if the mirror, due to e.g. mechanical constraints, can not be positioned at the back

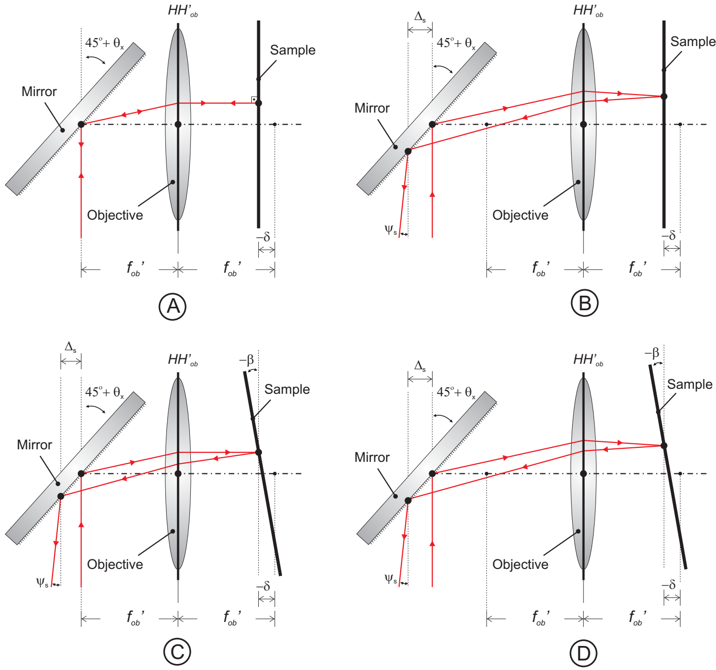

Figure 4.7: Considerations on the non-collinear focus detection in scanning systems.

focal plane of the objective lens and no additional optical elements are used to compensate this effect, no telecentricity will be attained in the image space and for each mirror angle (θ_x, θ_y) the rays projected on the sample will have a different incident angle. Therefore, as illustrated in Figure 4.7b, the returning rays will not follow the same path as the incoming rays and the light beam returning to the sensor will present a displacement Δ_s and an angle ψ_s.

The second point illustrated in Figure 4.7c and 4.7d is the probe inclination β. If the probe is inclined in reference to the optical axis, the light beam returning to the sensor will also present a displacement Δ_s and an angle ψ_s, independent of the telecentricity of the system. This issue also arises in the collinear system (Figure 2.18), where an inclina-

tion of the sample also causes a parallel displacement Δ_s and an angle ψ_s of the returning rays.

Figure 4.8 shows the complete optical schema of the system in 2D for a better comprehension and the new parameters introduced in the obscuration detection method by the tilting mirror and the probe inclination.

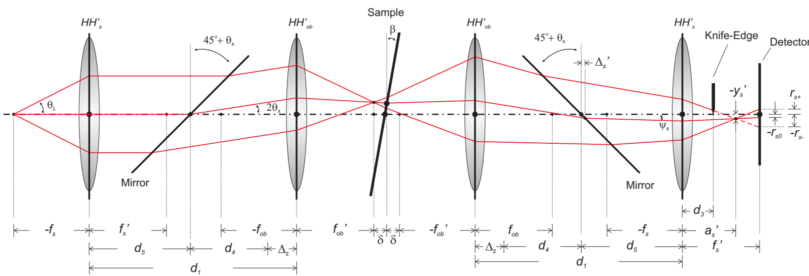

Figure 4.8: Complete 2D optical schema of the focus detection for the scanning system.

Figure 4.8 also introduces the displacement Δ_z of the objective lens in the model. This displacement is used to control the defocus δ of the system so that the FES is always zero (see Chapter 3), but it also changes the distance between the tilting mirror and the lens and therefore the angle of incidence of the light on the sample and must also be taken into account in the model. Using the optical schema shown in Figure 4.8 and following the same method used in Chapter 2.4 the values Δ_s and ψ_s as well as a'_s, y'_s and r_s can be determined. These variables describe the obscuration method in a more generalized way, and, replacing the values of $\Delta_z = 0$ and $\theta_x = 0$, Δ_s and ψ_s are zero and the same equations as those for the collinear method in Chapter 2.4.2 are obtained. They also elucidate a few important points. When the system is in focus the angle ψ_s will be zero and the displacement Δ_s will be a function of the surface inclination and, in the case the system is not telecentric, also of the mirror tilting angle.

In order to determine the generated focus error signal, it is still necessary to define the integration boundaries of the laser spot projected on the photodiode. Not only a'_s but also ψ_s and y'_s have an influence on the integration boundaries as shown in Figure 4.9.

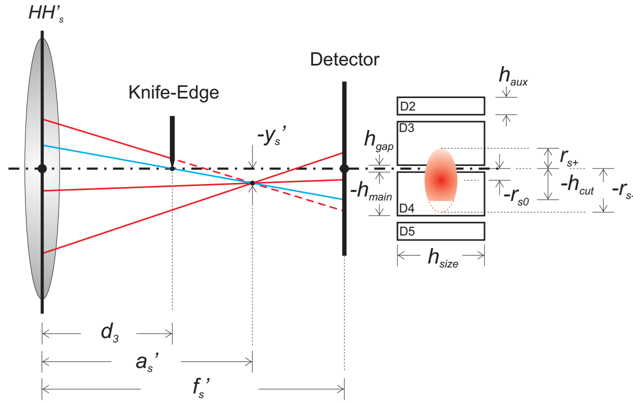

Figure 4.9: Integration boundaries for the non-collinear obscuration method.

Using Figure 4.9, the function $I(x, y, \delta)$ that describes the light intensity distribution on the photodiode can be determined as shown in Equation 4.4 using a 2D Gaussian distribution centred on $(x_0, y_0) = (0, r_{s0})$ and with standard deviation $r_s = \frac{r_{s+} + r_{s-}}{2}$ to approximate the profile of the projected laser spot. Once the intensity function $I(x, y, \delta)$ is known, the voltages $V2$, $V3$, $V4$, $V5$ and the FES can be calculated according to Equations 4.5 and 3.1.

$$I(x,y,\delta) \sim \begin{cases} \frac{1}{r_s^2} \exp\left(-\frac{2}{r_s^2}\left((x-x_0)^2 + (y-y_0)^2\right)\right) & \text{if } y \leq h_{cut}, a_s' > f_s \\ 0 & \text{if } y > h_{cut}, a_s' > f_s \\ \\ \frac{1}{r_s^2} \exp\left(-\frac{2}{r_s^2}\left((x-x_0)^2 + (y-y_0)^2\right)\right) & \text{if } y \geq h_{cut}, d_3 < a_s' < f_s \\ 0 & \text{if } y < h_{cut}, d_3 < a_s' < f_s \\ \\ \frac{1}{r_s^2} \exp\left(-\frac{2}{r_s^2}\left((x-x_0)^2 + (y-y_0)^2\right)\right) & \text{if } y \leq h_{cut}, a_s' < d_3 \\ 0 & \text{if } y > h_{cut}, a_s' < d_3 \\ \\ \frac{1}{r_s^2} \exp\left(-\frac{2}{r_s^2}\left((x-x_0)^2 + (y-y_0)^2\right)\right) & \text{if } y_s' \leq 0, a_s' = d_3 \\ 0 & \text{if } y_s' > 0, a_s' = d_3 \\ \\ \infty & \text{if } a_s' = f_s, y = h_{cut}, x = 0 \\ 0 & \text{if } a_s' = f_s, \text{ otherwise} \end{cases} \tag{4.4}$$

$$\begin{cases} V_2 \sim \int_{-\frac{1}{2}h_{size}}^{\frac{1}{2}h_{size}} \int_{\frac{3}{2}h_{gap}+h_{main}}^{\frac{3}{2}h_{gap}+h_{main}+h_{aux}} I(x,y,\delta)\partial y \partial x \\ V_3 \sim \int_{-\frac{1}{2}h_{size}}^{\frac{1}{2}h_{size}} \int_{\frac{1}{2}h_{gap}}^{\frac{1}{2}h_{gap}+h_{main}} I(x,y,\delta)\partial y \partial x \\ V_4 \sim \int_{-\frac{1}{2}h_{size}}^{\frac{1}{2}h_{size}} \int_{-\frac{1}{2}h_{gap}-h_{main}}^{-\frac{1}{2}h_{gap}} I(x,y,\delta)\partial y \partial x \\ V_5 \sim \int_{-\frac{1}{2}h_{size}}^{\frac{1}{2}h_{size}} \int_{-\frac{3}{2}h_{gap}-h_{main}-h_{aux}}^{-\frac{3}{2}h_{gap}-h_{main}} I(x,y,\delta)\partial y \partial x \end{cases} \tag{4.5}$$

The most important result that can be extracted from the derived paraxial model is that, in spite of the introduction of the radial and axial scanning in its optical path, the obscuration method still delivers an accurate detection of the focus point. That is, independently of the deterioration inserted in the FES by Δ_s and ψ_s, the system's focal point described in Equation 4.3 can still be accurately detected. Figure 4.10 shows the simulation of the FES using the parameters from Table 4.1 for different surface inclinations β with $\theta_x = 0$ and $\theta_y = 0$.

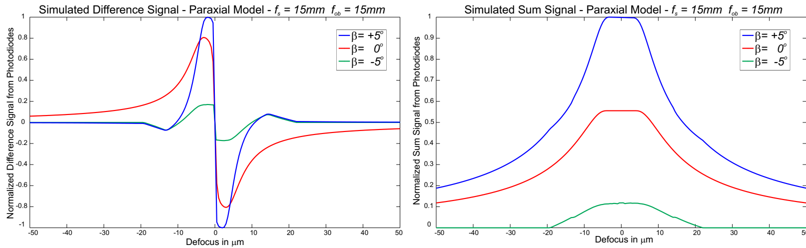

Figure 4.10: Simulation of the FES using the paraxial model.

Table 4.1: Parameters for the paraxial simulation of the FES based on the designed system.

Parameter	Value
f'_s	$22.0mm$
f'_{ob}	$15.0mm$
d_1	$83.3mm$
d_3	$13.5mm$
d_4	$45.8mm$
d_5	$37.5mm$

Figure 4.10 shows, as demonstrated by Hnilicka [HBVS03], Cohen [Coh87] and Mansuripur [MS97], that the obscuration focus detection method, neglecting optical aberration, is only diffraction limited. It also makes clear the influence of Δ_s and ψ_s on the FES. Although the main zero-crossing on the system focus remain unaffected, new zero-crossings occur when the system is not in focus. In order to avoid false focus detections, the defocus of the system must be kept in a very small range. Other observation that can be made using Figure 4.10 is the asymmetry of the FES in relation to the inclination angle of the sample, what can be explained by the presence of the knife-edge. For an angle $\beta < 0°$, the displacement y'_s (see Figure 4.8) is positive and, depending on the magnitude of y'_s a large part of the returning light will be blocked by the knife-edge and, in the extreme case, no signal will be detected by the photodiodes. On the other hand, for an angle $\beta > 0°$, the total light intensity detected on the photodiode will be larger, but, as the difference signal does not grow in the same proportion, the magnitude of the normalized FES will be reduced. The resulting S-Curve is strongly influenced by the geometry of the photodiodes and this same behaviour regarding the occurance of false zero crossings was observed by Mastylo [Mas12] while working with collinear auto-focus sensors.

Though the paraxial model offers a simple and fast way to evaluate an optical system, it applies strictly to light rays that are infinitesimally displaced from the optical axis and does not take optical aberrations into consideration. When working with high precision optical measurement systems, optical aberrations play an important role, and, as scanning systems work with relatively large incident angles, optical aberrations, if not properly addressed, are especially high [GD10, XRJR07, Mar91]. Figure 4.11 illustrates the influence of these optical aberrations in the optical layout shown in Figure 4.5. Using a simple plane-convex spherical lens with a curvature radius of $10.09mm$, a centre thickness of $5.50mm$ and a refractive index of 1.66711 (N-SF5, $\lambda = 650nm$), the focal surface of the system was simulated with the objective at the position $\Delta_z = 0$ using a ray-tracing software tool [GT09].

When compared with the perfect flat focal surface expected from the paraxial model (Equation 4.3), the focal surface shown in Figure 4.11 has a deviation of up to $150\mu m$. The traditional way to solve this problem and obtain a flat field is the development of complex objectives

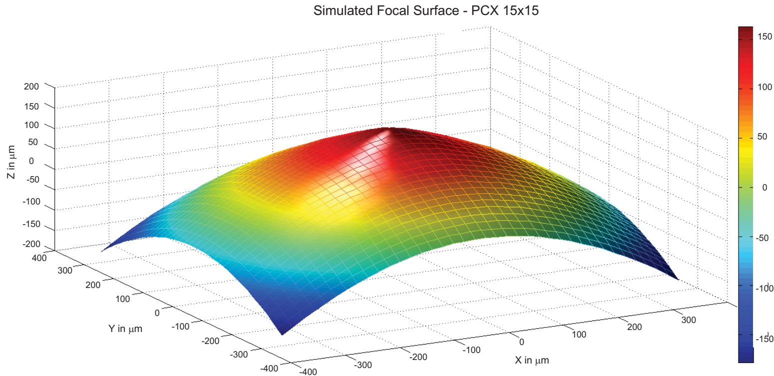

Figure 4.11: Influence of optical aberrations using a simple spherical lens ($f = 15mm$).

that optically compensate these errors and the use of additional optical components to avoid inconvenient conditions such as the under-filling of the objective's entrance pupil [Mar91, Bei95]. As mentioned earlier, this often leads to costly and heavy optics, which reduces system dynamics and makes measuring times larger. Two different alternative solutions to address these errors are proposed in this work. Both of them act not directly on the optical errors, but on their influence on the measurements. The first one is based on a more precise model of the system using ray-tracing and the second one on the measurement of known artifacts to determine the system's function experimentally (Chapter 4.4).

4.3.2 Ray-Tracing Model

Ray-tracing, as explained in Chapter 2.1.3, is a powerful technique for the simulation of optical systems using geometric optics and allows the simulation and evaluation of the optical aberrations in a system. In this chapter the ray-tracing model of the developed scanning microscope is presented and discussed. Figure 4.12 shows a schematic of the scanning system represented as a sequence of mathematical entities that are used for describing each of the mechanical and optical components.

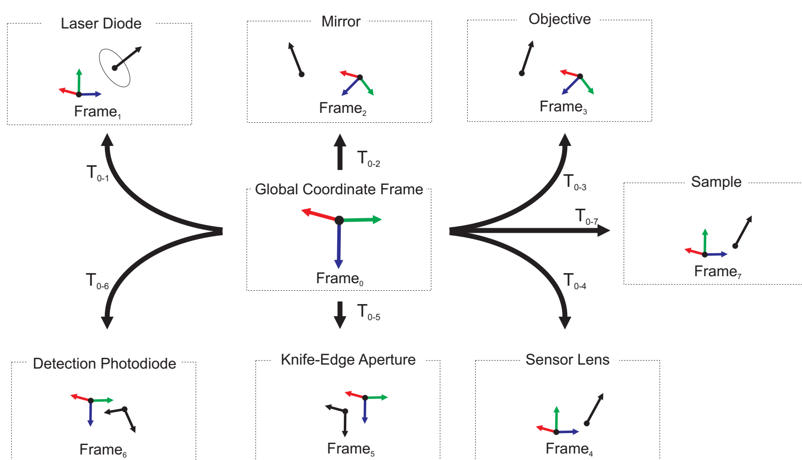

Figure 4.12: Mathematical representation of the scanning system for ray-tracing modelling.

Each one of the system's main components (laser diode, sensor lens, tilting mirror, objective, knife-edge, photodiode) is described in Figure 4.12 within an associated coordinate frame and each one of these coordinate frames is related to the global coordinate frame through a homogeneous transformation defined by Equation 2.9. The initial rays of the system are generated by the laser diode. The diode is mathematically represented by a point O_L that defines its origin, a vector N_L that defines its propagation direction and an aperture angle θ_L. With these parameters any desired number of rays can be generated to represent the laser beam. The generated rays are symmetrically distributed in-

side the circular aperture defined by O_L, N_L and θ_L. The tilting mirror is described by its rotation point P_m, its normal vector N_m and its surface off-set d_m (see Figure 4.4). The normal N_m is controlled by the two tilting angles θ_x and θ_y around the X and Y axes of the mirror coordinate frame and is given by Equation 4.2. The geometry of the objective lens is defined by its origin O_{ob}, its normal vector N_{ob}, its centre thickness d_{ob} and by the coefficients of its surfaces. These coefficients are defined through the even asphere equation (Equation 2.7) and are normally provided by the lens manufacturer. In order to fully describe the lens, it is still necessary to know its refraction index. As the developed system works with a single wavelength of approximately $650nm$, and the lenses materials are known, the refraction index can be obtained directly from a material's database [Pol].

The focus sensor, based on the obscuration method (Chapter 2.4.2), encloses not only the laser diode described above but also the three remaining components: the sensor lens, the knife-edge aperture and the detector photodiode. The sensor lens is used both for collimating the laser diode and for focusing the returning laser beam into the photodiode through the knife-edge. Similarly to the objective lens, it is defined by its origin O_{se}, its normal vector N_{se}, its centre thickness d_{se} and its surface's coefficients. The knife-edge and the photodiode are defined by their origin O_{ke} and O_{pd} , their normal vectors N_{ke} and N_{pd} and by an additional vector D_{ke} and D_{pd}. The vectors D_{ke} and D_{pd} define, respectively, the direction of the knife-edge and of the gap between the photo detectors as illustrated in Figure 4.13.

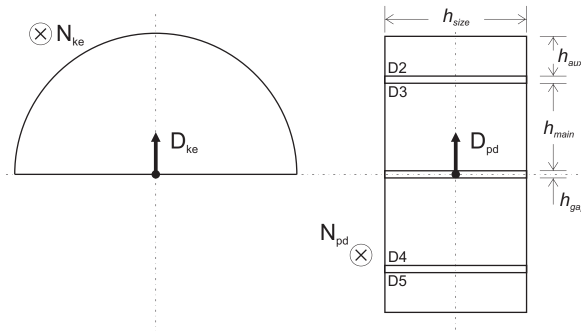

Figure 4.13: Definition of the direction vectors D_{ke} and D_{pd}.

The last component illustrated in Figure 4.12 is the measured sample. In order to simulate the *FES* it is necessary to describe the light collected by the scanning system after its interaction with the sample's surface. For this purpose the sample surface is modelled as a perfect plane mirror defined by its origin O_{sp} and its normal vector N_{sp}. This same approximation was also used for the derivation of the paraxial system.

Using this framework and the ray-tracing method described in Chapter 2.1.3, the complete system can be mathematically represented as shown in Table 4.2, Table 4.3 and Figure 4.14. Table 4.2 shows the definition of the origin and normal vectors of each component and Table 4.3 of the homogeneous transformations (T_{0-1} to T_{0-7}) associated with each one of the coordinate frames illustrated in Figure 4.12. For convenience and without loss of generality, the origin and normal vectors of the components are chosen, accordingly to Table 4.2, to coincide with their corresponding coordinate frames.

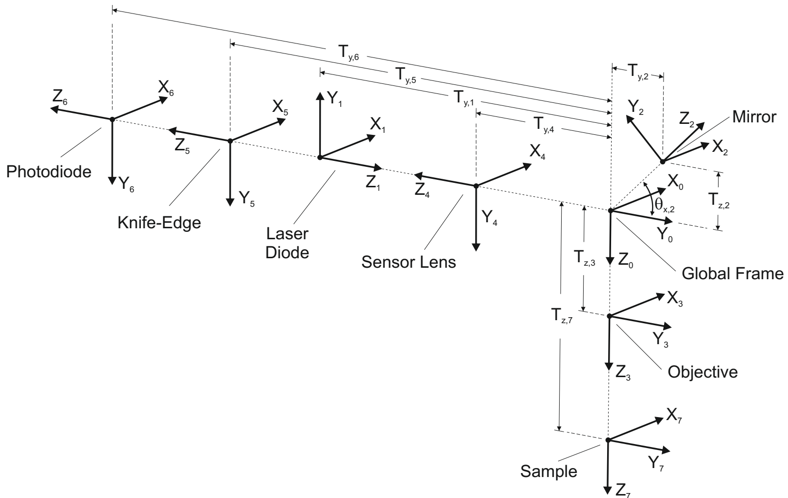

Figure 4.14: Representation of the kinematic chain of the ray-tracing model.

Table 4.2: Origin and normal vectors of the ray-tracing components.

Laser Diode	
Parameter	Value
O_L	$[0,0,0]$
N_L	$[0,0,1]$
θ_L	6°

Mirror	
Parameter	Value
P_m	$[0,0,0]$
N_m	Equation 4.2
d_m	$4mm$

Knife-Edge	
Parameter	Value
O_{ke}	$[0,0,0]$
N_{ke}	$[0,0,1]$
D_{ke}	$[0,1,0]$

Sample	
Parameter	Value
O_{sa}	$[0,0,0]$
N_{sa}	$[0,0,1]$

Objective Lens	
Parameter	Value
O_{ob}	$[0,0,0]$
N_{ob}	$[0,0,1]$

Sensor Lens	
Parameter	Value
O_{se}	$[0,0,0]$
N_{se}	$[0,0,1]$

Photodiode	
Parameter	Value
O_{pd}	$[0,0,0]$
N_{pd}	$[0,0,1]$
D_{pd}	$[0,1,0]$
h_{gap}	$0.0mm$
h_{main}	$1.0mm$
h_{aux}	$0.6mm$

Table 4.3: Homogeneous transformations of the ray-tracing model.

Laser Diode (T_{0-1})	
Parameter	Value
$T_{x,1}$	$0mm$
$T_{y,1}$	$-72.0mm$
$T_{z,1}$	$0mm$
$R_{x,1}$	-90°
$R_{y,1}$	0°
$R_{z,1}$	0°

Mirror (T_{0-2})	
Parameter	Value
$T_{x,2}$	$0mm$
$T_{y,2}$	$2.83mm$
$T_{z,2}$	$-2.83mm$
$R_{x,2}$	-135°
$R_{y,2}$	0°
$R_{z,2}$	0°

Objective Lens (T_{0-3})	
Parameter	Value
$T_{x,3}$	$0mm$
$T_{y,3}$	$0mm$
$T_{z,3}$	$45.0mm + \Delta_z$
$R_{x,3}$	0°
$R_{y,3}$	0°
$R_{z,3}$	0°

Sensor Lens (T_{0-4})	
Parameter	Value
$T_{x,4}$	$0mm$
$T_{y,4}$	$-50.0mm$
$T_{z,4}$	$0mm$
$R_{x,4}$	90°
$R_{y,4}$	0°
$R_{z,4}$	0°

Knife-Edge (T_{0-5})	
Parameter	Value
$T_{x,5}$	$0mm$
$T_{y,5}$	$-70.0mm$
$T_{z,5}$	$0mm$
$R_{x,5}$	90°
$R_{y,5}$	0°
$R_{z,5}$	0°

Photodiode (T_{0-6})	
Parameter	Value
$T_{x,6}$	$0mm$
$T_{y,6}$	$-72.0mm$
$T_{z,6}$	$0mm$
$R_{x,6}$	0°
$R_{y,6}$	0°
$R_{z,6}$	0°

Sample (T_{0-7})	
Parameter	Value
$T_{x,7}$	$0mm$
$T_{y,7}$	$0mm$
$T_{z,7}$	$0mm$
$R_{x,7}$	0°
$R_{y,7}$	0°
$R_{z,7}$	0°

Table 4.2 and Table 4.3 include the three system variables (θ_x, θ_y, Δ_z) and a series of constructive parameters, which are also illustrated in Figure 4.14 together with the coordinate frames resulting from the homogeneous transformations T_{0-1} to T_{0-7}.

Using these parameters, the system can then be simulated using the ray-tracing model. Figure 4.15 shows the simulation of the *FES* obtained using the parameters illustrated in Tables 4.2 and 4.3 for the system in its null position ($\theta_x = 0$, $\theta_y = 0$, $\Delta_z = 0$).

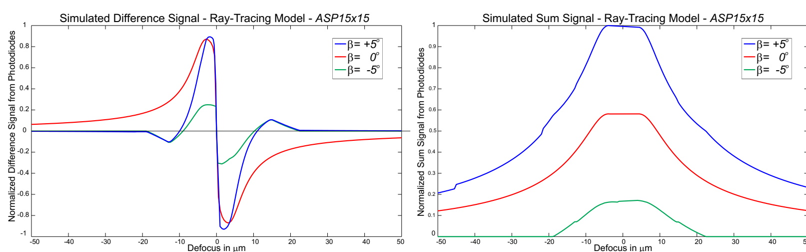

Figure 4.15: Simulation of the focus error signal *FES* using the ray-tracing model.

For this simulation, two aspheric lenses were used. The sensor lenses were simulated using the ASP6×22 lens, and the ASP15×15 was used as objective. Both lenses are designed, respectively, for laser collimating and focusing and are defined by the parameters shown in Table 5.1. Figure 4.15 shows the simulated S-Curves. As the scanning system is in its null position (coaxial situation), the aspherical lenses work on its optical axis and compensate for the optical aberrations of the system so that the obtained characteristic curve shows a behaviour very similar to that of the paraxial system (Figure 4.10). In the case of uncompensated spherical lenses, the influence of the optical aberrations in the characteristic curve is stronger as the slope of the linear region of the curve and therefore the sensitivity of the focus detection decreases. Figure 4.16 shows the characteristic curve of the system using the ASP6×22 lens as sensor lens and, as objective, a paraxial lens, the ASP15×15 and the PCX15×15 lenses.

The optical aberrations and the diffraction of the laser beam are the practical limiting factors for the sensitivity that can be achieved in the focus detection with the obscuration method [HBVS03, MS97, Coh87].

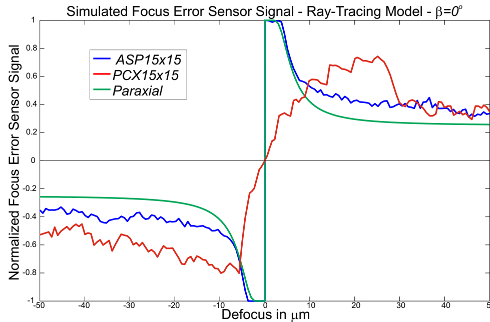

Figure 4.16: Influence of optical aberrations on the *FES* for $\beta = 0°$.

Chapter 5.1 shows a brief experimental analysis of these effects on the implemented scanning system. The influence of optical aberrations on focus detection methods was extensively studied by Cohen [Coh87], Mansuripur [MS97] and Hnilicka [HBVS03].

When simulating a system using a ray-tracing method, it is important to consider its high computational cost. Although alternatives such as real-time data acquisition and offline post-processing can be taken into consideration, ray-tracing is not suited for real-time applications unless it is combined with further improvements and optimizations.

The model presented in this chapter was implemented using two different programming languages. The first variant was developed using the software *MatLab*®, due to its flexibility and the wide option of numerical algorithms available in its libraries. The second variant was developed in *C/C++* in order to achieve a better efficiency and speed.

Although there is still much place for further improvements regarding speed and code efficiency in both implementations, these issues are not in the scope of this work and were not addressed. Ray-tracing optimization is a very broad and active research area [Pac08,PBMH02] following its use in different fields such as illumination and optics simulation, cinema, computer games and many others. There are different methods to accelerate ray calculations described in the literature using both software and hardware solutions [PBMH02]. Chapter 5.10 shows a short comparison between the execution speed of both implemented variations.

4.3.3 Model Calibration

Given the function $F_{LSM}(x, Q)$ of the LSM, obtained through mathematical modelling as shown in the previous chapters, there are two possible sources for discrepancies between the model and the real system. Either the model does not describe the real behaviour of the measuring system accurately enough, or the parameters Q of the function $F_{LSM}(x, Q)$ are not coincident with those of the real system. Model calibration addresses the second issue.

These deviations between the model's parameters and the real system arise mostly due to manufacturing and assembly tolerances and can be approximated through three different methods. The first one is the use of tolerance chains to define the maximum deviation between the design value of a parameter and its real value. The second method is the direct measurement of each parameter after assembling, so that the maximum deviation of each parameter is defined by the uncertainty of the measuring system used. The third and final method is the indirect measurement, or calibration, of the system's parameters using known artifacts or other measuring systems to numerically estimate the values of the parameters. Figure 4.17 shows an example of the application of these concepts. It illustrates a simple system where the voltage V on a resistance R is used to determine the current i in the circuit.

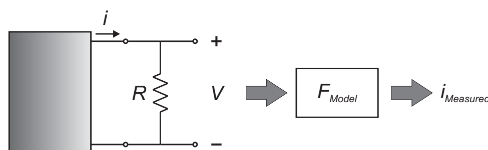

Figure 4.17: Example model for current measurement.

The current i can be determined using a mathematical description of the electrical circuit based on a model function F_{Model} given by Equation 4.6.

$$I_{\text{Measured}} = F_{\text{Model}}(V, R_{\text{Model}}) = \frac{V}{R_{\text{Model}}} \tag{4.6}$$

The mathematical model F_{Model} has the resistance R_{Model} as its single parameter. In order for the model to correctly describe the behaviour of the real system and correctly measure the current (i), the value of R_{Model} must correspond to the real value R of the resistance. However it is not possible to manufacture a resistance with an exact desired value, and the exact real value of the resistance is always unknown, so that R_{Model} and R will differ from one another by an unknown value ξ_R given by Equation 4.7.

$$R = R_{\text{Model}} + \xi_R \tag{4.7}$$

As explained earlier, there are three different ways of approximating the value R, so that the deviation ξ_R and its influence on the measurement are minimized. The first possibility is to use manufacturing tolerances. Manufacturing tolerances define with a large margin of confidence the maximum deviation of a given value, so that, the deviation ξ_R between R and R_{Model} is limited by $\pm\tau_R$ and its influence in the measurement can be calculated using error propagation [Kra00, DIN99, JCG08]. In the specific case of the model shown in Equation 4.6, the resultant error in the measurement of the current i due to manufacturing tolerances is given by the linearization of the function F_{Model} using the first order expansion of the Taylor series as shown in Equation 4.8. Using $\xi_R \leq \tau_R$ the maximal error can then be determined.

$$\xi_i \approx \sqrt{\left(\frac{\partial F_{\text{Model}}(V, R_{\text{Model}})}{\partial R_{\text{Model}}}\xi_R\right)^2} = \left|\frac{V}{R^2_{\text{Model}}}\xi_R\right| \tag{4.8}$$

The second possibility is to use a different system to directly measure the value of R and use the measured value R_{Measured} as a parameter in the model instead of the design value. This way R_{Model} is now given by R_{Measured} and the limiting values $\pm\tau_R$ of ξ_R will be defined by the measurement uncertainty of the device used to measure the resistance. This method normally offers a better estimate of the real parameter's value than the manufacturing tolerances, but is often not a viable alternative due to the number of involved parameters or the impossibility to perform a direct measurement. The final error in the

example function F_{Model} due to the measurement uncertainty will also given by Equation 4.8.

The third and last possibility is the calibration, or indirect measurement, of the system's parameters. It is based on the estimation of the model's parameters, the mathematical process of adapting the model to experimental data. The final parameters are chosen so that the resulting output of the model is as close as possible to the observed data. In order to accomplish the estimation, a known input is applied to the system and its output is measured. With the known input values and the design values of the system's parameters, the model output can also be calculated and the obtained results compared with the measured ones. Assuming the mathematical model describes the real system with enough accuracy, the difference between the values predicted by the model and the actual measured ones can be ascribed to the parameter deviations in the model and used to indirectly determine these deviations and adapt the model.

In the case of the function F_{Model}, applying n different known currents i'_j, n different voltage values V_j will be acquired by the system illustrated in Figure 4.17 and used to calculate the values of i_j according to Equation 4.6. As every measurement has an associated uncertainty, each pair $[i'_j, i_j]$ yields a different optimal value for R_{Model}. For this simple example, the value of R_{Model} that best represents the experimental data and minimizes ξ_R can be directly determined through Equation 4.9 and the limiting values $\pm\tau_R$ directly obtained through the uncertainties $\xi_{i'}$ and $\xi_{V'}$ associated with the independent variables i' and V respectively. The final error in the measurement of the current (i) due to the uncertainty in the calibration of R_{Model} will also be given by Equation 4.8.

$$\begin{cases} R_{\text{Model}} = \frac{1}{n} \sum_{j=1}^{n} \frac{V_j}{i'_j} \\ |\xi_R| \leq \tau_R \approx \sqrt{\left(\frac{\xi_V}{i'}\right)^2 + \left(\frac{-V\xi_{i'}}{i'^2}\right)^2} \end{cases} \tag{4.9}$$

Due to the complexity of many models it is not always possible to obtain a direct equation to define the deviations of a system's parameters as in Equation 4.9. Often the model function itself can not be analytically defined. In such situations numeric approximation and

iterative methods need to be employed in order to obtain a solution. Parameter estimation is often done through the solution of an overdetermined system of non-linear equations and is a problem that arises in many fields of applied sciences and engineering. There is a great variety of methods and algorithms to solve this class of systems and it is a very broad and active field of research. Van den Bos [vdB07], Hermann [Her01] and Kreyszig [Kre06] are good references for general issues regarding parameter estimation and numerical methods, while Ulbrich [UU12] presents a rigorous mathematical approach focused on non-linear problems. Van den Bos [vdB07] and Ulbrich [UU12] also show a deeper insight in the large variety of computational methods and algorithms available.

In the case of the developed LSM, the number of parameters and the complexity of the system and its model F_{LSM} are much larger than in the function F_{Model}, but the basic concept of minimizing the residue of a non-linear system given a set of experimental data is still valid. Given the set of parameters $Q = [\zeta_1, \cdots, \zeta_m]$, the function $F_{LSM}(x, Q)$, using the triplet $x_i = [\theta_{x,i}, \theta_{y,i}, \Delta_{z,i}]$, defines a measurement point P_i, although the real measured point P_i' lies in a different position. The difference $\varepsilon_i = P_i - P_i'$ is the measurement error of the system at the position x_i. Figure 4.18 illustrates this concept graphically.

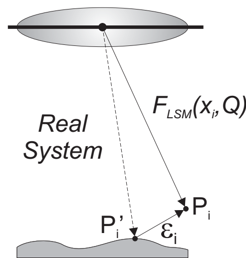

Figure 4.18: Basic calibration concept for the laser scanning microscope.

ε describes the measurement deviations due to errors in the model and occurs, as discussed earlier (Figure 4.2), due to differences between the model's parameters and their values in the real system. It is mathematically defined by Equation 4.10.

$$\begin{bmatrix} \varepsilon_1 \\ \vdots \\ \varepsilon_n \end{bmatrix} = P_i - P_i' = F_{LSM}(x_i, Q) - P_i' \tag{4.10}$$

Given the parameters $Q = [\zeta_1, \cdots, \zeta_m]$, the goal of the calibration is to determine the vector $\delta_Q = [\delta_{\zeta_1}, \cdots, \delta_{\zeta_m}]$ that minimizes the error vector ε shown in Equation 4.10, where m is the total number of parameters in the model and n the number of measurement points. Assuming the function F_{LSM} is differentiable, the displacement ΔP_i of the point P_i caused by an infinitesimal change δ_{ζ_j} when the system is at a position x_i can be approximated by the first order Taylor expansion on Equation 4.11, where J_{LSM} is the Jacobian matrix of F_{LSM} at the position x_i and δ_Q are the changes introduced in the system's parameters.

$$\begin{cases} F_{LSM}(x_i, Q + \delta_Q) \approx F_{LSM}(x_i, Q) + J_{LSM}(x_i, Q)\, \delta_Q \\ \Delta P_i = F_{LSM}(x_i, Q + \delta_Q) - F_{LSM}(x_i, Q) \end{cases}$$
$$\rightarrow \Delta P_i \approx J_{LSM}(x_i, Q)\, \delta_Q \tag{4.11}$$

Equation 4.11 can be interpreted as an error equation of the LSM, where the modifications δ_Q of the model's parameters should be chosen so that the inserted ΔP_i minimize the error ε and the points P_i and P_i' coincide.

$$\begin{cases} F_{LSM}(x_i, Q + \delta_Q) = P_i + \Delta P_i \\ \Delta P_i = -\varepsilon_i \end{cases}$$
$$\rightarrow F_{LSM}(x_i, Q + \delta_Q) = P_i' \tag{4.12}$$

However, the point P_i' and therefore also the error ε_i can not, without great difficulty (Figure 4.20), be directly measured. In order to measure the point P_i' an external measurement device is necessary and its position in reference to the LSM determined. An alternative to the laborious use of an external measurement system is the scanning of a known artifact. The deviations between the measured data and the

known geometry of the artifact can then be used to calibrate the system's parameters. With that purpose, the function F_{LSM} must first be remodelled.

Using the set of parameters Q and a reference surface S described by the parameters $B = [b_1, \cdots, b_k]$ a new function $F'_{LSM}(\theta_x, \theta_y, Q, B)$ can be written to describe the necessary displacement Δ'_z of the objective to scan the surface S (Equation 4.13). This displacement can be directly measured and the difference ε'_i between the measured displacement ($\Delta_{z,i}$) and the one obtained with F'_{LSM} is the model error. This way, Equation 4.11 can be rewritten as shown in Equation 4.14 for different positions $x'_i = [\theta_{x,i}, \theta_{y,i}]$.

$$\Delta'_z = F'_{LSM}(\theta_x, \theta_y, Q, B) \tag{4.13}$$

$$\varepsilon'_i = \Delta_{z,i} - F'_{LSM} = \begin{bmatrix} \frac{\partial F'_{LSM}}{\partial Q} & \frac{\partial F'_{LSM}}{\partial B} \end{bmatrix} \begin{bmatrix} \delta_Q \\ \delta_B \end{bmatrix} \tag{4.14}$$

Using function F'_{LSM}, the error ε'_i in each position x'_i is directly measureable and the calibration problem is reduced to a non-linear minimization problem with the general form $Ax = b$. Even though, as discussed earlier, there is a large variety of methods to solve such minimization problems, in this work only the Levenberg-Marquardt algorithm (LMA) was used. It is a widely used method for the minimization of non-linear equations and systems in the least squares sense [vdB07,UU12] and is a method that proved to be very successful in practice, especially in optical design. The algorithm is an iterative method based on modifications in the Gauss-Newton method to avoid convergence problems and is described in detail in the literature. Experimental and simulation results of the calibration process are shown and discussed in Chapter 5.3.

4.4 Measurement Based Error Correction

The experimental measurement of a system's function is an alternative to complex mathematical models. It offers a fast and direct method to determine the behaviour of a system and avoids the evaluation of mathematical functions that are expensive to compute. The function F_{LSM} can be seen as a black box that, given an input $x = [\theta_x, \theta_y, \Delta_z]$, defines a single point $P = [P_x, P_y, P_z]$ in space. The measurement of a probe using an LSM can be schematized as in Figure 4.19.

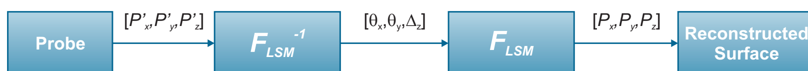

Figure 4.19: Laser scanning microscope as a black box.

This way, by applying different known inputs and measuring the associated outputs, F_{LSM} can be characterized without the need of knowing its internal mechanisms. Nevertheless this approach brings with it some disadvantages. The required experimental setup itself is often extremely laborious and time demanding and, as system's output can only be measured for fixed inputs, the behaviour of the system is measured only in discontinuous points and needs to be interpolated or extrapolated for inputs other then the measured ones. Another disadvantage of this approach is that the effect of modifications in the system can not be predicted, so that eventual improvements can not be planned and, for every change introduced, the experimental measurement must be redone. Regardless of these drawbacks, the experimental measurement of a system is in some cases the only solution when the system's model is unknown.

In the case of the developed LSM, Figure 4.20 shows a conceptual design of the required setup for directly measuring the outputs of the system's function. Using this setup, an input $x = [\theta_x, \theta_y, \Delta_z]$ is applied to the LSM and a position sensing detector (e.g. CCD Matrix, Quadrant-Diode) is moved along the XYZ axes until the FES of the LSM is zero and the laser spot is centred on the detector. The values of $P = [P_x, P_y, P_z]$ can now be obtained by measuring the displacement of the sensing detector.

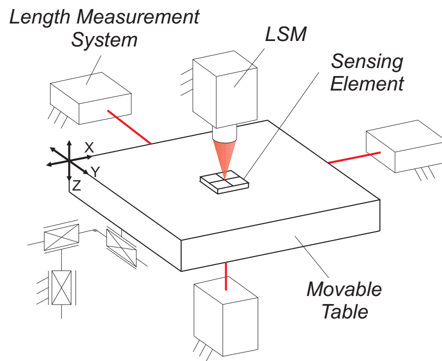

Figure 4.20: Conceptual design for the direct measurement of F_{LSM}.

Although the measurement rig in Figure 4.20 illustrates the basic concept for the direct measurement of the function of the LSM, it is a rather complex setup. In order to facilitate this experimental measurement, an alternative approach was used. The measurement task was divided into two stages. Firstly a flat mirror ($\lambda/20$) was positioned perpendicular to the scanning microscope and moved in the Z direction as shown in Figure 4.21. Choosing a single point in the work area (e.g. $(\theta_x, \theta_y) = (0, 0)$), the position of the mirror in $Z_{0,0}$ can be determined directly from Δ_z and the mirror mathematically described as $Z = Z_{0,0}$. Repeating this process for diferent Z positions, a series of measuring points with the form $(\theta_x, \theta_y, \Delta_z) \rightarrow P_z$ can be acquired.

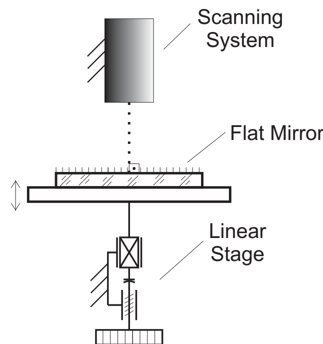

Figure 4.21: Conceptual design for the direct measurement of F_{LSM}.

With P_z experimentally determined, the second step is the measurement of P_x and P_y. One possibility is to repeat the same approach used for measuring Δ_z using a position sensitive device (PSD) or a CCD-Sensor to measure the P_x and P_y coordinates. A second possibility is to use the ray-tracing or the paraxial model to directly calculate these coordinates and only use a measurement based error correction on the Z direction.

In this chapter two approaches to the measurement based error correction are presented. Both are based on the experimental procedures described above, but use different interpolation strategies. The first approach uses look-up tables (LUT) and the second one polynomial functions for describing F_{LSM}.

4.4.1 Look-up Table

Look-up tables (LUT) have been a standard tool in mathematics and engineering since before the advent of computers. They consist of an array or matrix that is used to store pre-determined outputs of a function for different inputs. This way, given any input, the function value can be directly obtained through the LUT and does not need to be computed, replacing the calculation of the function by a simple consulting operation. In the case the input falls between the table's samples, the output can then be approximated with interpolation techniques. Figure 4.22 shows an example of a one dimensional LUT used to represent a sinusoidal function and its reconstruction using linear interpolation.

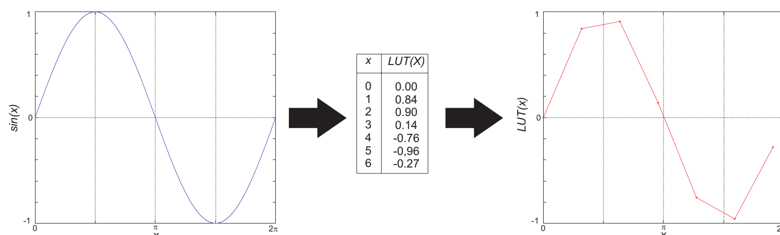

Figure 4.22: 1D Look-up table of a sinusoidal function.

Look-up tables offer a few advantages compared to direct function implementation. As the tables only exist as a logical structure in a digital

memory device, they are extremely flexible and fast. They are a commonly used technique to accelerate numeric processing in applications with strict time requirements, such as digital signal processing (DSP), custom control systems and image processing [FMT99]. Nevertheless, these advantages come with the cost of memory usage. It is necessary to store the LUT and, for high complexity functions, the number of necessary elements to keep interpolation errors small is extremely large.

A very common application for LUTs, especially in the fields of communications, measurements and control, is the implementation of linearizers/characterizers for non-linear systems [FMT99]. In such applications a LUT is used for reducing linearity errors so that the output values of a system are more accurate.

This same concept can be expanded and used in the developed LSM. The function $F_{LSM}(x, Q)$ maps a set of inputs $x = [\theta_x \theta_y \Delta_z]$ to exactly one output $P = [P_x, P_y, P_z]$, so that, applying different values x_i to the system and measuring the point P where the FES is zero (Figure 4.20), the function F_{LSM} can be experimentally determined and represented using three look-up tables, one for each cartesian coordinate $[P_x, P_y, P_z]$. Figure 4.23 shows how the basic concept illustrated in Figure 4.22 can be extended for F_{LSM}.

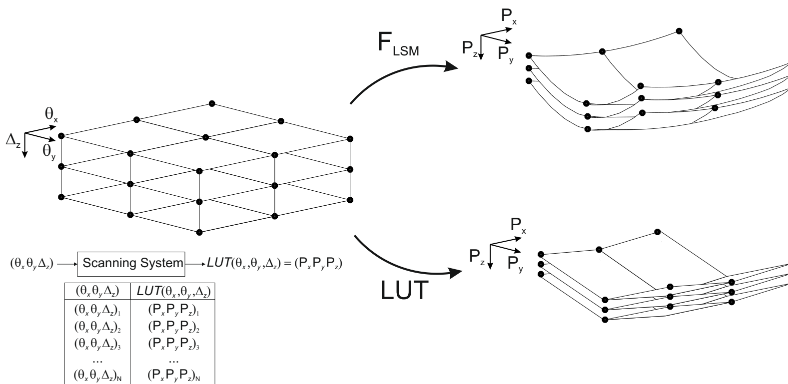

Figure 4.23: Describing F_{LSM} with a look-up table.

Another possibility, to avoid the necessity a complex measurement rig as shown in Figure 4.20, is to use the paraxial or the ray-tracing model for representing the P_x and P_y coordinates and use a single LUT to correct the errors on P_z.

4.4.2 Polynomials

Look-up tables (LUT) are not the only method to approximate multivariate functions. There are numerous methods for approximating such functions and the use of polynomials is one of the most classical ones. Polynomials are a very simple and well known group of mathematical functions. They are extremely easy to evaluate and are therefore widely used in many fields, including the interpolation and approximation of functions. They are well described in the literature and authors such as Phillips [Phi03] and Hermann [Her01] give a thoroughly and comprehensive description of the development of polynomials and the theory behind polynomial approximations and their use in numerical mathematics.

Polynomials are an extremely convenient way of approximating functions. They can not only be easily differentiated and integrated, resulting in another polynomial, but they can also approximate continuous functions with any desired accuracy. The Weierstrass theorem [Her01, Phi03] states that, for any continuous function $F(x)$ on a closed interval $J = [a, b]$, there is a polynomial $p_n(x)$ such that Equation 4.15 is valid for any chosen error $\varepsilon > 0$.

$$|F(x) - p(x)| < \varepsilon, x \in J \tag{4.15}$$

A polynomial can be generally described as shown in Equation 4.16, where $p_n(x)$ is a so called basis function.

$$p(x) = c_0 + c_1 p_1(x) + c_2 p_2(x) + \cdots + c_n p_n(x) \tag{4.16}$$

Many different types of polynomials can be obtained by choosing different basis functions $p_n(x)$. Nevertheless, for convenience, the basis function is often chosen as a polynomial itself [Phi03]. There is a wide variety of polynomials that can be chosen as basis for representing a

polynomial approximation. The Lagrange-Polynomials, the Newton-Polynomials and the Chebyshev-Polynomials are just a few examples. Each one of these basis polynomials have its own characteristics and are well documented in the literature [Phi03,Her01] especially for univariate interpolation.

In the case of multivariate interpolation, although approximation techniques are still not well developed, they are still a powerful mathematical tool. With that in mind and in order to overcome some of the drawbacks of LUTs, a polynomial approach was also implemented for approximating the function of the developed scanning microscope. The implemented approximation method is described in this chapter based on the more rigorous approach to the general problem of multivariate polynomial approximations given by Phillips [Phi03].

It can be shown that, given a positive integer n and a set of points S_n defined by Equation 4.17 where every x_i, y_j and z_k are distinct, then there is a unique polynomial $p(x,y,z)$, with degree n, given by Equation 4.18 that takes the same values as a function $f(x,y,z)$ on the set S_n.

$$S_n = \{(x_i, y_j, z_k) \mid i,j,k > 0, i+j+k \leq n\} \tag{4.17}$$

$$p(x,y,z) = \sum_{i=0}^{n} \sum_{j=0}^{(n-i)} \sum_{k=0}^{(n-i-j)} c_{i,j,k} x^i y^j z^k \tag{4.18}$$

The reason behind S_n is to define a minimal data set to guarantee that the polynomial coefficients $c_{i,j,k}$ can be uniquely determined though a linear system of equations as illustrated in Equation 4.19 for the case $n = 2$.

For representing the function F_{LSM} using this approach, one different polynomial is necessary for representing each of the cartesian coordinates of the system's focus point. Another possibility, as mentioned in Chapter 4.4.1, is to use the paraxial or the ray-tracing model for representing the P_x and P_y coordinates and use a single polynomial to correct the system errors only on P_z. Although this approach does not take in account the errors in X and Y it has the advantage that a complex measurement rig as shown in Figure 4.20 is not necessary. In

this work the paraxial approach was used. The obtained results are presented and discussed in Chapter 5.

$$\begin{bmatrix} c_{0,0,0} \\ c_{1,0,0} \\ c_{0,1,0} \\ c_{0,0,1} \\ c_{2,0,0} \\ c_{1,1,0} \\ c_{1,0,1} \\ c_{0,2,0} \\ c_{0,1,1} \\ c_{0,0,2} \end{bmatrix}_{10\times 1} = \boldsymbol{A}^{-1} \begin{bmatrix} f(x_0,y_0,z_0) \\ f(x_1,y_0,z_0) \\ f(x_0,y_1,z_0) \\ f(x_0,y_0,z_1) \\ f(x_2,y_0,z_0) \\ f(x_1,y_1,z_0) \\ f(x_1,y_0,z_1) \\ f(x_0,y_2,z_0) \\ f(x_0,y_1,z_1) \\ f(x_0,y_0,z_2) \end{bmatrix}_{10\times 1} \quad | \ (x_i,y_j,z_k) \in S_n \tag{4.19}$$

$$\boldsymbol{A} = \begin{bmatrix} 1 & x_0 & y_0 & z_0 & x_0^2 & x_0y_0 & x_0z_0 & y_0^2 & y_0z_0 & z_0^2 \\ 1 & x_0 & y_0 & z_1 & x_0^2 & x_0y_0 & x_0z_1 & y_0^2 & y_0z_1 & z_1^2 \\ 1 & x_0 & y_0 & z_2 & x_0^2 & x_0y_0 & x_0z_2 & y_0^2 & y_0z_2 & z_2^2 \\ 1 & x_0 & y_1 & z_0 & x_0^2 & x_0y_1 & x_0z_0 & y_1^2 & y_1z_0 & z_0^2 \\ 1 & x_0 & y_1 & z_1 & x_0^2 & x_0y_1 & x_0z_1 & y_1^2 & y_1z_1 & z_1^2 \\ 1 & x_0 & y_2 & z_0 & x_0^2 & x_0y_2 & x_0z_0 & y_2^2 & y_2z_0 & z_0^2 \\ 1 & x_1 & y_0 & z_0 & x_1^2 & x_1y_0 & x_1z_0 & y_0^2 & y_0z_0 & z_0^2 \\ 1 & x_1 & y_0 & z_1 & x_1^2 & x_1y_0 & x_1z_1 & y_0^2 & y_0z_1 & z_1^2 \\ 1 & x_1 & y_1 & z_0 & x_1^2 & x_1y_1 & x_1z_0 & y_1^2 & y_1z_0 & z_0^2 \\ 1 & x_2 & y_0 & z_0 & x_2^2 & x_2y_0 & x_2z_0 & y_0^2 & y_0z_0 & z_0^2 \end{bmatrix}_{10\times 10} \quad | \ (x_i,y_j,z_k) \in S_n \tag{4.20}$$

Chapter 5

Experimental Results

In order to evaluate different characteristics of the developed scanning system and the efficacy of the proposed correction strategies, a series of different measurement tasks and simulations were conducted and are presented and discussed in this section. Using a large variety of samples (e.g. plane mirrors, spheres, gratings, calibrated steps, μ-lenses, *Si*-structures, etc.), characteristics such as repeatability, measurement uncertainty, spot size and maximum surface inclination were investigated.

For the experiments presented in this chapter, a single sensor lens (ASP6×22) was used together with 3 different objective lenses (ZEISS8, ASP15×15, PCX15×15). Excluding the ZEISS8 lens, all lenses were described through the even asphere equation (Equation 2.7) and the aspheric coefficients in Table 5.1. The ZEISS8 lens is a high-end infinity compensated microscope objective. It was simulated as a paraxial lens and used as a control lens for comparison with other objective lenses.

5.1 Characteristic Curve of the Sensor

The characteristic curve of the focus sensor is described by the S-Curve shape discussed in Chapter 2.4. This curve defines the linear operation region of the sensor, the sensitivity of the focus detection and, therefore, the achievable vertical resolution. The final shape of the S-Curve is defined by all the involved elements (sensor lens, objective, photodiode geometry, etc.). For the specific case of the focus detection using the obscuration method, it has been shown in Chapter 4.3 that, for a

Table 5.1: Parameters and coefficients of the used lenses.

ASP15×15 ($f_{ob} = 15mm$)	
Coefficient	Value
C	$0.113122mm^{-1}$
K	-1.427973
K_2	0.0
K_4	1.577441×10^{-4}
K_6	-6.152039×10^{-8}
K_8	8.528969×10^{-10}
K_{10}	$-3.504659 \times 10^{-12}$
TH	$5.5mm$
$n_{\lambda=650nm}$	1.58618

ASP6×22 ($f_{ob} = 22mm$)	
Coefficient	Value
C	$0.080296mm^{-1}$
K	0.5823493
K_2	0.0
K_4	0.0
K_6	2.801315×10^{-9}
K_8	0.0
K_{10}	0.0
TH	$2.0mm$
$n_{\lambda=650nm}$	1.56599

PCX15×15 ($f_{ob} = 15mm$)	
Coefficient	Value
C	$0.099108mm^{-1}$
K	0.0
K_2	0.0
K_4	0.0
K_6	0.0
K_8	0.0
K_{10}	0.0
TH	$5.5mm$
$n_{\lambda=650nm}$	1.66711

ZEISS8	
Parameter	Value
f_{ob}	$8.225mm$

paraxial system, the sensitivity of the system (i.e. the slope of the S-Curve at the origin) is theoretically infinite. Nevertheless, the actual slope of the S-Curve will in praxis be limited by the optical aberrations of the system (Figure 4.15) and by diffraction.

In order to experimentally observe the behaviour of the characteristic curve of the system, the sensor signal was measured for different positions (θ_x, θ_y) of the tilting mirror using a flat mirror sample. For the measurements, the flat mirror was positioned within the working range of the system and the lens position (Δ_z) scanned through the complete working range ($0 - 100\mu m$). Figure 5.1 shows the obtained characteristic curves for the different positions of the tilting mirror, using two different objective lenses (Table 5.1).

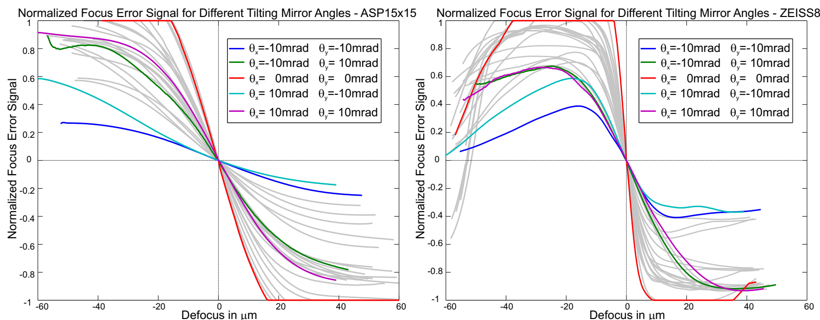

Figure 5.1: Characteristic curve of the system for different positions (θ_x, θ_y).

Using a flat mirror as a sample, the inclination of the sample is constant, so that the observed changes in the S-Curve are caused by the scanning angles θ_x and θ_y. That is, due to the non-telecentricity of the scanning system, the angles θ_x and θ_y modify the incident angle of the focused light on the probe, changing the characteristic curve as discussed in Chapter 4.3. The slope of the characteristic curve near the zero-crossing defines the sensitivity of the system to a small defocus. Using the measured curves shown in Figure 5.1 and interpolating the obtained results, it is possible to obtain a defocus sensitivity map for the system as shown in Figure 5.2.

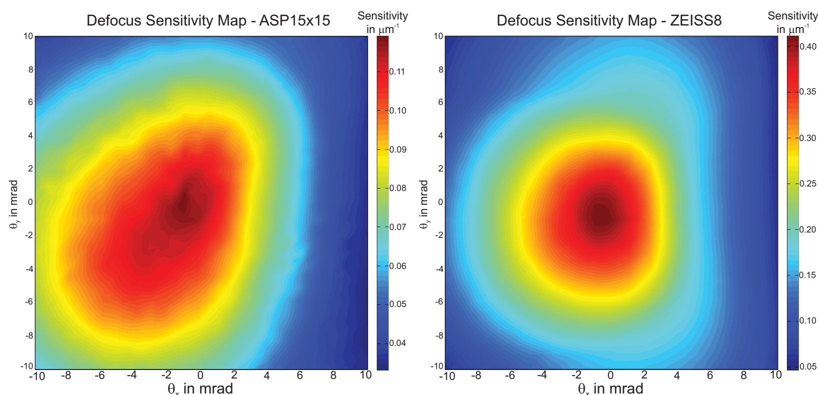

Figure 5.2: Measured S-Curve slope for different mirror tip-tilt angles (θ_x, θ_y).

Figure 5.2 shows the variation of the slope of the system's characteristic curve depending on the tilting angles (θ_x, θ_y). The system has a maximum in sensitivity when the incident angle of the focused light is perpendicular to the sample. Figure 5.2 also illustrates the reduction of the system's sensitivity due to the variation of the focal length and the use of suboptimal optics.

Considering only the curve slopes observed in Figure 5.2 and the resolution of the used AD Converters (Chapter 3.4), it is possible to calculate a theoretical limit for the resolution with which the defocus of the system can be measured. Considering the used AD converters with a resolution of 16 bits and amplifying the FES to cover the entire voltage range of $\pm 10V$, the minimum detectable variation of the normalized FES will be approximately 3×10^{-5} and, consequently, the minimum

detectable defocus will vary from $0.3nm$ to $1nm$ for the ASP15×15 lens and from $0.1nm$ to $0.3nm$ for the high-end microscope objective (ZEISS8).

5.2 Error and Sensitivity Analysis

An instrument is defined through its structure and its interaction with the environment and it will always perform its task with an associated inaccuracy [Kra00]. This inaccuracy depends on a series of factors such as the instrument's working principle, manufacturing and assembling. Even though it can be minimized, as shown in Chapter 4.2, this associated inaccuracy will always be present. In Chapter 4 the developed laser scanning microscope was described as a mathematical function $F_{LSM}(x, Q)$, where Q represents the parameters of the system and fully describes its structure and functionality. In this section, the implemented ray-tracing model is used to evaluate the influence of each parameter in the error behaviour of the developed scanning microscope.

However, before describing the error behaviour of the system, it is wise to introduce two important related concepts and their definitions: invariance, and innocence [Sch82, Kra00]. Both concepts are widely used in mechanical and optical design in order to minimize the influence of manufacturing and assembling deviations as well as environmental variations in the output of a system. Equation 5.1 illustrates these concepts mathematically.

$$\Delta_\Omega = V_1\Delta_Y + V_2(\Delta_Y)^2 + \cdots + V_n(\Delta_Y)^n$$
$$\begin{cases} V_1 = V_2 = \cdots = V_n = 0 & \rightarrow \text{Invariance} \\ V_1 = 0 & \rightarrow \text{Innocence} \end{cases} \tag{5.1}$$

A system is invariant or innocent according to its error coefficients $V_1 \cdots V_n$. It is invariant if its output Ω is not influenced by a disturbance Δ_Y of a parameter Y, and it is innocent if a disturbance causes only second or higher order errors. The error coefficients V_n can be determined through the Taylor series accordingly to Equation 5.2.

$$V_n = \frac{\partial^n \Omega(\Upsilon)}{\partial \Upsilon^n} \frac{1}{n!} \tag{5.2}$$

These error coefficients can be used to evaluate a system regarding its sensitivity and the influence of eventual parameter errors. Tight tolerances and model calibration minimize the magnitude of the deviations between the real system and its mathematical model, but it is still expected that the system presents a certain behaviour associated with a set of design parameters. Even though eventual errors can be corrected to a certain point, as explained in Chapter 4.3, it is important to identify which parameter deviations are mostly prejudicial for a system and, if necessary, resort to the use of adjustment setups and compensation.

Regarding the identification of the error coefficients (Equation 5.2), the model-based approach proves itself much more adequate then the experimental approach based on look-up tables and polynomials. LUTs and Polynomials do not define a direct relation between constructive parameters and the system's outputs, so that no error analysis is possible. Using the developed ray-tracing model (Chapter 4.3) for describing the function $F_{LSM}(x, Q)$, the first error coefficient V_1 for each one of the system's kinematic parameters defined in Table 4.3 can be numerically determined according to Equation 5.2. However, some important points must first be considered. The error coefficients vary depending on the used lenses and on the system's position $x = [\theta_x, \theta_y, \Delta_z]$ and, as the scanning system is a relative measurement system, an adequate global coordinate frame must be chosen so that, for example, a displacement of the whole system in the space does not become mathematically interpreted as an error.

In order to investigate the sensitivity of the system to eventual misalignments of its components, the function F_{LSM} was investigated regarding small variations of the rotation (R_x, R_y, R_z) and translation (T_x, T_y, T_z) parameters of its homogeneous transformations defined in Table 4.3.

Figure 5.3 shows the maximal error coefficients for the system output $[P_x, P_y, P_z]$ within the working volume ($\theta_x = -25 \cdots 25mrad$, $\theta_y = -25 \cdots 25mrad$, $\Delta_z = 0 \cdots 100\mu m$), considering the global coordinate frame (see Figure 4.14) at the system's focal point for the position $x =$

$[0,0,0]$ and the sensor and objective lenses as paraxial lenses with $f'_s = 22mm$ and $f'_{ob} = 15mm$. Given a parameter ζ_i from the system, the associated error coefficient was calculated according to Equation 5.3.

$$\begin{cases} \frac{\partial F_{LSM}(x_0,Q_0)}{\partial \zeta_i} = \begin{bmatrix} \frac{\partial P_x(x_0,Q_0)}{\partial \zeta_i} \\ \frac{\partial P_y(x_0,Q_0)}{\partial \zeta_i} \\ \frac{\partial P_z(x_0,Q_0)}{\partial \zeta_i} \end{bmatrix} \\ V_{1,\zeta_i} = \max\left(\sqrt{\left(\frac{\partial P_x(x_0,Q_0)}{\partial \zeta_i}\right)^2 + \left(\frac{\partial P_y(x_0,Q_0)}{\partial \zeta_i}\right)^2 + \left(\frac{\partial P_z(x_0,Q_0)}{\partial \zeta_i}\right)^2}\right) \end{cases} \tag{5.3}$$

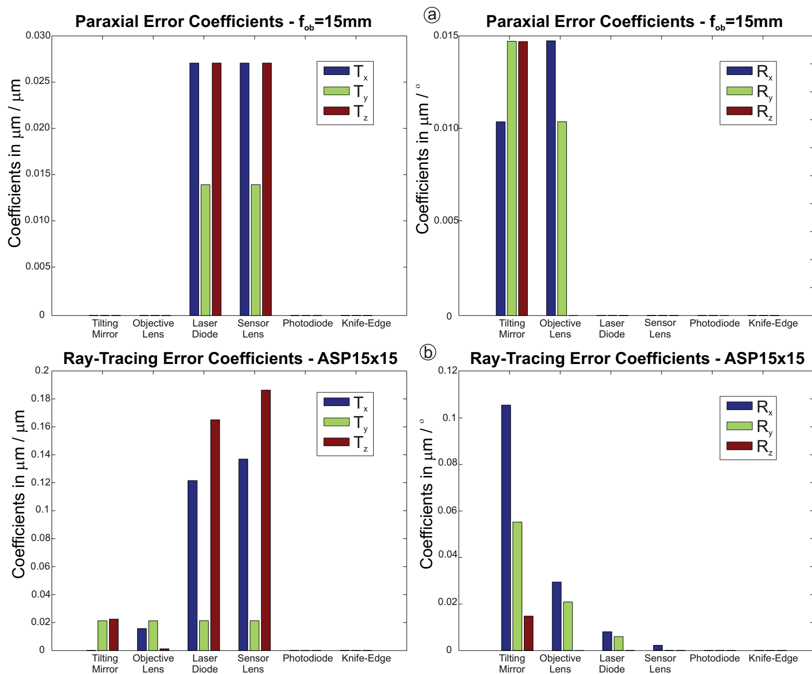

Figure 5.3: Simulation of the error coefficients of the system using the paraxial and ray-tracing models.

The error coefficients of the paraxial system shown in Figure 5.3a illustrate the robustness of the system. Considering only the position of its components, the system is innocent regarding small displacements of all components with exception to the displacement of the sensor lens and the photodiode; that is, the distance between photodiode and sensor lens. By changing this distance, the collimation of the laser is strongly influenced, causing not only a displacement of the entire focal plane of the system, but also inserting a curvature, influencing the X, Y and Z positions of the detected focus point. Regarding the orientation of its components, although not innocent, the system demonstrates a highly insensitive behaviour. The angle of incidence of the laser on the objective lens has a strong influence on the X and Y positions of the focus point.

Figure 5.3b shows the error coefficients obtained using the same simulation procedures when the lenses are not considered paraxial. Using the ray-tracing model and the ASP15 $\times$ 15 and ASP6 $\times$ 22 as objective lens and sensor lens respectively, the influence of the optical aberrations in the error coefficients can be observed. Not only is the system more sensitive to eventual misalignments, but also loses its innocence regarding various parameters.

The error coefficients of the system are important for the numerical identification of the system's model. They define which parameters should be calibrated and which ones can not be calibrated. Chapter 5.3 shows the results of the system's calibration.

5.3 Model Calibration and Function Measurement

As explained in Chapter 4.3.3, the calibration of the system's model consists of the identification of its functional parameters based on measured data. This way, the discrepancies between the model and the real system caused by manufacturing and assembly tolerances are minimized.

The first step in order to calibrate the system's model F_{LSM} is to define which parameters are to be identified. The following two characteristics are the most important when using kinematic chains to mathematically describe a system: continuity and minimality [GM11]. They directly influence the parameter identification process and are related to model smoothness and to parameter redundancies in the model. Mathematically, model continuity is equivalent to continuity of the inverse function of the model (${F_{LSM}}^{-1}$). This way, parameterizaton's singularity can be defined as a rank deficiency in the jacobian matrix (Equation 4.11) and each parameterization can be investigated concerning its singularities through the detection of the zeros of the determinant $\det({J_{LSM}}^T J_{LSM})$.

To avoid singularities and numerical instability in the calibration process, not all parameters should be identified, or, in other words, invariant parameters should not be included in the identification process. Repeating the error analysis shown in Chapter 5.2 for the function F'_{LSM}, Table 5.2 shows the parameters included in the identification process and their values before and after the calibration procedure. The tilting mirror was chosen as reference for defining the global coordinate frame.

The identification of the system's parameters is done using a high quality ($\lambda/20$) flat mirror as a reference artifact and considering it as a perfect plane. After measuring the flat mirror, its surface is reconstructed using the ray-tracing model and the acquired data ($\theta_x, \theta_y, \Delta_z$). Comparing the obtained surface with an ideal geometric plane, all deviation can be interpreted as model errors and the system's parameters modified as shown in Chapter 4.3.3 in order to minimize these deviations.

Table 5.2: Calibrated parameters of the ray-tracing model.

Laser Diode (T_{0-1})		
Parameter	Value	Correction
$T_{x,1}$	$0mm$	$0.00mm$
$T_{y,1}$	$-72.0mm$	$0.10mm$
$T_{z,1}$	$0mm$	$-0.08mm$
$R_{x,1}$	$-90°$	$0.00°$
$R_{y,1}$	$0°$	$0.08°$
$R_{z,1}$	$0°$	–

Mirror - (T_{0-2})		
Parameter	Value	Correction
$T_{x,2}$	$0mm$	–
$T_{y,2}$	$2.83mm$	–
$T_{z,2}$	$-2.83mm$	–
$R_{x,2}$	$-135°$	–
$R_{y,2}$	$0°$	–
$R_{z,2}$	$0°$	–

Objective Lens - (T_{0-3})		
Parameter	Value	Correction
$T_{x,3}$	$0mm$	$-0.05mm$
$T_{y,3}$	$0mm$	$0.15mm$
$T_{z,3}$	$45.0mm + \Delta_z$	$0.00mm$
$R_{x,3}$	$0°$	$-0.57°$
$R_{y,3}$	$0°$	$-0.26°$
$R_{z,3}$	$0°$	–

Sensor Lens - (T_{0-4})		
Parameter	Value	Correction
$T_{x,4}$	$0mm$	$0.00mm$
$T_{y,4}$	$-50.0mm$	$0.01mm$
$T_{z,4}$	$0mm$	$0.00mm$
$R_{x,4}$	$90°$	$0.24°$
$R_{y,4}$	$0°$	$-0.16°$
$R_{z,4}$	$0°$	–

Knife-Edge - (T_{0-5})		
Parameter	Value	Correction
$T_{x,5}$	$0mm$	–
$T_{y,5}$	$-70.0mm$	–
$T_{z,5}$	$0mm$	–
$R_{x,5}$	$90°$	–
$R_{y,5}$	$0°$	–
$R_{z,5}$	$0°$	–

Photodiode - (T_{0-6})		
Parameter	Value	Correction
$T_{x,6}$	$0mm$	$0.00mm$
$T_{y,6}$	$-72.0mm$	$0.00mm$
$T_{z,6}$	$0mm$	$0.04mm$
$R_{x,6}$	$0°$	$0.20°$
$R_{y,6}$	$0°$	$0.00°$
$R_{z,6}$	$0°$	–

Sample - (T_{0-7})		
Parameter	Value	Correction
$T_{x,7}$	$0mm$	–
$T_{y,7}$	$0mm$	–
$T_{z,7}$	$0mm$	–
$R_{x,7}$	$0°$	–
$R_{y,7}$	$0°$	–
$R_{z,7}$	$0°$	–

5.4 Error Correction Methods

In Chapter 4.2, three different strategies were proposed in order to address the measurement errors introduced in the system by the use of a minimal optical schema and uncompensated optics. The first strategy is based on the simulation of the system using a ray-tracing model and its calibration, the second one is based on the use of a look-up table (LUT) and the third one on the use of a polynomial.

In order to quantitatively evaluate these error correction strategies, a $\lambda/20$ flat mirror was used as a sample and scanned in different positions within the working volume using the ASP15$\times$15 lens as objective. If the lenses used were paraxial, the expected surface would be a highly flat surface with random noise in the range of approximately $\pm 50nm$ due to the positioning resolution of the objective lens ($\pm 13nm$) and the surface quality of the mirror ($\lambda/20 \approx 30nm$). By reconstructing the measured surface using the paraxial model, the curved surface illustrated in Figure 5.4 is obtained. This curvature illustrates the deviation between the real system and the paraxial model and is caused mainly by the optical aberrations in the system.

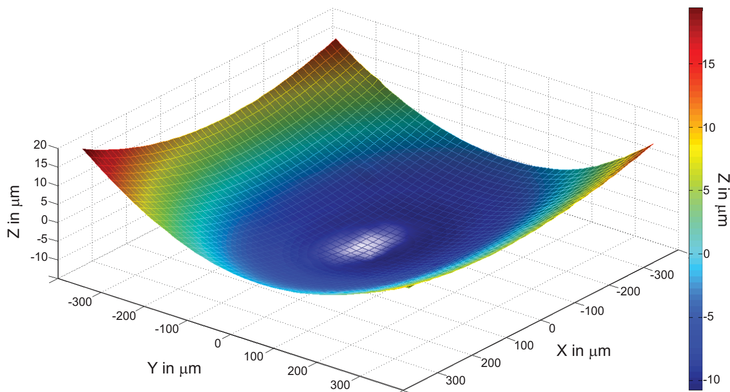

Figure 5.4: Surface of a $\lambda/20$ flat mirror using the paraxial model (ASP15$\times$15).

Regarding the mirror surface as a perfect flat, the deviations between the reconstructed surface shown in Figure 5.4 and a perfect geometric plane can be interpreted as the modelling error. With this approach, the captured data ($[\theta_x, \theta_y, \Delta_z]$) from the $\lambda/20$ flat mirror was used to reconstruct its surface using all the proposed error correction strategies presented in Chapter 4.2. Figure 5.5 shows the obtained results and average shape deviation for each one of the correction methods and for the surface reconstructed directly with the paraxial model (Figure 5.4).

For the paraxial model, the observed average shape deviation was $5\mu m$ and by observing the shape of the error surface in Figure 5.5a, the presence of systematic errors caused by the optical aberrations in the

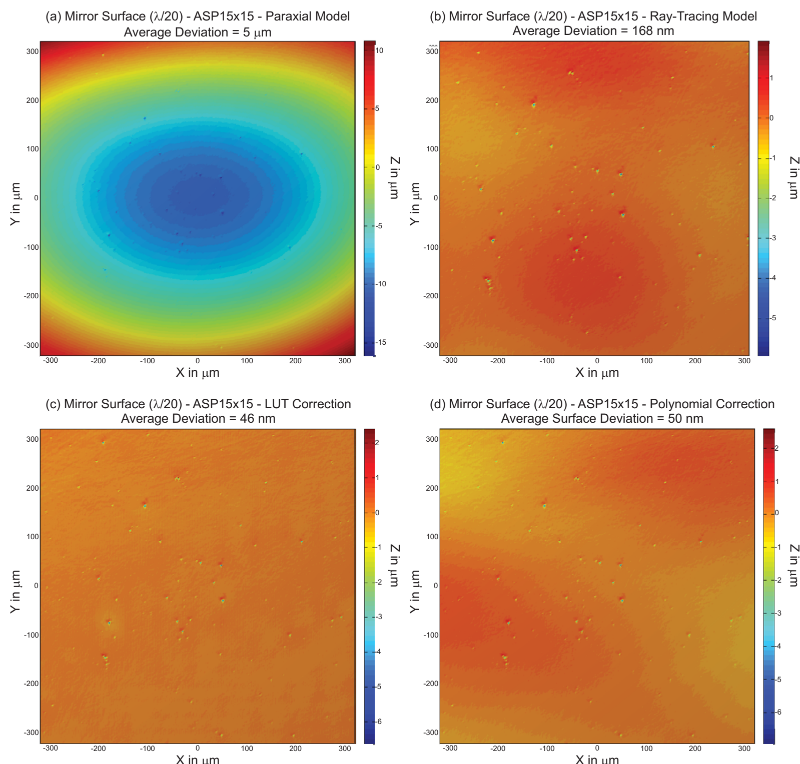

Figure 5.5: Surface of a $\lambda/20$ mirror using different correction methods (ASP15$\times$15).

measurement is evident. Figure 5.5b-d shows the reconstructed mirror surface using the ray-tracing model and the LUT and polynomial correction methods respectively. In all three methods, the reduction of the observed deviations is evident. Not only could the clear presence of systematic error given by the surface's curvature be eliminated, but the observed average deviations in all three methods were found to lie within the expected measurement noise (approximately 50nm). In all the images it is also possible to observe small particles on the measured mirror surfaces.

Between the obtained results, the look-up table approach displays the best results, reducing the average surface deviations to approximately $40nm$. As the LUT and the polynomial are only measurement based methods, they take into account an average of all deviations in the system, including effects that are not described by the implemented ray-tracing model such as diffraction effects, back reflections and scattering on the optical components. Nevertheless, the ray-tracing model also achieved extremely positive results, reducing the average shape deviation to $168nm$.

The same $\lambda/20$ flat mirror was also scanned using a high-end microscope objective. The obtained results are shown in Figure 5.6. Even though the used microscope objective is a highly compensated optical system, the influence of optical aberration can still be seen in the final results. These deviations occur as a result of the microscope objective not being used under its design conditions, which is caused by the minimal optical design of the whole system, and because of the optical aberration in the sensor lens (ASP6$\times$22).

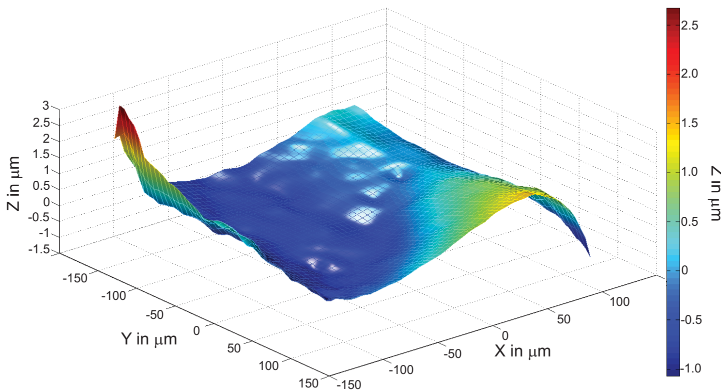

Figure 5.6: Surface of a $\lambda/20$ flat mirror using the paraxial model (ZEISS8).

Considering the ZEISS8 objective lens as a paraxial lens with a focal length of $8.225mm$, the ray-tracing model, as well as the LUT and polynomial methods, can be used to correct the measured surface. Figure 5.7 shows the obtained surfaces after the error correction.

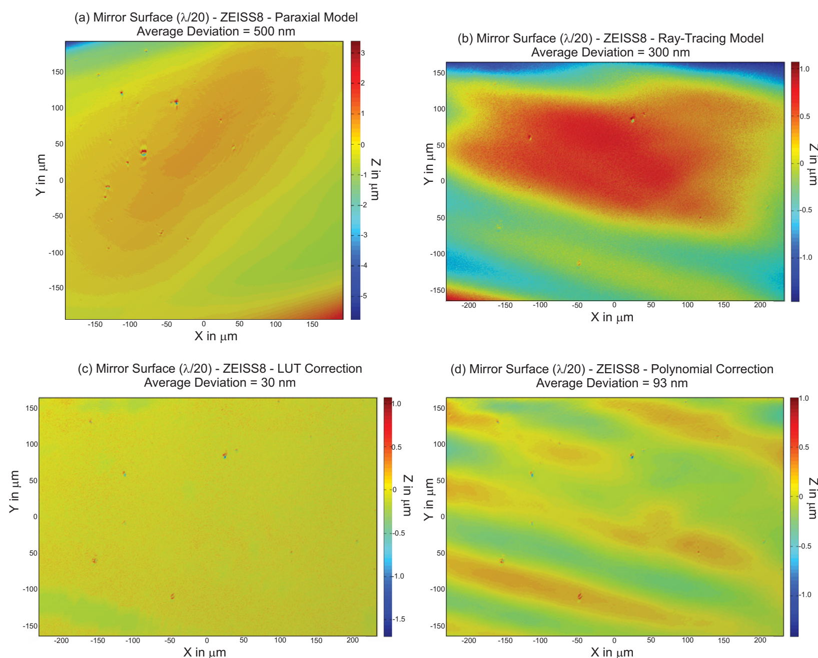

Figure 5.7: Surface of a $\lambda/20$ mirror using different correction methods (ZEISS8).

By comparing Figure 5.5 and Figure 5.7, it can be seen that, although the use of a compensated objective greatly reduces the deviations observed in the paraxial model, the final results are very similar for the polynomial and look-up table methods. With the use of these correction methods, both objectives have their measurement accuracy limited only by random errors caused by the electronic noise of the system and interpolation errors. Nevertheless, it is important to note that the optical aberrations also have an influence on the slope of the characteristic curve of the system, that is, its sensitivity. In Chapter 5.1, it was shown that the system is actually capable of detecting a defocus of at least $1nm$ and that the limiting factor for its axial resolution is the positioning of the objective ($\pm 12nm$). This limiting factor is the same for both used objectives (ASP15$\times$15, ZEISS8), however, by improving the positioning accuracy of the used linear stage with a high

resolution DA converter, the limiting factor of the achievable resolution would be the system's sensitivity. In this case, the quality of the compensated objective could be truly utilized.

It is important to note that the use of non-model-based correction methods such as LUTs or polynomials also leads to a growth of the measurement uncertainty of the system. The numerical correction functions are constructed through the measurement of an artifact and have within them an associated measurement uncertainty given by the repetability of the system and the surface quality of the used artifact. When reconstructing a surface using one of these methods, the final measurement uncertainty will be given by the addition of the uncertainty of the numerical function and of the actual measurement.

5.5 Influence of the Model Calibration

As discussed in Chapter 4.3.3, given a mathematical model of a real system and its design parameters, deviations between the model's parameters and the real system will always occur due to manufacturing and assembly tolerances for example. In order to minimize these differences, it is necessary to calibrate the model. In Chapter 5.3, the experimental calibration procedure and the obtained results were shown and discussed and in this section a comparison between the calibrated and uncalibrated models is shown.

Scanning a $\lambda/20$ flat mirror, its surface was reconstructed using the calibrated and the uncalibrated models. Figure 5.8 shows the obtained results using the same evaluation criteria as in Figure 5.5. Through the identification of the parameters of the real system, the residual error in the reconstructed surface of the sample mirror was reduced from $1.9\mu m$ to $168nm$ improving the results of the ray-tracing model by almost 90%.

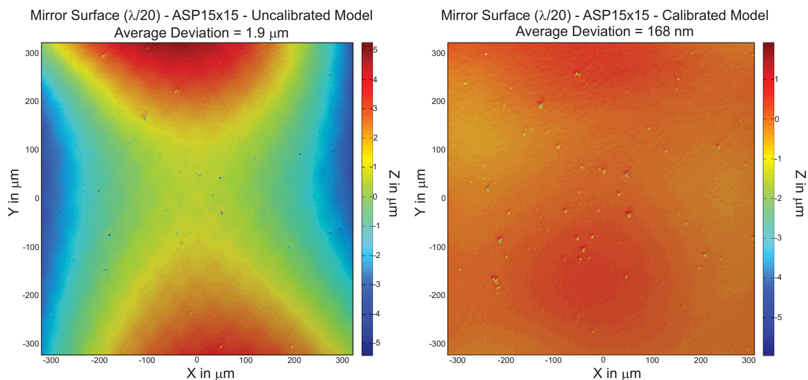

Figure 5.8: Surface of a $\lambda/20$ mirror using the ray-tracing model with and without calibration.

5.6 Influence of Sample Inclination in the Measurements

When working with optical-based measurement techniques, the slope or inclination of the scanned surfaces also has an influence on the measurements. This influence was modelled and discussed in Chapter 4.3 using the paraxial model of the developed scanning system and it demonstrated that, although an inclination of the sample surface reduces the sensitivity of the system, the focal point can still be accurately detected. That is, the zero position of the focus detection system is insensitive to the surface inclination and no systematic errors arise.

Nonetheless, the focus detection system works based on the light reflected by the sample's surface and in the worst case, depending on the surface inclination, the incident light can be reflected away and the measurement of the surface will not be possible. Considering the scanning system in its central position ($\theta_x = \theta_y = 0$), Figure 5.9 shows the deflection of the incoming laser beam on the sample surface. The theoretical maximum measurable local slope is then given by the maximum angle β_{max} in which the objective still collects the returning beam as shown in Equation 5.4.

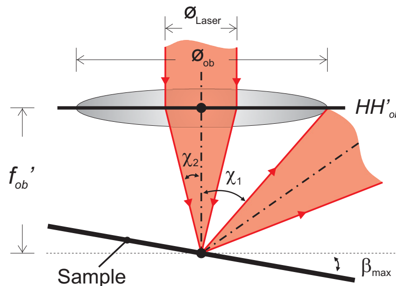

Figure 5.9: Maximum measureable surface inclination.

$$\begin{cases} \chi_1 = \arctan\left(\frac{\varnothing_{ob}}{2f_{ob}}\right) \\ \chi_2 = \arctan\left(\frac{\varnothing_{Laser}}{2f_{ob}}\right) \end{cases} \rightarrow \beta_{max} = \frac{\chi_1 + \chi_2}{2} \qquad (5.4)$$

Considering the developed system and its parameters, the maximum measurable surface inclination is, according to Equation 5.4, $\beta_{max} = 23°$ for the ZEISS8 objective and $\beta_{max} = 17°$ for the ASP15×15. However, this inclination limit does not take optical aberrations into account, only reflected light. When considering real probes, the surface roughness also causes part of the incoming light to scatter and this portion of the light is also used by the measuring system so that the maximum measurable inclination also depends on the surface roughness.

The surface roughness can either increase or decrease the maximum measurable inclination. Normally, a small roughness in the range of $0.05\mu m$ (R_a) improves the maximum measurable inclination β_{max}, but as the surface roughness increases ($R_a \geq 1\mu m$), β_{max} decreases [Mas12, Lea11]. As the surface roughness increases, the micro-geometry of the surface also causes speckles in the reflected light and generates high-frequency noise in the measurements [FY05, Lea11]. Fukatsu [FY05] studied this effect and proposed different methods to address it. The influence of speckles on the measurement does not lie in the scope of this work and was considered as random noise.

Another effect that influences the maximum measurable surface inclination is the focus detection system. As discussed in Chapter 4.3.1 and Figure 4.7, the surface inclination degrades the FES and, in some cases, renders the focus point measurement impossible.

In order to determine the value of the maximum measurable angle experimentally, two different experiments were conducted. Firstly, a plane mirror was used as a sample and its inclination angle gradually changed. For each different inclination of the plane mirror, the S-Curve of the sensor and the mirror surface were measured. Figure 5.10 shows some of the obtained sensor curves for different inclination angles of the sample mirror using the ZEISS8 and ASP15×15 objectives.

Figure 5.10 clearly shows the degradation of the FES and the reduction of the quasi-linear region of the curve as the inclination of the sample increases. Considering both implemented scanning procedures shown in Chapter 3.3, the continuous scanning is extremely sensitive to this degradation, whilst the stepwise scanning presents itself as relatively robust against it as the zero-crossing of the S-Curve remains unaffected. The maximum measurable sample inclination observed

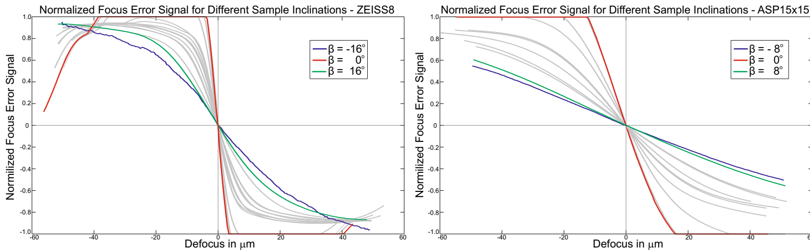

Figure 5.10: Influence of the sample inclination on the FES.

using this method was approximately $\pm 16°$ for the ZEISS8 objective and $\pm 8°$ for the ASP15$\times$15.

The second experimental test to determine the maximum measurable sample inclination was the measurement of a steel sphere. A sphere has a constant changing inclination and offers an ideal sample for testing the maximum measurable angle in samples with low roughness. Figure 5.11 shows the obtained measurement results using a sphere with the nominal diameter $\varnothing = 2mm$ and the ZEISS8 objective.

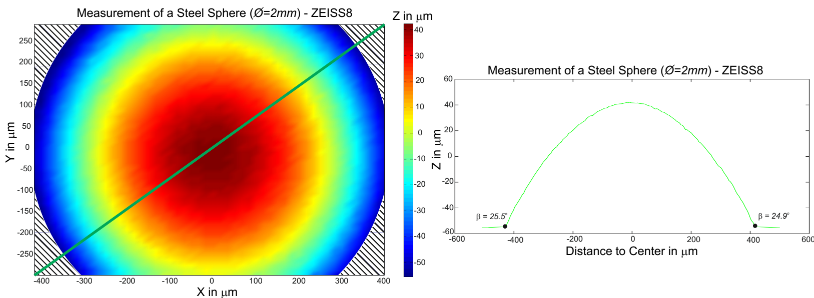

Figure 5.11: Maximum measurable angle in a steel sphere ($\varnothing = 2mm$).

The hatched areas in Figure 5.11 show the positions within the scanned area where no measurement could be made due to the degradation of the FES. Figure 5.11 also shows a single scan line along the X and Y axes and the respectively maximum measured angles. The maximum angles obtained with the measurement of the sphere are slightly larger than the theoretically expected ones (Equation 5.4). This happens not only due to the roughness of the sphere surface and the scattered light

as explained, but also due to the non-telecentricity of the system. Figure 5.12 illustrates this effect.

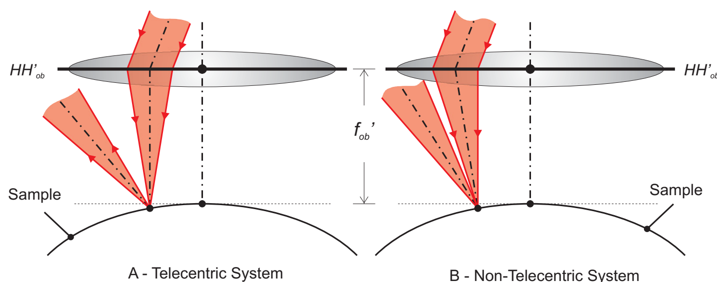

Figure 5.12: Non-telecentric ilumination and maximum measurable angle.

As explained in Chapter 3, due to mechanical constraints, the developed scanning system is not telecentric. It possesses a layout similar to the one illustrated in Figure 5.12, so that the maximum measurable angle will be larger for convex surfaces and smaller for concave surfaces.

5.7 Vertical and Lateral Resolution and Noise

As explained in Chapter 3, the vertical and lateral resolution of the developed scanning microscope are theoretically limited by the resolution of the analogue-digital and digital-analogue converters, the slope of the characteristic curve of the sensor and the spot size of the focused laser beam. These parameters determine the resolution of the scales used to measure the defocus of the system, the movement of the objective and the tilting angles of the mirror. In practice, however, the achievable positioning accuracy of the whole system will also be limited by the electronic noise of the components used as well as by environment parameters such as vibrations and temperature variations.

In this chapter, the vertical and lateral resolutions of the developed LSM are experimentally investigated as well as the noise in the measurement of the focus error signal (FES) and the variables θ_x, θ_y and Δ_z.

5.7.1 Vertical Resolution and Noise

The vertical resolution of an optical measurement system is normally determined by the depth of focus of the objective lens [Lea11]. However, in the case of auto-focus detection systems, it is defined by the repeatability of the auto-focus mechanism and by the resolution of the linear stage used for moving the objective lens.

As discussed in Chapter 3, the positioning resolution of the linear stage used is approximately $12nm$ due to the limited resolution of the AD and DA converters. Therefore, considering the slope of the characteristic curve (Chapter 5.1), the defocus can be measured with a maximum resolution of $0.3nm$ for the ASP15$\times$15 objective lens. That means that the theoretical vertical resolution is not restricted by the measuring principle, but by the positioning mechanism of the auto-focus system and by noise. Figure 5.13 shows the smallest movement step of the linear stage.

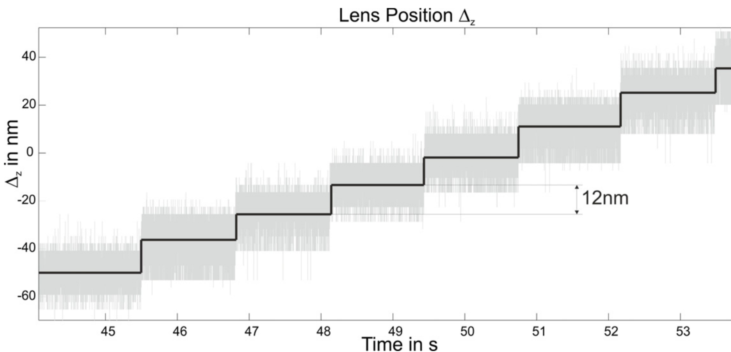

Figure 5.13: Minimal step of the linear stage of the objective lens (Δ_z).

In order to observe and experimentally evaluate the positioning noise of the objective lens within the control loop of the scanning procedure and its influence on the focus error signal, the angles θ_x and θ_y were held constant and the lens position controlled with a digitally implemented proportional-integral (PI) controller in order to always keep the FES at zero whilst using a flat mirror as a sample. Figure 5.14 shows the measured focus error signal and lens position (Δ_z) for the position $\theta_x = 0$ and $\theta_y = 0$.

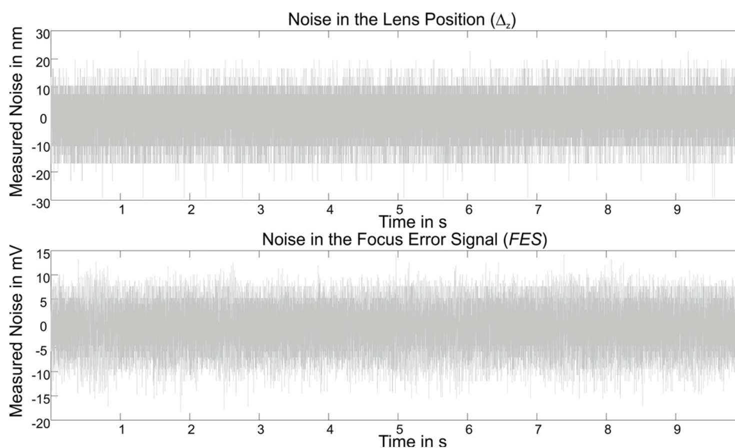

Figure 5.14: Measurement of the lens position Δ_z and the FES in closed loop.

Figure 5.14 shows that the noise observed in the measurement of the lens position Δ_z lies within the expected range of $\pm 12nm$ defined by the least significant digit of the DA converter. For the noise in the measurement of the FES, a noise of approximately $\pm 10mV$ was observed. This noise is not only generated by electronic noise in the system, but also by the positioning noise of the lens and the mirror. In other words, the noise observed in the focus error signal is influenced by all system variables as well as by the properties of the measured sample (for example reflectivity and roughness).

Repeating the procedure illustrated in Figure 5.14, the standard deviation of the measurements of Δ_z and FES can be charted for different positions of the tilting mirror (θ_x, θ_y) as shown in Figure 5.15.

Figure 5.15 shows that, although the measurement noise in the lens position Δ_z stays relatively constant throughout the working range, the observed noise in the focus error signal decreases as the angles θ_x and θ_y move away from the central position. This effect is caused by the variation of the system's characteristic curve shown in Chapter 5.1. As the angles θ_x and θ_y move away from the central position, the FES becomes less sensitive, so that the positioning noise of the focus lens ($\pm 12nm$) causes a smaller fluctuation of the focus error signal.

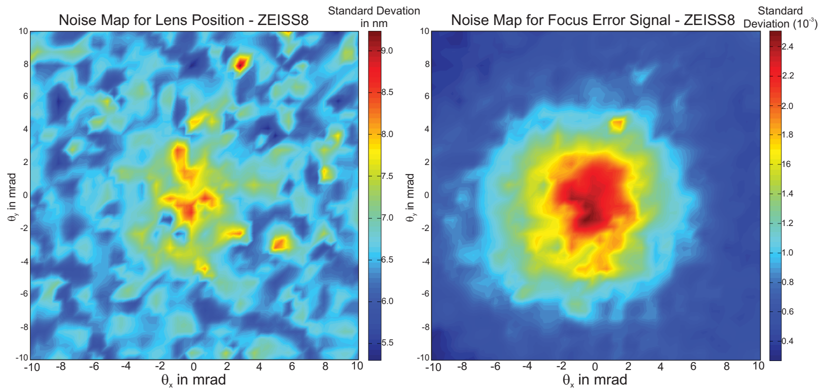

Figure 5.15: Measurement noise of the lens position Δ_z and the FES in closed loop for different angle positions.

The noise observed in both signals (Δ_z, FES) corresponds with the resolution limits of the AD converter for positioning the objective lens. Therefore electronic noise does not present a problem or a limit to the actual scanning system and the current restricting factor is the resolution of the used AD/DA converters (16/14 bits).

5.7.2 Lateral Resolution and Noise

There are two main factors that influence the lateral resolution of the developed scanning system. The first factor is the resolution of the tilting angles θ_x and θ_y and the second one the spot size of the focused laser. The resolution of the tilting angles, discussed in Chapter 3, has a theoretical value of $6\mu rad$ for the angles θ_x and θ_y, and is limited only by the resolution of the used ADC/DAC and the electronic noise. Figure 5.16 shows the minimum step movement of the mirror's tilting angles and Figure 5.17 shows the associated noise observed in their measurement.

Figure 5.17 shows that the noise observed in the measurement of the angles θ_x and θ_y is in accordance with the expected noise of $\pm 6\mu rad$ from the used DAC (14 bits), which is the limiting parameter of the calculated theoretical resolution.

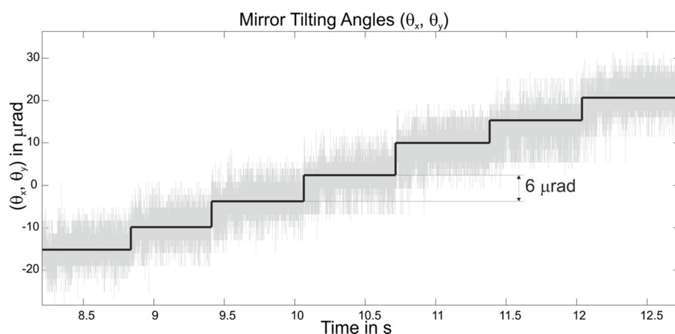

Figure 5.16: Minimal step of the tilting angles of the scanning mirror (θ_x, θ_y).

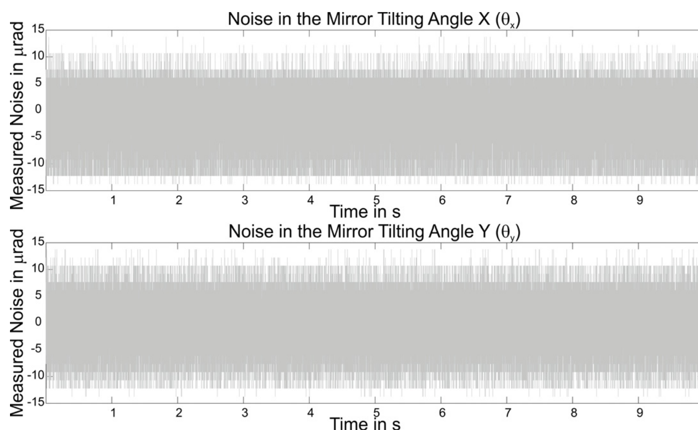

Figure 5.17: Measurement of the tilting angles θ_x and θ_y.

Considering the paraxial and ray-tracing models presented in Chapter 4.3, the obtained angular resolution can be converted into a spatial resolution in the X and Y directions as shown in Figure 5.18. Figure 5.18 defines the smallest lateral displacement of the focused laser stop in the lateral directions which are dependent on the actual angular position. Figure 5.18a illustrates the obtained step size using the paraxial model (Equation 4.3) with a lens with a focal length of 15mm and Figure 5.18b,c illustrate the results obtained using the ray-tracing model with a simple spherical lens (PCX15$\times$15) and an aspherical lens (ASP15$\times$15) as objectives (Table 5.1).

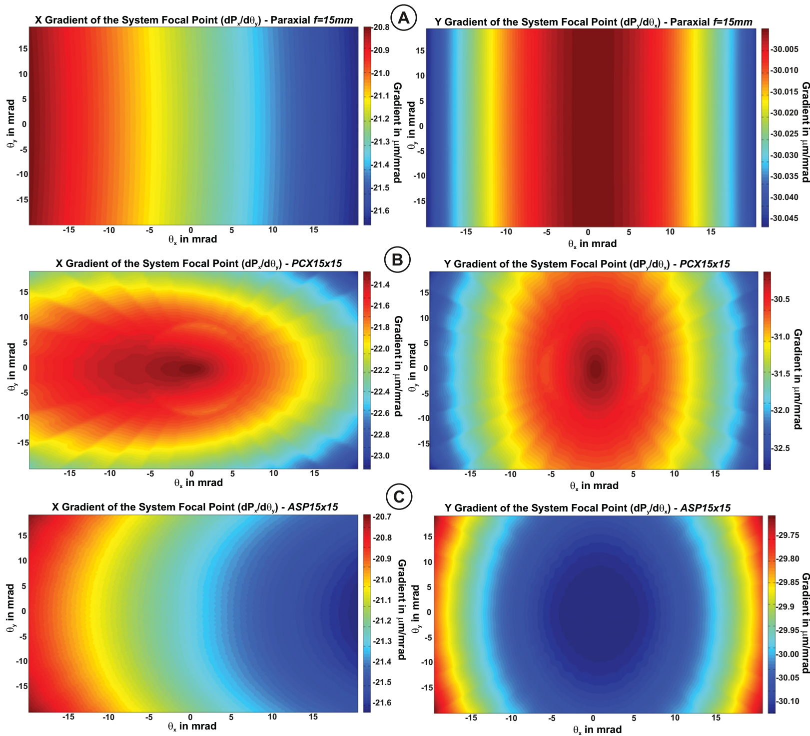

Figure 5.18: Simulation of the spatial step size of the scanning system.

All three lenses show similar behaviour. Due to the optical characteristics of the system, the minimum achievable step size is not constant within the measuring area. For the position of the focus point along the X axis, due to the 45° inclination of one of the rotation axes of the mirror in relation to the objective lens, the step size and the measurable range are smaller than in the Y axis. Also due to this inclination, the gradient of the step size changes monothonically.

For the Y axis, with the paraxial lens illustrated in Figure 5.18, the gradient has an optimum in the centre of the systems and, as the angles θ_x and θ_y increase, the absolute value of the gradient also increases and the spatial resolution decreases. This same behaviour can be observed for the spherical lens, but for the aspherical lens, this tendency

is inverted due to its surface shape and the distortion aberration. The minimum achievable step size improves as the angles θ_x and θ_y increase, but the gradient variation is much smaller because of the aspherical curvature of the lens and its residual barrel distortion. By comparing all the gradient maps in Figure 5.18, the influence of the uncompensated objectives in the step size can be clearly seen. The observed increase of the step size is much steeper for the spherical lens and the crosstalk between the X and Y position becomes larger for both spherical and aspherical lenses.

Using the gradients observed in Figure 5.18, the average step size for all three objectives can be determined as shown in Table 5.3.

Table 5.3: Average minimum step size for different objective lenses.

Lens	Step Size $[\mu m]$	
	X	Y
Paraxial ($f = 15mm$)	0.12	0.18
ASP15×15	0.12	0.18
PCX15×15	0.13	0.19

However, the achieved step size alone does not determine the lateral resolution of a scanning system. The optical scanning process can be seen as the convolution of a point spread function over a surface [Mar91, Bei95] and the spot size of the focused laser beam plays an important role. As discussed in Chapter 2.3, the spot size of the focused light beam can be defined by its diffraction on a circular aperture [Hec02, Haf94, Gro03], resulting in the Airy pattern shown in Figure 2.10. By considering the spot size as the diameter in which the intensity of the Airy disk is half of its maximum (FWHM - Full Width Half Maximum), the obtained spot size for a diffraction limited optical system will be given by Equation 5.5, where NA is the numerical aperture of the objective and λ the wavelength of the laser beam.

$$\varnothing_{FWHM} \approx 0.51 \frac{\lambda}{NA} \tag{5.5}$$

As the developed scanning system does not completely use the objective's aperture and does not use diffraction-limited optics, the resulting spot size will not always correspond with Equation 5.5. Equation 5.5 describes the diffraction-limited focusing of the light beam

and also does not take into consideration the optical aberrations, so that the actual resulting stop size for an uncompensated objective will be larger.

According to Equation 5.5, using the ASP15×15 lens described in Table 5.1 ($NA = 0.5$), the resulting spot size should be approximately $0.66\mu m$. Using the implemented ray-tracing model to simulate its spot size, the obtained results are shown in Figure 5.19.

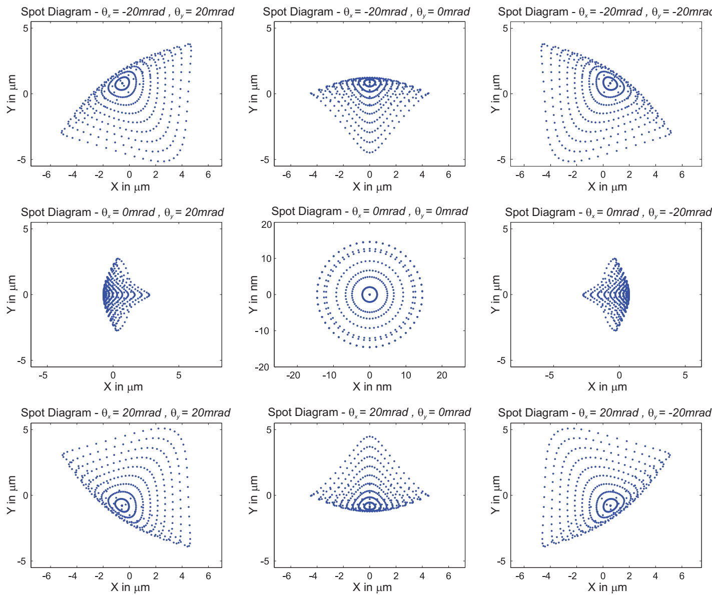

Figure 5.19: Simulation of the laser spot size for the ASP15×15 objective.

The used ASP15×15 lens is designed for the on-axis focusing of light and, as expected, shows a diffraction-limited performance only for small values of θ_x and θ_y. In the off-axis case, the spot size becomes larger. A direct measurement of the laser spot was not possible due to the short working distances of the system (e.g. $\approx 13mm$ for the ASP15×15) and the impossibility to attenuate the laser generated by the hologram unit. Therefore the worst simulated spot size with a diameter of approximately $8\mu m$ was considered. In a first approximation, the spot size acts as a low pass filter [Lea11] and offers a rough estimate of the lateral resolution of the system.

Figure 5.20 shows the measurement of a diffraction grating with 300 lines per millimetre using the ZEISS8 objective lens. The grating micro structure with its pitch of $3.3\mu m$ can be seen clearly.

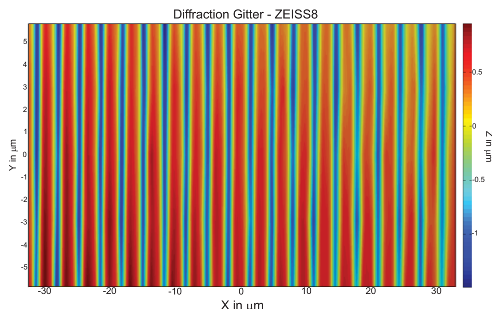

Figure 5.20: Measurement of a diffraction grating using the ZEISS8 objective.

5.8 Repeatability

Repeatability is the variability of the obtained results of many measurements of the same sample under the same conditions and is an important parameter in assessing the precision of a measurement instrument [JCG08].

In order to assess the repeatability of the developed system, a high quality flat mirror ($\lambda/20$) was used as a sample and its surface measured 12 times using the stepwise procedure. Using the paraxial model for reconstructing the scanned surfaces from the measured values [θ_x, θ_y, Δ_z], the average standard deviations for the X, Y and Z positions of the measured surface points are shown in Table 5.4 for the ASP15$\times$15 and ZEISS8 objectives.

Considering the simulated gradients, measured characteristic curves and measurement noise observed in the system variables $[\theta_x, \theta_y, \Delta_z]$ in Chapter 5.7, it can be observed that the experimentally obtained standard deviations lie within the expected values. Merging the values shown in Table 5.4 according to Equation 5.6 and using a coverage factor $k = 2$, the 3D repeatability (σ_{3D}) of the system is given by Table 5.5.

Table 5.4: Average standard deviations of the scanning system.

Objective	Position	Standard Deviation [μm]
ZEISS8	s_x	0.008
	s_y	0.005
	s_z	0.023
ASP15×15	s_x	0.024
	s_y	0.009
	s_z	0.061

$$s_{3D} = k\left(\sqrt{s_x^2 + s_y^2 + s_z^2}\right) \tag{5.6}$$

Table 5.5: 3D repeatability of the scanning system.

Objective	3D Repeatability ($k = 2$)
ZEISS8	0.050μm
ASP15×15	0.132μm

5.9 Comparison with other Measurement Systems

In this section, two different artifacts were measured with the developed scanning system and with other systems with a comproved higher accuracy. The two measured artifacts are a calibrated step with a height of 50μm [Sim09] and a mirror surface marked with a laser mask. The calibrated step was also measured using the nanopositioning and measuring machine (NPMM-200) [JHM+06, MHM+07, Jö6] and the mirror mask was measured using a comercial phase-shifting Fizeau interferometer (*ZYGO*®). The obtained surfaces and results are shown in Figure 5.21 and Table 5.6.

The results obtained for the calibrated step height with all systems lie within their confidence intervals, although, for the masked mirror, a large difference between the results obtained with the interferometer and the scanning system was observed. The developed system, as shown in Chapter 5.7 and 5.8, has a 3D repeatability of approximatelly

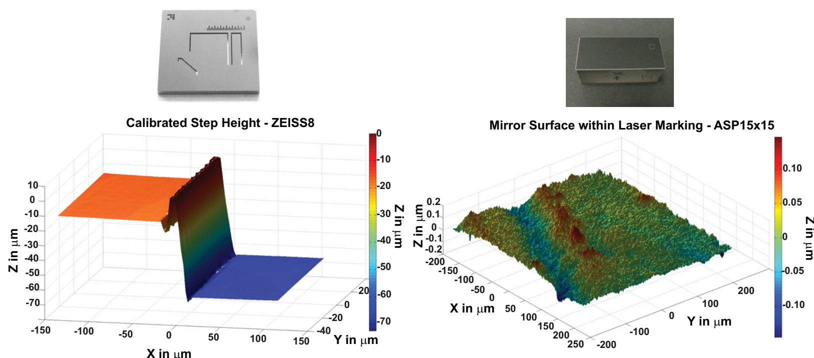

Figure 5.21: Comparison artifacts and their measured surfaces.

Table 5.6: Comparison of different measuring systems.

Calibrated Step Height (Expanded Uncertainty→ $k = 2$)		
Calibrated Height	$50.215\mu m$ $\pm 30nm$	
NPMM-200	$50.194\mu m$ $\pm 2.42nm$	
Scanning System	$50.198\mu m$ $\pm 65nm$	
Masked Mirror Surface - Flatness (Expanded Uncertainty→ $k = 2$)		
	Peak-to-Valley	RMS
ZYGO®	$13.798nm \pm 1.720nm$	$2.627nm \pm 0.044nm$
Scanning System	$143.9nm \pm 56.1nm$	$38.728nm \pm 7.884nm$

$50nm$ and the expected shape deviations of the masked mirror ($13nm$) lie under this limit. The results obtained in Table 5.6 illustrate the limits of the scanning system and do not represent the mirror surface accurately.

5.10 Ray-Tracing Implementations

The ray-tracing model of the developed scanning system, as explained in Chapter 4.3, was implemented using two different programming languages (*MatLab*®, *C/C++*) and the obtained results were compared regarding their execution time. The objective of this short comparison is to show that with the use of adequate computer techniques, ray-

tracing is nowadays a viable option even for real-time applications.

In order to evaluate the computational cost of the proposed ray-tracing model, both implementations were evaluated regarding their execution time. Figure 5.22 graphically shows how the execution time of each implementation changes as the number of rays used to describe the system grows. That is, given a group of n_R rays to represent the collimated laser beam and a fixed position $[\theta_x, \theta_y, \Delta_z]$ of the scanning system, Figure 5.22 shows the time necessary for calculating the reflection of all these rays on the mirror, their refraction on the objective lens and the resulting focus point of the system.

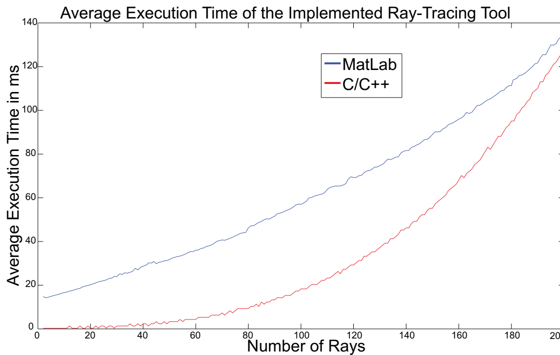

Figure 5.22: Execution speed of the ray-tracing model using different programming languages.

The graph in Figure 5.22 clearly displays the difference between both implementations. Due to its internal optimizations for matrix operations, the execution time in *MatLab*® grows more slowly than for the *C/C++* version of the ray-tracing model, as no considerations or optimized matrix libraries were used in its implementation. The graph also reveals that, even without these optimizations, the change from an interpreted language (*MatLab*®) to a compiled language (*C/C++*) can offer an increase of up to 90% ($n_R = 50$) in execution speed. With further improvements, this time could be even further reduced, so that the ray-tracing model may be used in real-time for reconstructing the scanned surfaces.

The ray-tracing model is however still computationally costly when compared to the LUT and polynomial correction strategies. Table 5.7

shows a brief comparison of the time necessary for reconstructing a surface with 100×100 points with each one of the methods introduced in Chapter 4.2.

Table 5.7: Average execution time of different error correction strategies.

Modelling and Error Correction	Execution Time $[s]$
Paraxial Model	0.012
Polynomials	0.067
Look-up Table	0.302
Ray-Tracing Model (*C/C++* ,$n_R = 50$)	49.365
Ray-Tracing Model (*MatLab*®, $n_R = 50$)	650.394

All the simulations shown in Figure 5.22 and Table 5.7 have been done using a workstation equipped with an *AMD® Phenom II X4 920* processor and 3 GB *RAM* running under *Microsoft Windows XP® Professional SP3*.

Chapter 6

Measurement Tasks and Applications

The main application of the developed system is the optical acquisition of 3D topographic information of microstructures, although the system also permits for example the measurement of macroscopic surfaces for the observation of machining marks and material structures. Once the operation, functionality and main characteristics of the developed scanning system have been fully described, this section will present a series of application examples of the system.

As discussed in previous chapters, the measurement of microstructures is essential in many technical fields. In this section, a series of different microstructures were measured using the developed system and the results are shown and discussed. The use of different objective lenses is also compared. All the presented surfaces have been reconstructed using the LUT correction method presented in Chapter 4.4.1; the objective lenses used are indicated for each measurement.

The first samples presented in this section are a series of silicon structures. Figure 6.1 and Figure 6.3 show a variety of measured surfaces using the ZEISS8 and ASP15×15 lenses. The second presented sample is a pinhole with a diameter of $600\mu m$. Figure 6.2 shows the measured surface using the ASP15×15 lens. The third and last sample shown is a milled aluminium surface. Figure 6.4 shows the machining marks left by the milling process.

All the samples shown illustrate the flexibility of the developed scanning system and its usage in a wide variety of measuring tasks.

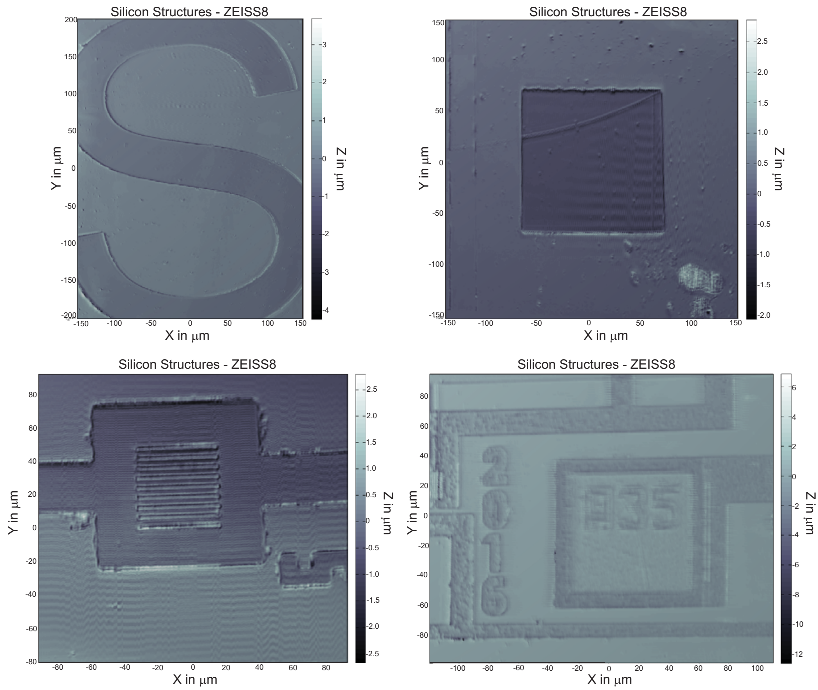

Figure 6.1: Different silicon structures measured with the ZEISS8 objective.

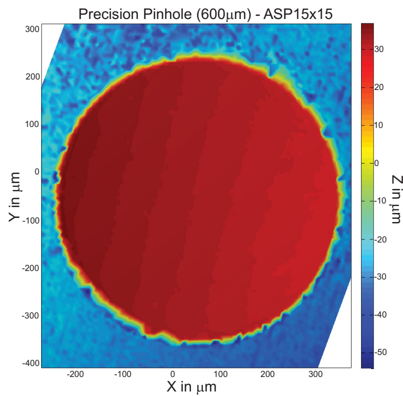

Figure 6.2: Pinhole ($\varnothing = 600\mu m$) measurement with the ASP15×15 objective.

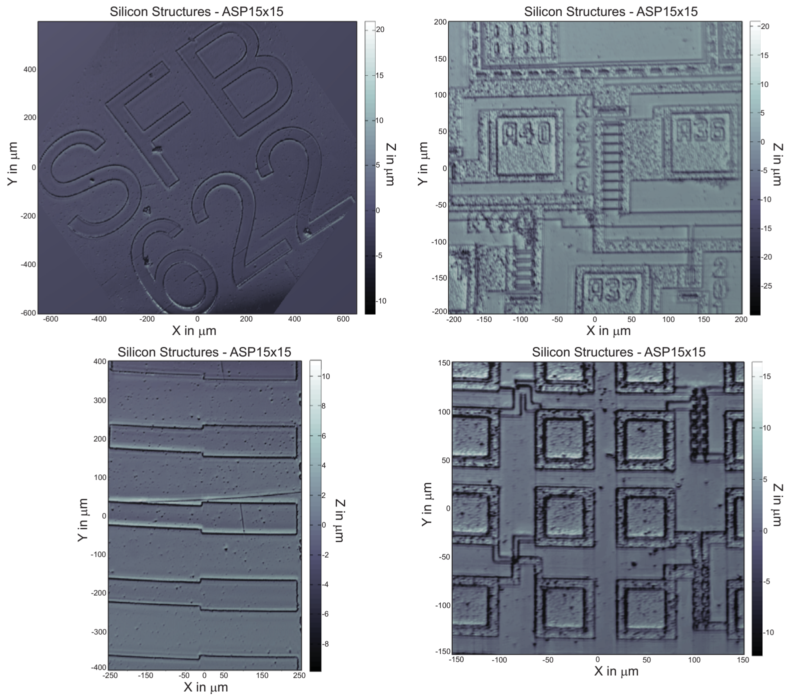

Figure 6.3: Different silicon structures measured with the ASP15×15 objective.

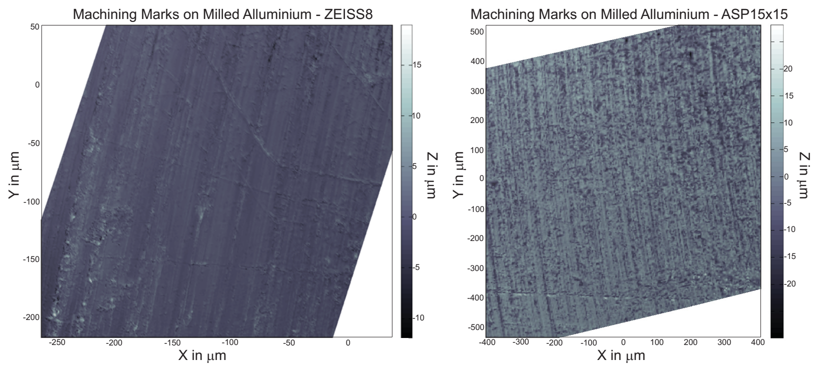

Figure 6.4: Machining marks on a milled aluminium surface.

Chapter 7

Conclusions and Further Work

7.1 Conclusions

The use of optical sensors for micro range measurements has gained increasing importance in the last years. Laser auto-focus sensors are one of the most promising methods in this field. They offer axial resolutions in the nanometre range and can also be used with optical rough surfaces, but they are traditionally regarded as single point measuring sensors and used in combination with positioning tables.

In the presented work, the use of auto-focus sensors as an area based sensor was investigated using a self developed scanning microscope. The developed system shows similarities with traditional auto-focus sensors and confocal laser scanning microscopes. It replaces the use of a positioning table with a tip-tilt mirror for achieving the lateral scanning of the samples. An integrated auto-focus sensor unit from conventional DVD technology based on the Foucault Knife-Edge principle in combination with the tip-tilt mirror and a high-precision linear stage were combined in order to build an areal optical measuring system with millimetre range and sub-micrometer resolution. The axial position of the system's focus is measured using the focus error signal (FES) generated by the auto-focus sensor and the displacement of the objective lens with the linear stage.

The presented system was conceived for fast and flexible surface mea-

surements and introduced the intentional use of simple uncompensated optics in order to reduce weight and size of the movable components, therefore improving measurement speeds and system dynamics and facilitating the miniaturization of the system. In order to overcome the effects of optical aberrations in the system, caused by the use of uncompensated optics, a new approach based on the use of different modelling techniques was proposed and evaluated, showing that, for the case of point scanning systems, the use of error-correction algorithms is a viable alternative to the traditional cost and volume-driven optimization of optical systems. Considering the optics as part of a complex system, the effects of optical aberrations in the measurement system as a whole can be modelled and the task of handling the resulting errors can be divided between optical compensation and computational correction, offering more flexibility for the design of the optical system.

Through a fully automated computer interface, different parameters of the scanning process can be easily controlled and altered, and surfaces with lateral dimensions up to $1500\mu m \times 1200\mu m$ can be measured with an axial resolution of up to $12nm$. The maximal measureable lateral dimensions can also be easily expanded with the use of objectives with longer focal lengths at the cost of lateral resolution.

7.2 Further Work

The developed auto-focus scanning microscope sets an important cornerstone in the expansion of auto-focus methods towards areal measurement and lays the foundations for the further development of scanning microscopes based on this working principle.

The developed system allows the measurement of a surface topography, measuring the 3D position of the system's focus point, but, the system also offers the possibility of simultaneously measuring the inclination of the surface. The inclination of the sample at the measuring point, as showed in this work, generates a parallel offset of the returning laser beam after it is descanned by the tip-tilt mirror. When the system is properly focused, this offset is a function of the sample's inclination and can be used for measuring it. Through the simulataneous acquisition of surface points and their slopes, the measured sur-

face can then be reconstructed with a much higher accuracy. Another possibility regarding surface inclination is the deliberate alteration of the telecentricy of the system in order to improve the maximal measurable inclinations.

The actual experimental setup has its measuring speed and size limited by the used electromechanical components and DA/AD converters. Eventhough the used auto-focus sensor is able to achieve measurement speeds in MHz range, the measurement speed of the system is limited by the resonant frequency of its mechanical components. The linear stage ($100Hz$) is the main limiting factor for the stepwise scanning and, for the continuous scanning, the tilting mirror ($1KHz$). The used DA/AD ($10KHz$) converters also impose a limit to the maximal measurement speed. A hardware optimization would enable the experimental setup to take better advantage of the sensor's speed.

Especially for the continuous scanning method, the use of mirrors based on microelectromechanical systems (MEMS) poses a promising alternative with scanning frequencies up to $10KHz$. Micromirrors also have their resolution only limited by the electronic noise of the system and, regarding miniaturization, they offer a great advantage in comparison with piezo mirrors. Another possible optimization would be the replacement of the used DA/AD converters. The used DA/AD converters have a resolution of 14 and 16 bits respectively and an acquisition speed of $10KHz$. Faster and more precise converters are commercially available with frequencies up to $2MHz$ and resolutions up to 18 bits with affordable costs (1500EUR). The use of faster DA/AD converters also facilitates the use of digital filtering to minimize the influence of electronic noise.

Regarding the used laser sensor unit, originally from the DVD technology, it uses only 50% of the returning light to generate the focus error signal. The other half of the light intensity is not used for the focus measurement. By changing the structure of the used holographic element (HOE) the laser unit could be designed to use two parallel Focault Knife-Edges, reducing the influence of surface inclination in the sensitivity of the system and minimizing the asymmetries caused by the presence of the knife-edge in the optical path.

In terms of software, the proposed ray-tracing model presents currently a major drawback regarding its execution speed. In order for

it to become a viable option, further programming optimizations are necessary to reduce its execution time.

The system was tested using a high-end microscope objective and out-of-the-shelf spherical and aspherical lenses as objectives. With the use of the proposed error correction strategies, a single aspherical lens could be designed for the specific application, focusing on the optimization of the spot size across the whole working range in detriment of characteristics such as distortion and field curvature, which can be computationally corrected.

The prerequisites of all the further improvements and works proposed in this section were layed by this work.

List of Figures

1.1 The nanopositioning and measuring machine (NPMM) developed in Ilmenau. 3
1.2 Conceptual diagram of the proposed optical pre-scanning system. 5

2.1 Image formation on a thin lens. 11
2.2 Ray-tracing general procedure. 12
2.3 Ray-tracing flowchart. 13
2.4 Models for optical imaging. 17
2.5 Third-order optical aberrations. 18
2.6 Barrel and pincushion distortion in a grid. 19
2.7 Basic compound microscope and its optical path. 20
2.8 Misky's confocal microscope [Min61]. 21
2.9 Basic principle of confocal microscopes. 22
2.10 Fraunhofer-diffraction on a circular aperture. 23
2.11 Rayleigh and sparrow resolution criteria. 25
2.12 Diagram of the astigmatic method for detection of the focus error signal (FES). 27
2.13 Typical focus error signal (FES) curve. 28
2.14 Beam path of the collinear astigmatic method. 29
2.15 The two planes of the astigmatic lens. 30
2.16 Two-dimensional gaussian distribution on the quadrant diode. 32
2.17 Diagram of the knife-edge method for detection of the focus error signal (FES). 33
2.18 Beam path of the knife-edge method. 34
2.19 Focus error detection with the obscuration method. . . 35
2.20 Types of optical beam scanning. 36
2.21 Lateral scanning in confocal microscopy. 37

3.1 Optical schema of the scanning system and its main components. 42
3.2 Miniaturized hologram laser unit [YMO+00]. 42
3.3 Developed laser scanning microscope (1-Hologram Laser Unit; 2-Tilting Mirror; 3-Camera Lens; 4-Camera; 5-Polarized Beam Splitter; 6-Linear Stage; 7-Objective). . . . 44
3.4 Telecentricity in the scanning system. 46
3.5 Telecentricity on the image space and system defocus. . 47
3.6 Typical signals during the stepwise and continuous scanning procedure. 48
3.7 System control signals and data acquisition. 50

4.1 Surface reconstruction using error correction. 56
4.2 Basic concepts of model based error correction. 58
4.3 Simplified 2D schematic of the scanning system. 59
4.4 Schematic diagram of the used 2D tilting mirror. 60
4.5 Simplified 3D paraxial schematic of the scanning system. 61
4.6 Lateral displacement of the focus point in the 3D paraxial model with $f'_{ob} = 15mm$. 62
4.7 Considerations on the non-collinear focus detection in scanning systems. 63
4.8 Complete 2D optical schema of the focus detection for the scanning system. 64
4.9 Integration boundaries for the non-collinear obscuration method. 65
4.10 Simulation of the FES using the paraxial model. 66
4.11 Influence of optical aberrations using a simple spherical lens ($f = 15mm$). 68
4.12 Mathematical representation of the scanning system for ray-tracing modelling. 69
4.13 Definition of the direction vectors D_{ke} and D_{pd}. 70
4.14 Representation of the kinematic chain of the ray-tracing model. 71
4.15 Simulation of the focus error signal FES using the ray-tracing model. 73
4.16 Influence of optical aberrations on the FES for $\beta = 0°$. . 74
4.17 Example model for current measurement. 75
4.18 Basic calibration concept for the laser scanning microscope. 78

4.19 Laser scanning microscope as a black box. 81
4.20 Conceptual design for the direct measurement of F_{LSM}. 82
4.21 Conceptual design for the direct measurement of F_{LSM}. 82
4.22 1D Look-up table of a sinusoidal function. 83
4.23 Describing F_{LSM} with a look-up table. 84

5.1 Characteristic curve of the system for different positions (θ_x, θ_y). 90
5.2 Measured S-Curve slope for different mirror tip-tilt angles (θ_x, θ_y). 91
5.3 Simulation of the error coefficients of the system using the paraxial and ray-tracing models. 94
5.4 Surface of a $\lambda/20$ flat mirror using the paraxial model (ASP15×15). 98
5.5 Surface of a $\lambda/20$ mirror using different correction methods (ASP15×15). 99
5.6 Surface of a $\lambda/20$ flat mirror using the paraxial model (ZEISS8). 100
5.7 Surface of a $\lambda/20$ mirror using different correction methods (ZEISS8). 101
5.8 Surface of a $\lambda/20$ mirror using the ray-tracing model with and without calibration. 103
5.9 Maximum measureable surface inclination. 104
5.10 Influence of the sample inclination on the FES. 106
5.11 Maximum measurable angle in a steel sphere ($\varnothing = 2mm$). 106
5.12 Non-telecentric ilumination and maximum measurable angle. 107
5.13 Minimal step of the linear stage of the objective lens (Δ_z). 108
5.14 Measurement of the lens position Δ_z and the FES in closed loop. 109
5.15 Measurement noise of the lens position Δ_z and the FES in closed loop for different angle positions. 110
5.16 Minimal step of the tilting angles of the scanning mirror (θ_x, θ_y). 111
5.17 Measurement of the tilting angles θ_x and θ_y. 111
5.18 Simulation of the spatial step size of the scanning system. 112
5.19 Simulation of the laser spot size for the ASP15×15 objective. 114

5.20 Measurement of a diffraction grating using the ZEISS8 objective. 115
5.21 Comparison artifacts and their measured surfaces. . . . 117
5.22 Execution speed of the ray-tracing model using different programming languages. 118

6.1 Different silicon structures measured with the ZEISS8 objective. 122
6.2 Pinhole ($\varnothing = 600\mu m$) measurement with the ASP15×15 objective. 122
6.3 Different silicon structures measured with the ASP15×15 objective. 123
6.4 Machining marks on a milled aluminium surface. . . . 123

List of Tables

2.1 Typical characteristics of commercial confocal scanning systems. 39

3.1 Specification of the system's components. 45
3.2 Average measurement frequency of the scanning methods. 49
3.3 Resolution limits of the used AD/DA converters. . . . 51

4.1 Parameters for the paraxial simulation of the *FES* based on the designed system. 66
4.2 Origin and normal vectors of the ray-tracing components. 72
4.3 Homogeneous transformations of the ray-tracing model. 72

5.1 Parameters and coefficients of the used lenses. 90
5.2 Calibrated parameters of the ray-tracing model. 97
5.3 Average minimum step size for different objective lenses. 113
5.4 Average standard deviations of the scanning system. . 116
5.5 3D repeatability of the scanning system. 116
5.6 Comparison of different measuring systems. 117
5.7 Average execution time of different error correction strategies. 119

Bibliography

[Bar85] Egbert Barthel. *Ein Beitrag zu berührungslosen Antastverfahren, dargestellt an Varianten des Fokussierverfahrens*. Ph.d. thesis, Technische Hochschule Ilmenau, 1985.

[Bas95] Michael Bass. *Handbook of Optics*. McGraw-Hill Inc., 2nd edition, 1995.

[Bei95] Leo Beiser. Fundamental architecture of optical scanning systems. *Applied Optics*, 34(31):7307, November 1995.

[Bit03] Frank Bitte. *Ein Spiegelmatrix-basiertes optisches 3D-Messsystem für die Mikrostrukturprüfung*. Ph.d. thesis, RWTH AAchen, 2003.

[BL76] Claude Bricot and Jean Claude Lehureau. Optical Focusing Device. *US Patent 4,023,033*, 1976.

[BM92] Bruce E. Bernacki and Masud Mansuripur. Diffraction analysis and evaluation of several focus- and track-error detection schemes for magneto-optical disk systems. In *Proc. SPIE 1316, Optical Data Storage, 150*, pages 150–156, August 1992.

[BM94] Bruce E. Bernacki and Masud Mansuripur. Causes of focus-error feedthrough in optical-disk systems: astigmatic and obscuration methods. *Applied optics*, 33(5):735–43, February 1994.

[Bog07] Robert Bogue. Nanometrology: a critical discipline for the twenty-first century. *Sensor Review*, 27(3):189–196, 2007.

[BR91] Jos Benschop and Gerard Van Rosmalen. Confocal compact scanning optical microscope based on compact disc technology. *Applied Optics*, 30(10):1179–1184, 1991.

[CFD05] Nathan S. Claxton, Thomas J. Fellers, and Michael W. Davidson. Laser Scanning Confocal Microscopy, 2005.

[CGLL84] Donald Kenneth Cohen, Wing Ho Gee, M. Ludeke, and Julian Lewkowicz. Automatic focus control: the astigmatic lens approach. *Applied Optics*, 23(4):565, February 1984.

[Cho06] Hyungsuck Cho. *Optomechatronics: Fusion of Optical and Mechatronic Engineering*. CRC Press, 1 edition, 2006.

[CK96] Timothy R. Corle and Gordon S. Kino. *Confocal Scanning Optical Microscopy and Related Imaging Systems*. Academic Press, 1996.

[CNY$^+$00] James Carriere, Raghu Narayan, Wei-Hung Yeh, Chubing Peng, Pramod Khulbe, Lifeng Li, Robert Anderson, Jinhan Choi, and Masud Mansuripur. Principles of optical disk data storage. *Progress in Optics*, 41:97–179, 2000.

[Coh87] Donald Kenneth Cohen. *Analysis of Methods for Detecting Focus Error in Optical Data Storage Systems*. Ph.d. thesis, University of Arizona, 1987.

[DDX$^+$10] Hans-ulrich Danzebrink, Thorsten Dziomba, M. Xu, A. Pidduck, Richard K. Leach, Andrew Yacoot, and Ludger Koenders. Scanning Probe Microscopy, Scanning Electron Microscopy and Critical Dimension: Nanometrology Status and Future Needs Within Europe. Technical report, Co-Nanomet Consortium, 2010.

[DIN99] DIN. DIN 1319-4: Grundlagen der Meßtechnik, 1999.

[Fab09] Markus Fabich. Advancing Confocal Laser Scanning Microscopy. *Optik & Photonik*, 4(2):40–43, June 2009.

[FMT99] A. Flammini, D. Marioli, and A. Taroni. Application of an optimal look-up table to sensor data processing. *IEEE Transactions on Instrumentation and Measurement*, 48(4):813–816, 1999.

[FY05] Hiroya Fukatsu and Kazuhisa Yanagi. Development of an optical stylus displacement sensor for surface profiling

instruments. *Microsystem Technologies*, 11(8-10):582–589, August 2005.

[Gas02] Kjell J. Gasvik. *Optical Metrology*. John Wiley & Sons Inc., West Sussex, 3rd edition, 2002.

[GD10] P S Gandhi and S Deshmukh. A 2D optomechanical focused laser spot scanner: analysis and experimental results for microstereolithography. *Journal of Micromechanics and Microengineering*, 20(1), January 2010.

[GM11] Luciano Selva Ginani and José Maurício S. T. Motta. Theoretical and Practical Aspects of Robot Calibration with Experimental Verification. *Journal of the Brazilian Society of Mechanical Sciences and Engineering*, 33(1):15–21, 2011.

[Gra07] Duncan Graham. Nanometrology–is it the next big thing in measurement? *The Analyst*, 132(2):95–6, February 2007.

[Gro03] Rudolf Gross. Optik und Quantenphänomene, 2003.

[GT09] Luciano Selva Ginani and René Theska. Development of a Software Simulation Tool for Movable Optic Components. In *International Congress of Mechanical Engineering - COBEM*, page 6, Gramado, 2009. ABCM.

[GT10] Luciano Selva Ginani and René Theska. Investigation of Opto-Mechanical Scanning Systems with the use of a Ray-Tracing Tool. In *Proceedings of EUSPEN*, pages 148–151, Delft, 2010. EUSPEN.

[GVY05] Yuval Garini, Bart J Vermolen, and Ian T Young. From micro to nano: recent advances in high-resolution microscopy. *Current opinion in biotechnology*, 16(1):3–12, February 2005.

[Hac10] Tobias Hackel. *Grundlegende Untersuchungen zu vertikalen Positioniersystemen für Nanopräzisionsmaschinen*. Ph.d. thesis, Technische Universität Ilmenau, 2010.

[Haf94] Heinz Haferkorn. *Optik: Physikalish-technische Grundlagen und Anwendungen*. Barth, Leipzig, 3 edition, 1994.

[HBVS03] Bohumil Hnilicka, Alina Besancon-Voda, and Heinz-Jörg Schröder. Modelling the Focus Error Signal Generation

in a DVD Player. In *IMACS Multiconference Computational Engineering Systems Applications*, pages 11–18, Lille, 2003. IEEE.

[HCHD06] H.N. Hansen, K. Carneiro, H. Haitjema, and L. De Chiffre. Dimensional Micro and Nano Metrology. *CIRP Annals - Manufacturing Technology*, 55(2):721–743, January 2006.

[Hec02] Eugene Hecht. *Optik*. Oldenbourg GmbH, München, 4 edition, 2002.

[Her01] Martin Hermann. *Numerische Mathematik*. Oldenbourg GmbH, München, 2001.

[HTB+06] Günter Höhne, René Theska, Torsten Brix, Markus Lotz, Thomas Frank, and Tobias Hackel. Design of high precision positioning and measuring machines using virtual prototyping. *ABCM Symposium Series in Mechatronics*, 2:485–492, 2006.

[Hul07] Angela Hullmann. Measuring and assessing the development of nanotechnology. *Scientometrics*, 70(3):739–758, March 2007.

[IEE90] IEEE. IEEE Std 610.12-1990 - Standard Glossary of Softare Engineering Terminology, 1990.

[J06] Gerd Jäger. Precision Mechatronics - Nanomeasuring and Nanopositioning Engineering at the Technische Universität Ilmenau. In *Proceedings of the 3rd Vietnam Conference on Mechatronics*, Hanoi, 2006.

[JCG08] JCGM. JCGM 100:2008 - Evaluation of measurement data - Guide to the expression of uncertainty in measurement, 2008.

[JHM+06] Gerd Jäger, Tino Hausotte, Eberhard Manske, H.-J. Büchner, Rostyslav Mastylo, N Dorozhovets, and N Hofmann. Nanomeasuring and nanopositioning engineering. *Proceedings of SPIE*, pages 628001–628001–9, 2006.

[Kni03] S. Knight. Overview of NIST metrology development for the semiconductor industry. In *11th IEEE International*

Conference on Advanced Thermal Processing of Semiconductors. RTP 2003, pages 35–44. IEEE, 2003.

[Kra00] Werner Krause. *Gerätekonstruktion in Feinwerktechnik und Elektronik*. Carl Hanser GmbH, München, 3. edition, 2000.

[Kre06] Erwin Kreyszig. *Advanced Engineering Mathematics*. John Wiley & Sons Inc., 9th edition, 2006.

[LBB+10] Richard K. Leach, Robert Boyd, Theresa Burke, Hans-ulrich Danzebrink, Kai Dirscherl, Thorsten Dziomba, Mark Gee, Ludger Koenders, Valérie Morazzani, Debdulal Roy, Wolfgang E S Unger, and Andrew Yacoot. Consultation on a European Strategy for Nanometrology. Technical report, Co-Nanomet Consortium, 2010.

[Lea11] Richard Leach, editor. *Optical Measurement of Surface Topography*. Springer Berlin Heidelberg, Berlin, Heidelberg, 2011.

[Lin94] Psang Dain Lin. Modeling for optical ray tracing and error analysis. *Mathematical and Computer Modelling*, 19(12):37–48, June 1994.

[Mar85] Gerald F. Marshall. *Laser Beam Scanning*. Marcel Dekker Inc., New York, 1985.

[Mar91] Gerald F. Marshall. *Optical Scanning*. Marcel Dekker Inc., New York, 1991.

[Mas05] Rostyslav Mastylo. A focus sensor for an application in a nanopositioning and nanomeasuring machine. *Proceedings of SPIE*, 5856(June):238–244, 2005.

[Mas12] Rostyslav Mastylo. *Optische und Taktile Nanosensoren auf der Grundlage des Fokusverfahrens für die Anwendung in Nanopositionier- und Nanomessmaschinen*. Ph.d. thesis, Technische Universität Ilmenau, 2012.

[Mer84] Peter-Michael Merbach. *Untersuchungen über die Realisierungsmöglichkeiten des berührungslosen Antastens bei automatisierten Dreikoordinaten-Längenmeßeinrichtungen*. Ph.d. thesis, Technische Hochschule Ilmenau, 1984.

[MHM+07] Eberhard Manske, Tino Hausotte, Rostyslav Mastylo, T Machleidt, K-H Franke, and Gerd Jäger. New applications of the nanopositioning and nanomeasuring machine by using advanced tactile and non-tactile probes. *Measurement Science and Technology*, 18(2):520–527, 2007.

[Min61] Marvin Minsky. Microscopy Apparatus. *US Patent 3,013,467*, 1961.

[MMJ04] Rostyslav Mastylo, Eberhard Manske, and Gerd Jäger. Entwicklung eines Fokussensors und Integration in die Nanopositionier- und Nanomessmaschine. *tm - Technisches Messen*, 71(11/2004):596–602, 2004.

[MPM05] Steven A. Miller, James Pond, and Bernhard Michel. Raytracing trifft Maxwell-Gleichungen : Über die Integration von mikro- und makrooptischem Design. *Photonik*, 6, June 2005.

[MS97] Masud Mansuripur and Glenn Sincerbox. Principles and techniques of optical data storage. *Proceedings of the IEEE*, 85(11):1780–1796, 1997.

[NS92] Helmut Naumann and Gottfried Schröder. *Bauelemente der Optik*. Carl Hanser GmbH, München, 6 edition, 1992.

[Pac08] Hugo Pacheco. Ray Tracing in Industry. Technical report, Minho University, Braga, 2008.

[Paw06] James B. Pawley, editor. *Handbook of Biological Confocal Microscopy*. Springer Science+Business Media, New York, 3rd edition, 2006.

[PBMH02] Timothy J. Purcell, Ian Buck, William R. Mark, and Pat Hanrahan. Ray tracing on programmable graphics hardware. *ACM Transactions on Graphics*, 21(3), July 2002.

[Phi03] George McArtney Phillips. *Interpolation and Appoximation by Polynomials*. Springer Verlag, New York, 2003.

[Phy03] Physik Instrumente. S-334 Tip/Tilt Mirror, 2003.

[Pol] Mikhail Polyanskiy. Refractive Index Database. *http://refractiveindex.info/*.

[Rie88] Horst Riesenberg. *Handbuch der Mikroskopie*. VEB Verlag Technik, Berlin, 3 edition, 1988.

[Sch82] Manfred Schilling. *Konstruktionsprinzipien der Gerätetechnik*. Habilitation thesis, Technische Hochschule Ilmenau, 1982.

[She93] Song Shen. Theoretical models and comparison of three focus-error detection methods. In *Proceedings of SPIE*, volume 2053, pages 144–149. SPIE, 1993.

[Sim09] Simetrics. Vertical Standard VS, 2009.

[SM62] G. H. Spencer and M. V. R. K. Murty. General Ray-Tracing Procedure. *Journal of the Optical Society of America*, 52(6):672, June 1962.

[SMGH95] K.-P. Schröder, W. Mirandé, H. Geuther, and C. Herrmann. In quest of nm accuracy: supporting optical metrology by rigorous diffraction theory and AFM topography. *Optics Communications*, 115:568–575, 1995.

[SS97] C.J.R. Sheppard and D.M. Shotton. *Confocal Laser Scanning Microscopy*. BIOS Scientific Publishers, Oxford, 1997.

[SS02] Mark L. Schattenburg and Henry I. Smith. The critical role of metrology in nanotechnology. In Martin C. Peckerar and Michael T. Postek, Jr., editors, *Proceedings of SPIE*, pages 116–124, Gaithersburg, July 2002. SPIE.

[TFHL04] René Theska, Thomas Frank, Tobias Hackel, and Markus Lotz. Design Principles for Highest Precision Applications. In *Proceedings of ASPE*, page 4, Orlando, 2004. ASPE.

[The88] René Theska. *Berürungslos-optische Antastung von Messobjekten unter ausnutzung astigmatischer Abbildungseigenschaften*. Ph.d. thesis, Technische Hochschule Ilmenau, 1988.

[TV98] Emanuele Trucco and Alessandro Verri. *Introductory Techniques for 3S Computer Vision*. Prentice Hall Inc., 1998.

[UU12] Michael Ulbrich and Stefan Ulbrich. *Nichtlineare Optimierung*. Springer Basel, Basel, 2012.

[vdB07] Adriaan van den Bos. *Parameter Estimation for Scientists and Engineers*. John Wiley & Sons Inc., New Jersey, 1 edition, 2007.

[Web96] Robert H. Webb. Confocal optical microscopy. *Reports on Progress in Physics*, 59:427–471, 1996.

[WPH06] A Weckenmann, G Peggs, and J Hoffmann. Probing systems for dimensional micro- and nano-metrology. *Measurement Science and Technology*, 17(3):504–509, March 2006.

[XRJR07] Peng Xi, Bartlomiej Rajwa, James T. Jones, and J. Paul Robinson. The design and construction of a cost-efficient confocal laser scanning microscope. *American Journal of Physics*, 75(3):203, 2007.

[YMO+00] Shinya Yoshida, Kohji Minami, Kuniaki Okada, Hiroyuki Yamamoto, Tetsuo Ueyama, Keiji Sakai, and Yukio Kurata. Optical Pickup Employing a Hologram-Laser-Photodiode Unit. *Japanese Journal of Applied Physics*, 39(2):877–882, 2000.

Liste der bisher erschienenen Bände, Stand 01.07.2013

Bericht aus dem Institut für Maschinenelemente und Konstruktion (IMK), 1990 – 2010

Band 1 **Institut für Maschinenelemente und Konstruktion der TU Ilmenau (Hrsg.):**
Forschung und Lehre im Institut für Maschinenelemente und Konstruktion
(Institutsbericht)
Ilmenau : ISLE, 1999. - ISBN 3-932633-37-7

Band 2 **Spiller, Frank:**
Möglichkeiten der rechentechnischen Umsetzung von Erkenntnissen aus der Konstruktions-systematik unter Nutzung der Featuretechnologie
(Dissertation TU Ilmenau 1998)
Ilmenau : ISLE, 1998. - ISBN 3-932633-20-2

Band 3 **Leibl, Peter:**
Entwicklung eines featureorientierten Hilfsmittels für die Konstruktion kostengünstiger Produkte
(Dissertation TU Ilmenau 1998)
Ilmenau : ISLE, 1998. - ISBN 3-00-003695-4

Band 4 **Lutz, Steffen:**
Kennlinie und Eigenfrequenzen von Schraubenfedern
(Dissertation TU Ilmenau 2000)
Ilmenau : ISLE, 2000. - ISBN 3-932633-47-4

Band 5 **Kletzin, Ulf:**
Finite-Elemente-basiertes Entwurfssystem für Federn und Federanforderungen
(Dissertation TU Ilmenau 2000)
Ilmenau : ISLE, 2000. - ISBN 3-932633-48-2

Band 6 **Volz, Andreas K.:**
Systemorientierter Karosserie-Konzeptentwurf am Beispiel der Crashsimulation
(Dissertation TU Ilmenau 1998)
Ilmenau : ISLE, 2000. - ISBN 3-932633-52-0

Band 7 **Brix, Torsten:**
Feature- und constraint-basierter Entwurf technischer Prinzipe
(Dissertation TU Ilmenau 2001)
Ilmenau : ISLE, 2001. - ISBN 3-932633-67-9

Band 8 **Rektor der TU Ilmenau und Institut für Maschinenelemente und Konstruktion der TU Ilmenau (Hrsg.) in Zusammenarbeit mit Carl Zeiss Jena GmbH**
Vom Arbeitsblatt zum virtuellen Prototyp – 50 Jahre Konstruktionssystematik
(Institutsbericht)
Ilmenau : ISLE, 2002. - ISBN 3-932633-68-7

Band 9 **Liebermann, Kersten:**
Rechnergestütztes Entwurfs- und Optimierungssystem für Schraubendruckfedern
(Dissertation TU Ilmenau 2003)
Ilmenau : ISLE, 2003. - ISBN 3-932633-74-1

Band 10 **Meissner, Manfred; Denecke, Klaus:**
Die Geschichte der Maschinenelemente als Fachgebiet und Institut an der Technischen Universität Ilmenau von 1953 bis 2003
(Institutsbericht)
Ilmenau : ISLE, 2003. - ISBN 3-932633-82-2

Band 11 **Geinitz, Veronika:**
Genauigkeits- und auslastungsoptimierte Schraubendruckfedern
(Dissertation TU Ilmenau 2006)
Ilmenau : ISLE, 2006. - ISBN 3-938843-11-X

Band 12 **Institut für Maschinenelemente und Konstruktion (Hrsg.):**
Festschrift zum Ehrenkolloquium anlässlich der Emeritierungen von Univ.-Prof. Dr.-Ing. habil. Dr. h.c. Günter Höhne und Univ.-Prof. Dr.-Ing. habil. Hans-Jürgen Schorcht
(Institutsbericht)
Ilmenau : ISLE, 2005. -ISBN 3-932633-97-0

Band 13 **Wittkopp, Tobias:**
Mehrkörpersimulation von Schraubendruckfedern
(Dissertation TU Ilmenau 2005)
Ilmenau : ISLE, 2005. - ISBN 3-938843-07-1

Band 14 **Frank, Stefan:**
Justierdrehen – eine Technologie für Hochleistungsoptik
(Dissertation TU Ilmenau 2007)
Ilmenau : ISLE, 2008. - ISBN 978-3-938843-35-4

Band 15 **Schilling, Thomas:**
Augmented Reality in der Produktentstehung
(Dissertation TU Ilmenau 2008)
Ilmenau : ISLE, 2008. - ISBN 978-3-938843-42-0

Band 16 **Lotz, Markus:**
Konstruktion von Messspiegeln hochgenauer Mess- und Positioniermaschinen
(Dissertation TU Ilmenau 2009)
Ilmenau : ISLE, 2009. - ISBN 978-3-938843-46-8

[Band 17] **Hackel, Tobias:**
Grundlegende Untersuchungen zu vertikalen Positioniersystemen für Nanopräzisionsmaschinen
(Dissertation TU Ilmenau 2010)
Münster, Westf : Monsenstein und Vannerdat, 2010. - ISBN 978-3-86991-111-3

[Band 18] **Frank, Thomas:**
Konzeption und konstruktive Gestaltung der Messkreise von Nanomessmaschinen
(Dissertation TU Ilmenau 2010)
Münster, Westf : Monsenstein und Vannerdat, 2010. - ISBN 978-3-86991-194-6

Berichte aus dem Institut für Maschinen- und Gerätekonstruktion (IMGK), 2010 - …

Band 19 **Sondermann, Mario:**
Mechanische Verbindungen zum Aufbau optischer Hochleistungssysteme
(Dissertation TU Ilmenau 2010)
Ilmenau : Univ.-Verl. Ilmenau, 2011. - ISBN 978-3-939473-94-7

Band 20 **Stephan Husung:**
Simulation akustischer Produkteigenschaften unter Nutzung von Virtual Reality während der Produktentwicklung
(Dissertation TU Ilmenau 2011)
Ilmenau : Univ.-Verl. Ilmenau, 2012. - ISBN 978-3-86360-026-6

Band 21 **Dobermann, Dirk:**
Stabilisierung der Bildlage abbildender optischer Systeme
(Dissertation TU Ilmenau 2012)
Ilmenau : Univ.-Verl. Ilmenau, 2013. - ISBN 978-3-86360-056-3

Band 22 **Taubmann, Peter:**
Analyse der Ventilfederbewegung als Beitrag zur Beeinflussung der Verschleißursachen an den Auflageflächen
(Dissertation TU Ilmenau 2013)
Ilmenau : Univ.-Verl. Ilmenau, 2013. - ISBN 978-3-86360-059-4

Band 23 **Erbe, Torsten:**
Beitrag zur systematischen Aktor- und Aktorprinzipauswahl im Entwicklungsprozess
(Dissertation TU Ilmenau 2013)
Ilmenau : Univ.-Verl. Ilmenau, 2013. - ISBN 978-3-86360-060-0

Band 24: **Ginani, Luciano Selva**
Optical Scanning Sensor System with Submicron Resolution
(Dissertation TU Ilmenau 2013)
Ilmenau : Univ.-Verl. Ilmenau, 2013. - ISBN 978-3-86360-068-6